

AD A0 59529

DDC FILE COPY

18 AFOSR TR-78-1260 LEVEL II 2  
19 FINAL REPORT.  
9 1 Apr 73-30 Sep 77

6 RELATIONSHIP BETWEEN NEAR-FIELD AND TELESEISMIC  
OBSERVATIONS OF SEISMIC SOURCE PARAMETERS.

10 Shelton Alexander (814-865-2622) 11 Jul 78

The Pennsylvania State University  
Department of Geosciences  
Geophysics Section  
403 Deike Building  
University Park, Pennsylvania 16802

12 133p.  
DDC  
OCT 5 1978  
F

15 Grant No. AFOSR-73-2515  
Mod. No. AFOSR 73-2515A-G  
Project-Task AO 1827-6  
Contract Interval: 1 April 1973 to 30 September 1977  
Amount of Contract: \$234,533  
ARPA Order 1827

16 41-20

Prepared  
for

AIR FORCE OFFICE OF SCIENTIFIC RESEARCH  
OFFICE OF AEROSPACE RESEARCH  
UNITED STATES AIR FORCE  
AFOSR (SRPG), ARLINGTON, VIRGINIA

Approved for public release;  
distribution unlimited.

WORK SPONSORED BY THE ADVANCED RESEARCH PROJECTS AGENCY

AIR FORCE OFFICE OF SCIENTIFIC RESEARCH (AFSC)  
NOTICE OF TRANSMITTAL TO DDC  
This technical report has been reviewed and is  
approved for public release IAW AFR 190-12 (7b).  
Distribution is unlimited.  
A. D. BLOSE  
Technical Information Officer

408 103  
78 09 05 034 LB

TABLE OF CONTENTS

- I. Objective
- II. Major Accomplishments
- III. Publications
- Appendix A: Examples of Results Not Included in Other Publications or Reports
- Appendix B: Abstracts of Ph.D. Theses Completed
- Appendix C: The Nature and Origin of Seismic Codos from NTS Explosions Recorded at NORSAR by P. Glover and S. S. Alexander
- Appendix D: Determination of Focal Parameters for the Oroville, California Sequence of August 1975 Using Synthetic and Seismic Research Observatory Data by R. W. Tiff and S. S. Alexander
- Appendix E: A Crust and Upper Mantle Model for Novaya Zemlya from Rayleigh Wave Dispersion Data by D. W. McCowan, P. Glover and S. S. Alexander
- Appendix F: A Static and Dynamic Finite Element Analysis of the 1971 San Fernando, California, Earthquake by D. W. McCowan, P. Glover and S. S. Alexander
- Appendix G: A Fast, Accurate Method for Computing Group-Velocity Partial Derivatives for Rayleigh and Love Modes by W. L. Rodi, P. Glover, T. M. C. Li and S. S. Alexander

ACCESSION for

NTIS  White Section

DDC  Buff Section

UNANNOUNCED

JUSTIFICATION \_\_\_\_\_

---

BY \_\_\_\_\_

DISTRIBUTION/AVAILABILITY CODES

Dist.	Avail.	Special
A		

RELATIONSHIP BETWEEN NEAR-FIELD AND TELESEISMIC  
OBSERVATIONS OF SEISMIC SOURCE PARAMETERS

Brief Summary

I. Objective

The overall objective of this investigation has been to establish the connection between source mechanism parameters inferred from seismic measurements made relatively near to earthquakes and explosions and those inferred from teleseismic observations.

II. Major Accomplishments

The following brief summary outlines the accomplishments under this grant. We have:

1. found that there are significant variations in body-wave and surface wave excitation for explosions of comparable magnitude detonated in similar source media and located only a few kilometers apart at NTS (Yucca Flats and Pahute Mesa). These observed differences in excitation and energy partitioning imply either a rapidly varying tectonic stress field in the source region and/or strongly varying patterns of near-source fracturing. Source-generated P-wave coda of two minutes duration or more are observed at NORSAR to vary significantly in strength and character among nearby Yucca and Pahute events, possibly due to short-period surface wave to P-wave scattering;
2. shown that relatively few SRO-type stations can be used to compare source mechanisms for suites of events of varying size in a given source region. For example, foreshocks and aftershocks of the Utah-Idaho border and Oroville, California sequences of 1975, as recorded at the Albuquerque SRO station, have

been analyzed and compared; in both cases the principal foreshock exhibited the same mechanism as the main shock, while the aftershocks are more varied in mechanism. For both sequences we were able to match the observed Love and Rayleigh waveforms and spectra as the mechanism changed. Average path dispersion (hence structure) is a useful by-product of the analysis;

3. developed a promising approach for using the entire short-period signature for identifying short-time-lag double events; the technique will work best at regional distances where relatively broad-band surface wave (e.g. Lg, Rg) as well as body waves (Pn, Pg, Sg) signals are recorded;

4. developed further the surface-wave inversion techniques we devised for inferring lateral heterogeneity in structure using any combination of Love and Rayleigh group velocity or phase velocity dispersion for as many modes as are observed;

5. developed a finite element code that can compute theoretical waveforms that would be observed at any point of interest from an arbitrary source extended in space and time in geologically heterogeneous structures. In addition we have been able to combine this code with the Haskell method to propagate waves from a simple, plane-layered region into and across a complicated structure. Using this code the 1971 San Fernando earthquake was simulated using static and dynamic fault models with a variable rupture velocity. We obtained good agreement with observed near-field observations for a rupture velocity of about 2 km/sec. We have obtained digitized records for additional near-field sites and are now attempting to interpret them with the aid of the finite element calculations; this involves interpolation of the digital data to a uniform sampling rate in time and filtering to produce a wave-form with the same spectral band as the numerical code calculations;

6. far-field surface wave amplitude spectra have been studied for their use in determining seismic source parameters. Using theoretical spectra generated for a double couple source in a plane layered half-space, the minimum residual fit to the observed spectra was obtained, yielding source parameter estimates; and

7. developed a software package for analysis of SRO data tapes. In addition to standard types of filtering, matched filtering, spectral decomposition, and dispersion analysis, we have implemented routines for polarization filtering to isolate individual phases and stacking of events.

This grant has supported wholly or in part two completed Ph.D. theses and three that are near completion. In addition, the soft-ware developed under this grant, particularly the inversion programs, has been disseminated rather widely and it is being used by several organizations on ARPA/AFOSR projects.

### III. Publications

Publications based on the work summarized above are listed on the following two pages.

## PUBLICATIONS

- Alexander, S. S., L. S. Turnbull, and R. J. Greenfield, April 1973. Non-Linear Least-Squares Determination of Seismic Source Parameters Using Frequency-Dependent Radiation Patterns of Rayleigh and Love Waves, *Trans. A.G.I.*, Vol. 54, No. 4, p. 367.
- Alexander, S. S., 1976. The Seismological Potential of the New Seismic Research Observatory (SRO) Network, *Trans. Am. Geophys. Union*, Vol. 57, No. 4, p. 284.
- Alexander, S. S., 1976. Applications of the Seismic Research Observatory (SRO) Network, *Trans. Am. Geophys. Union*, Vol. 57, No. 10, p. 758.
- Alexander, S. S., T. W. Tifft, and P. Glover, 1976. Comparison of Earthquake Source Mechanisms for Foreshock, Mainshock, and Aftershock Sequences Using Seismic Research Observatory (SRO) Data, *Trans. Am. Geophys. Union*, Vol. 57, No. 12, pp. 954-955.
- Glover, P., D. W. McCowan and S. S. Alexander, 1974. Dynamic Finite Element Method (DFEM) Calculations of Elastic Wave Propagation in Two-Dimensional Structures, *Trans. Am. Geophys. Union*, Vol. 55, p. 351.
- McCowan, D. W., P. Glover and S. S. Alexander, 1973. Dynamic Finite Element Method Calculations for Stress Waves in Earth Structure. *Earthquake Notes*, Vol. XLIV, Nos. 1-2, p. 34.
- McCowan, D. W., May 1975. Dynamic Finite Element Analysis with Applications to Seismological Problems. Ph.D. Thesis, The Pennsylvania State University, 189 pp.
- McCowan, D. W., P. Glover, and S. S. Alexander, 1977. A Static and Dynamic Finite Element Analysis of the 1971 San Fernando, California, Earthquake, *Geophys. J. R. Astr. Soc.*, Vol. 48, pp. 163-185.
- Rodi, W. L., P. Glover, T. M. C. Li, and S. S. Alexander, 1975. Group Velocity Partial Derivative Computations and the Systematic Inversion of Surface Wave Data, *Trans. Am. Geophys. Union*, Vol. 56, No. 6, p. 402.
- Rodi, W. L., P. Glover, T. M. C. Li, and S. S. Alexander, 1975. A Fast Accurate Method for Computing Group Velocity Partial Derivatives for Rayleigh and Love Modes, *Bull. Seis. Soc. Am.*, Vol. 65, pp. 1105-1114.
- Turnbull, L. S. and S. S. Alexander, June 1973. Determination of Source Parameters for Several Mid-Atlantic Ridge Events Using Surface Wave Radiation Patterns, *Earthquake Notes*, Vol. XLIV, Nos. 1-2, p. 22.
- Turnbull, L. S., D. F. Sun and S. S. Alexander, November 1973. Determination of Seismic Source Parameters for Several Earthquakes Using Frequency Dependent Radiation Patterns, *Trans. A.G.I.*, Vol. 54, No. 11, p. 1133.

## PUBLICATIONS (Continued)

- Turnbull, L. W., Jr., August 1976. Determination of Seismic Source Parameters Using Far-Field Surface Wave Spectra. Ph.D. Thesis, The Pennsylvania State University, 424 pp.
- Yeh, Y.-T. and S. S. Alexander, 1976. A New Surface-Wave Inversion Method for Determining Lateral Variations in Crust-Mantle Structure, Trans. Am. Geophys. Union, Vol. 57, No. 4, p. 286.

## APPENDIX A

Contained in this Appendix are examples to illustrate some of the results discussed in the Summary of Accomplishments but not incorporated into the references, publications, or reports that appear elsewhere in this document.

TABLE A-I

This Table summarizes the variations in Love and Rayleigh wave magnitudes expected as a function of source structure, depth, and fault type (tectonic stress); VSS = vertical strike-slip; 45DS = 45° dip-slip; periods as given and amplitudes were measured from synthetic seismograms for 3000 km distance.

Structure		Canadian Shield - Brune and Dorman (1963)							
Depth (km)	Fault	$\log \frac{A}{T}(L)$	Per. (sec)	$\overline{\log R(L)}$ Love	Per. (sec)	$\log \frac{A}{T}(R)$	Per. (sec)	$\overline{\log R(R)}$ Rayleigh	Per. (sec)
1.0	VSS	1.64	17	6.31	17	1.09	17	6.18	17
	45DS	1.34	17	6.01	17	0.99	17	6.08	17
5.0	VSS	1.62	17	6.30	17	0.77	18	5.95	18
	45DS	1.32	17	6.00	17	0.42	16,19 22	5.63	16,19 22
10.0	VSS	1.64	17	6.32	17	0.17	22	5.72	22
	45DS	1.34	17	6.02	17	0.71	15,16 17	5.84	15,16 17

Structure		Hamilton Healy							
Depth (km)	Fault	$\log \frac{A}{T}(L)$	Per. (sec)	$\overline{\log R(L)}$ Love	Per. (sec)	$\log \frac{A}{T}(R)$	Per. (sec)	$\overline{\log R(R)}$ Rayleigh	Per. (sec)
1.0	VSS	0.90	15	5.89	15	0.59	16	5.79	16
	45DS	0.60	15	5.59	15	0.46	16	5.68	16
5.0	VSS	1.28	15,16	6.28	15	0.78	16	5.95	16
	45DS	0.97	15,16	5.98	15	0.43	14,15 16,17	5.55	15,16 17
10.0	VSS	1.38	16	6.45	16	0.23	20	5.86	20
	45DS	1.07	16	6.15	16	0.79	14,15 15,16	5.93	14,15 16

Structure		35CM2 - Alexander (1963)							
Depth (km)	Fault	$\log \frac{A}{T}(L)$	Per. (sec)	$\overline{\log R(L)}$	Per. (sec)	$\log \frac{A}{T}(R)$	Per. (sec)	$\overline{\log R(R)}$	Per. (sec)
1.0	VSS	0.69	16	5.71	16	0.40	16	5.52	16
	45DS	0.38	16	5.41	16	0.49	16,17	5.62	16
5.0	VSS	1.36	16.5	6.44	17	0.79	16.5, 17	5.98	17
	45DS	1.06	16.5	6.14	17	0.49	15,16 17,18	5.65	15,16 17,18
10.0	VSS	1.31	16.5	6.40	17	0.22	21	5.71	21
	45DS	1.01	16.5	6.09	17	0.67	16	5.83	16

TABLE II

BASIC SRO PROGRAMS:

- 1 HEADERDUMP.  
READS MULTIPLE FILE SRO TAPES AND PRINTS HEADER LABEL FOR EVERY RECORD.
- 2 SPSURSET.  
READS SEGMENT OF AN SRO TAPE, EXTRACTS SPECIFIED SHORT PERIOD WINDOW, DEMAGNIFIES DATA, AND PRODUCES A STANDARD FORMAT SUBSET TAPE AND A PLOT TAPE.
- 3 LPSURSET.  
SIMILAR TO SPSURSET WITH ADDITIONAL FEATURE OF DEMULTIPLYING THREE COMPONENT LONG PERIOD DATA AND ROTATING HORIZONTAL COMPONENTS TO A SPECIFIED DIRECTION.

SRO DATA PROCESSING PROGRAMS:

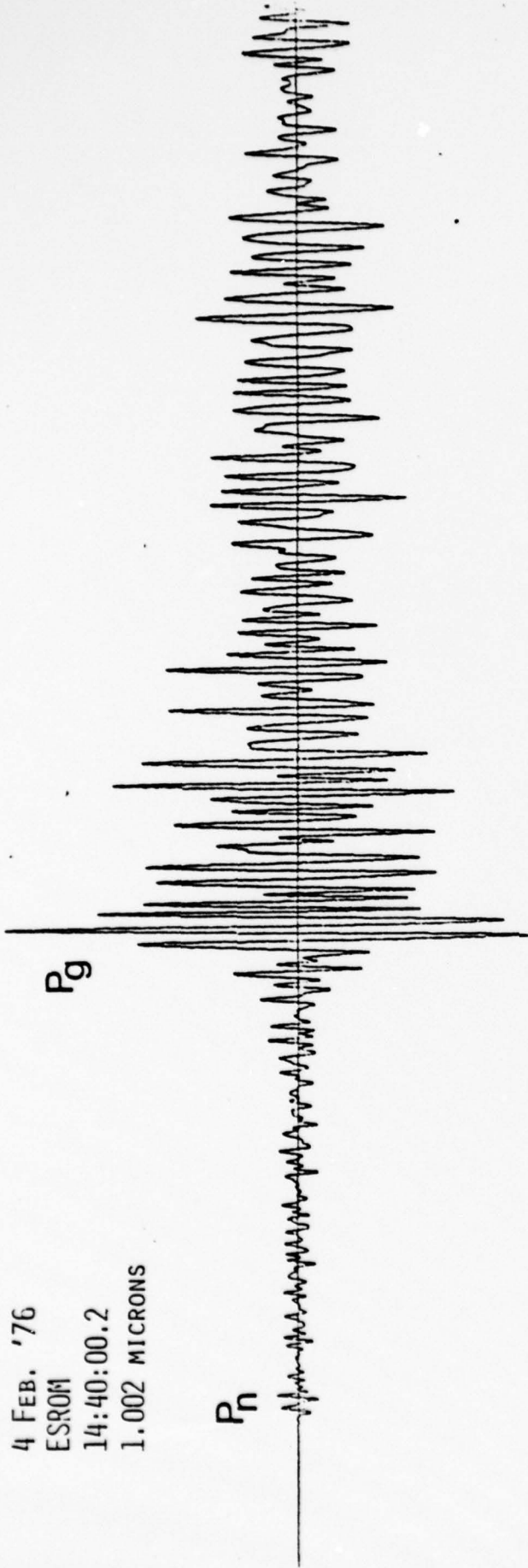
- 1 COLLAPSE.  
AN OLD SDL PROGRAM TO MATCHFILTER LONG PERIOD DATA USING REAL OR SYNTHETIC SIGNALS AS FILTERS. ADDITIONAL FEATURES ALLOW COMPUTATION OF SMALL EVENT SPECTRA, BEAMING OF ARRAY DATA, ETC.
- 2 NARROWBAND.  
PERFORMS NARROW BAND FILTERING IN THE FREQUENCY DOMAIN FOR EXTRACTION OF GROUP ARRIVAL TIMES. JUDICIOUS CHOICE OF WIDER PASS BAND ALLOWS SEPERATION OF NORMALLY AND INVERSELY DISPERSED ARRIVALS.
- 3 SEISHOPRINT.  
PRODUCES 2-D CONTOUR PLOT OF POWER VS FREQUENCY AS A FUNCTION OF TIME. OPTIONALLY, PROGRAM ALSO PRODUCES INSTRUMENT CORRECTED PLOTS OF POWER VS FREQUENCY AVERAGED OVER A GIVEN TIME WINDOW.
- 4 LOG-LOGPLOT.  
COMPUTES POWER SPECTRUM OF A LENGTH OF SEISMIC DATA AND PRODUCES A CALCOMP PLOT OF LOG POWER VS LOG FREQUENCY, THUS FACILITATING THE DETERMINATION OF CORNER FREQUENCY.
- 5 LTOR.  
COMPUTES THE POWER SPECTRAL DENSITY OF THE LOVE AND RAYLEIGH WAVE (VERTICAL COMPONENT) PORTION OF A LONG PERIOD SEISMOGRAM AND PRODUCES A PLOT OF THE RATIO L/R AS A FUNCTION OF PERIOD.

ANCILIARY PROGRAMS.

- 1 SWIP2M.  
INVERTS OBSERVED SURFACE WAVE DISPERSION DATA TO DETERMINE THE BEST SINGLE OR COMPOSITE, FLAT OR SPHERICAL, EARTH MODEL. INPUT CONSISTS OF A GUESS MODEL, SINGLE OR COMPOSITE, THE OBSERVED DATA AND ESTIMATES OF THEIR VARIANCES, AND A WEIGHTING MATRIX EXPRESSING CONFIDENCE IN THE TRIAL MODEL. DATA CAN BE LOVE OR RAYLEIGH WAVE PHASE AND GROUP VELOCITIES, FUNDAMENTAL OR HIGHER MODE.
- 2 HARPING.  
COMPUTES LOVE AND RAYLEIGH WAVE PHASE AND GROUP VELOCITIES AND THEIR PARTIALS WITH RESPECT TO THE MODEL PARAMETERS FOR A PLANE-PARALLEL LAYERED HALFSPACE.
- 3 STRTCH.  
CONVERTS INPUT FLAT EARTH MODEL INTO A CORRESPONDING PSEUDO-SPHERICAL MODEL FOR USE WITH HARPING.
- 4 RAYPUNCH AND LOVEPUNCH.  
COMPUTES THE RAYLEIGH OR LOVE WAVE DISPLACEMENT-STRESS QUANTITIES AT AN IMAGINARY SURFACE CONTAINING THE POINT SOURCE FOR A PLANE-PARALLEL LAYERED HALFSPACE.
- 5 SRSIN.  
COMPUTES SYNTHETIC LOVE AND RAYLEIGH WAVE SEISMOGRAMS FROM EARTHQUAKE AND EXPLOSIVE SOURCES IN A PLANE-PARALLEL LAYERED EARTH MODEL.

Figure A-1. Short-period and long-period seismograms recorded at the Albuquerque SRO station for two nuclear explosions (Keelson and Esrom) located within approximately 2 km of one another at Yucca Flats and detonated about 20 minutes apart in time. Note that the levels of excitation for the short-period phases (Pn,Pg,Lg) are approximately the same for the two events, whereas there is a very large difference in both Love and Rayleigh wave excitation between the two with the second (Esrom) exhibiting the large surface waves (tectonic release). Similar results were obtained for other (SDCS) stations.

4 FEB. '76  
ESROM  
14:40:00.2  
1.002 MICRONS



4 FEB. '76  
KEELSON  
14:20:00.1  
0.773 MICRONS

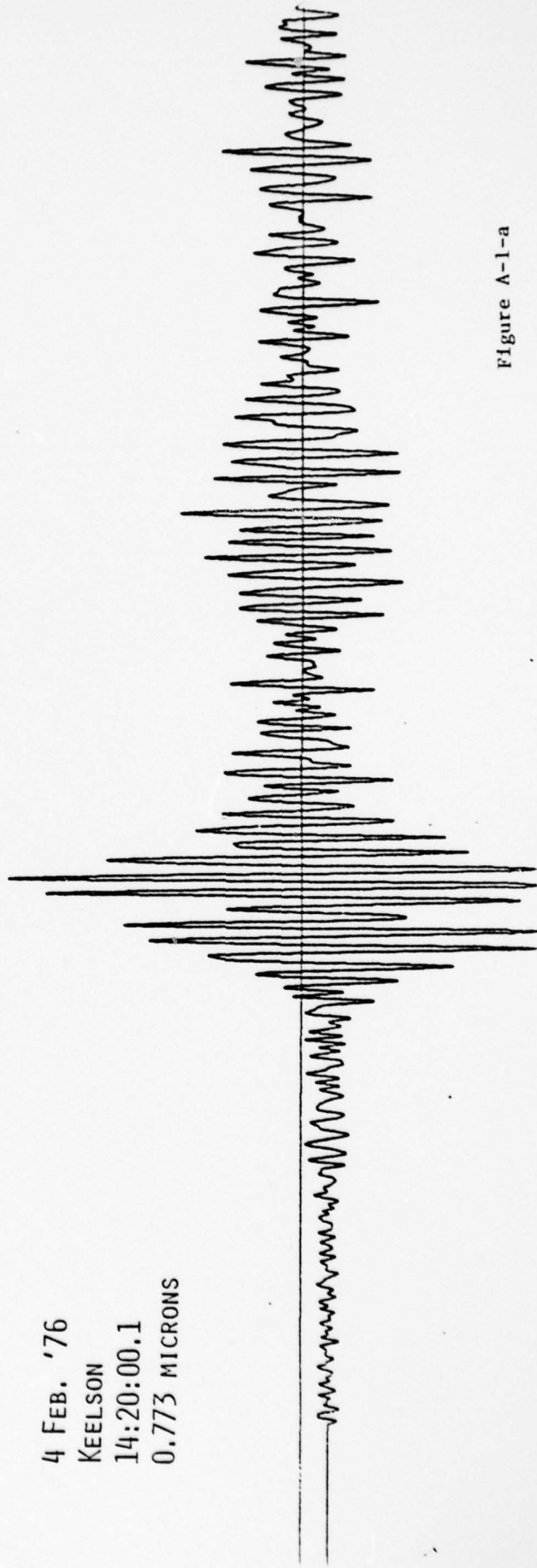
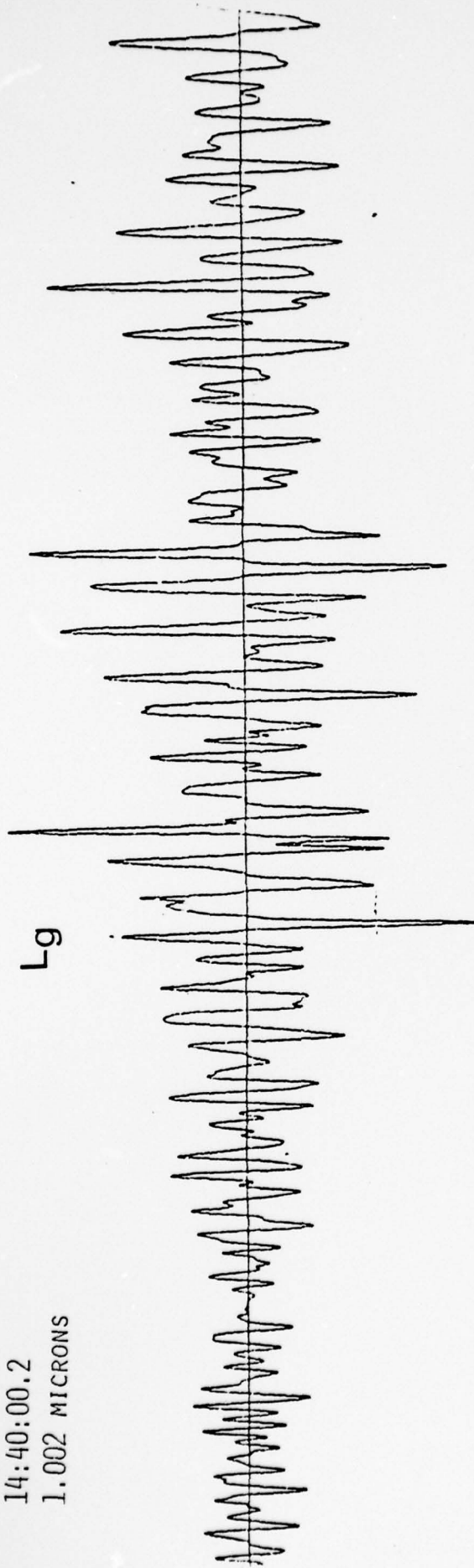


Figure A-1-a

4 FEB. '76  
ESROM  
14:40:00.2  
1.002 MICRONS



4 FEB. '76  
KEELSON  
14:20:00.1  
0.773 MICRONS

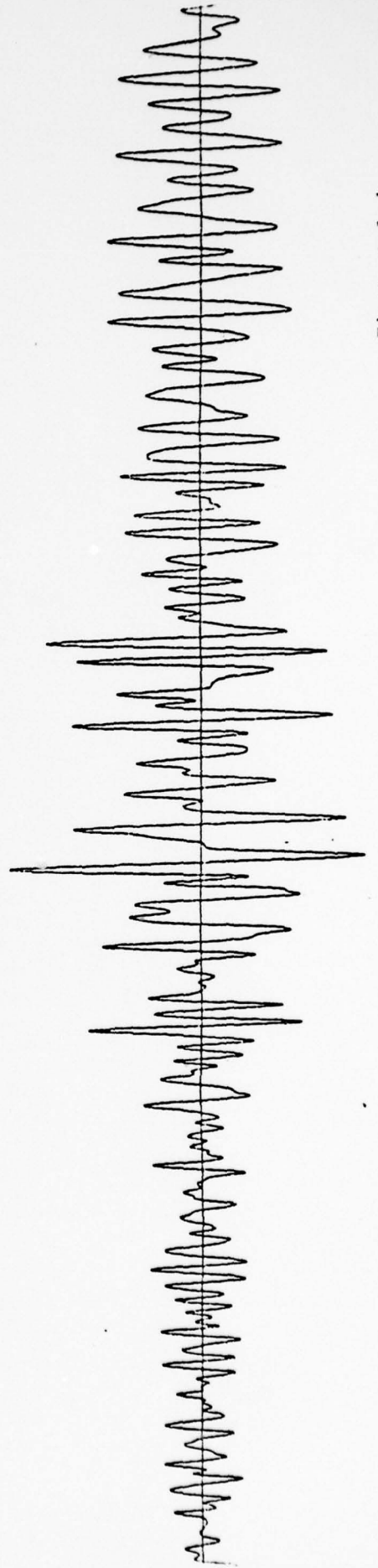


Figure A-1-b

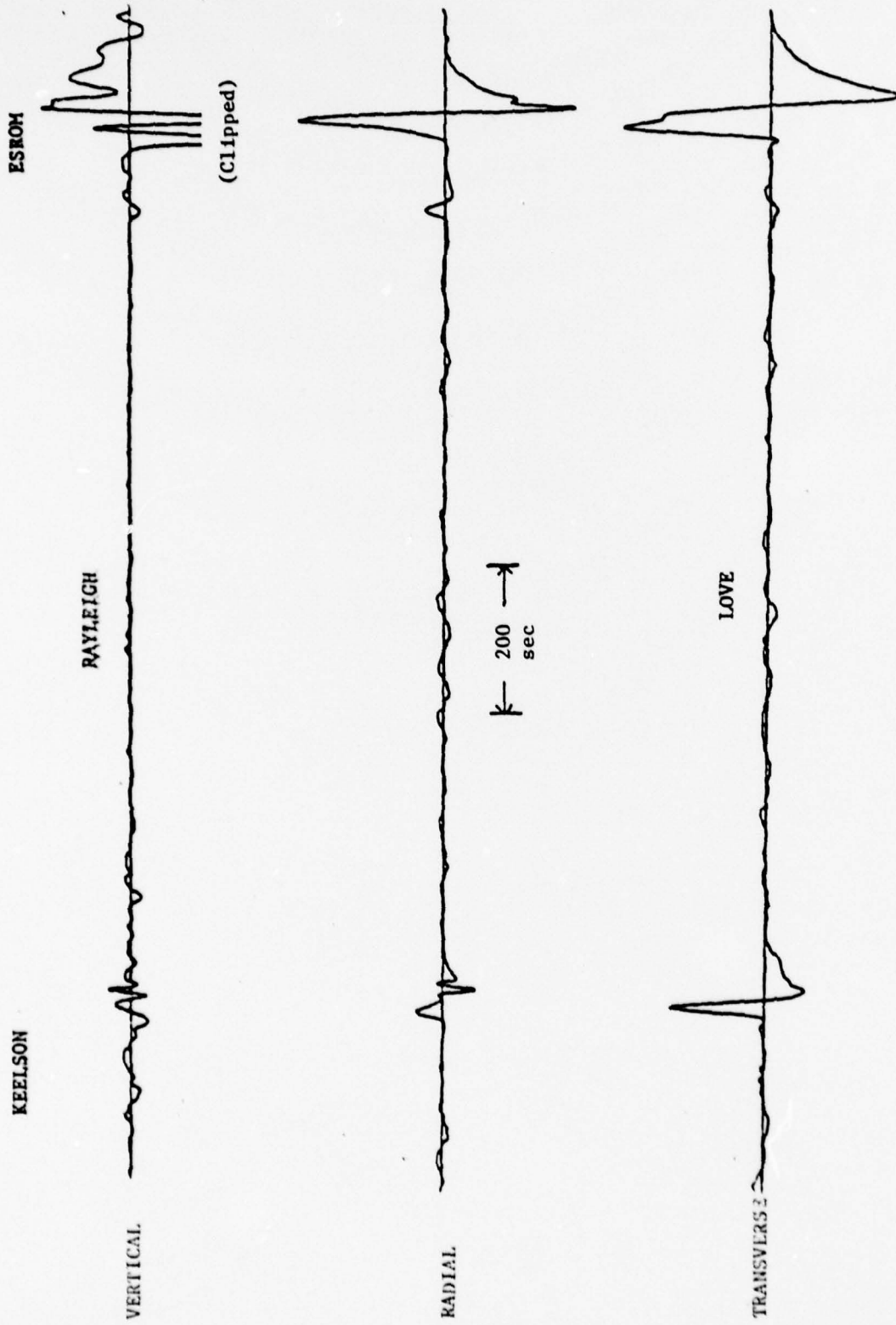


Figure A-1-c

APPENDIX B

Abstract and Table of Contents of Ph.D. Theses completed under  
sponsorship from this grant.

ABSTRACT

DYNAMIC FINITE ELEMENT ANALYSIS WITH APPLICATIONS  
TO SEISMOLOGICAL PROBLEMS\*

A Dynamic Finite Element Method (DFEM) for elastic wave propagation in general two-dimensional heterogeneous media was developed from a causal, variational statement of Hamilton's Principle and applied to several seismological problems. Judged from test cases where the results were compared against known analytic solutions, the method was able to reproduce temporal and phase characteristics of Rayleigh waves such as travel time, group velocity dispersion, ellipticity, and phase lag to within 5% of the values predicted by theory. The Rayleigh wave amplitude, however, was found to be 25% small over the whole spatial waveform, an effect which was attributed to the artificial viscosity in the method necessary to remove severe numerical noise. Three seismological problems of interest were solved: 1) Rayleigh wave propagation across a continental margin structure, 2) radiation from an extended shear source, and 3) a static and dynamic study of the February 9, 1971 San Fernando earthquake. Conspicuous among the many results were: phase velocity anisotropy on the order of 5% in the continental margin problem which agreed with Alexander's (1963) model experiment, P and S wave radiation spectra from the extended shear source problem which fit the prediction of the Brune (1970) seismic source theory, and static and dynamic models of the San Fernando earthquake which supported the results of

---

\* Ph.D. Thesis of D. W. McCowan

previous investigations of near-field data for this event (e.g., Bolt, 1972; Alewine and Jordan, 1973). Based on these results, conclusions were drawn concerning the extension of the method to more complicated seismological problems.

## TABLE OF CONTENTS

Introduction . . . . .	1
The Finite Element Method . . . . .	12
The Euler Theorem of Variational Calculus . . . . .	14
Essentials of The FEM . . . . .	16
Linear Constraints . . . . .	21
Dirichlet Boundary Conditions . . . . .	22
Higher Order Elements . . . . .	25
Some Examples . . . . .	28
The DFEM . . . . .	35
Numerical Integration . . . . .	42
Test Cases . . . . .	47
Comparison with Viecelli's Halfspace Solution . . . . .	48
Sharp Source Solutions of The Halfspace Problem . . . . .	55
Layer Over A Halfspace Problem . . . . .	62
Three Problems . . . . .	67
Rayleigh Wave Dispersion Near A Continental Margin . . . . .	67
Radiation from An Extended Shear Source . . . . .	96
FEM Study of The San Fernando Earthquake . . . . .	114
Summary and Conclusions . . . . .	152
Appendix A . . . . .	159
Some Notes on The Theoretical Solution to Lamb's Problem . . . . .	159
Appendix B . . . . .	161
Some Useful Matrix Techniques . . . . .	161
Appendix C . . . . .	167
Stability of The Newmark $\beta$ Integration Method . . . . .	167
Appendix D . . . . .	170
Least Squares Method with Trade-off Correction . . . . .	170
Appendix E . . . . .	173
Description of The DFEM Computer Code . . . . .	173
Appendix F . . . . .	177
Effects of Different Levels of Damping on The DFEM Lamb's Problem Solution . . . . .	177
References . . . . .	181

## ABSTRACT

### DETERMINATION OF SEISMIC SOURCE PARAMETERS USING FAR-FIELD SURFACE WAVE SPECTRA\*

Far-field surface wave amplitude spectra have been studied for their use in determining seismic source parameters. Using theoretical spectra generated for a double couple source in a plane layered half-space, the minimum residual fit to the observed spectra was obtained, yielding source parameter estimates.

An iterative least-squares regression program has been developed to fit observed Rayleigh and Love wave amplitude spectra. Iteration is on the dip angle, slip angle, strike direction, and seismic moment. The initial choice of these parameters, with nominal azimuthal coverage (six stations over  $180^{\circ}$  azimuth), was found to be primarily limited by the symmetry of the theoretical source description. As determined from tests with theoretical spectra, this initial choice can be as much as  $30^{\circ}$  from the correct value of the angular parameters and several times the value of the moment. Intelligent estimates of these initial choices can be obtained using either bodywave source mechanism estimates, or an improved version of Tsai and Aki's (1970a) exhaustive fitting procedure developed in this study. One advantage of the iterative method is that, for the same parameter set and the same degree of precision desired, it is several times faster computationally than exhaustive fitting procedures.

---

\*Ph.D. Thesis of L. S. Turnbull, Jr.

An important extension of both the iterative and exhaustive techniques that has been developed in this study is the amplitude spectral ratio concept. A 'master event' is determined for a particular geographical region, whose source mechanism has been established with a high degree of confidence. The source mechanism of other events occurring in the same region can then be determined using amplitude spectral ratios with the master event, eliminating the need to make path and instrument corrections.

Complete expressions for the next two higher multipoles (quadrupole and octapole) were generated from the work of Harkrider (1970). Their importance relative to that of a double couple was found to be a function of frequency and the physical extent of the rupture volume. Alternatively, an extended fault can be modelled using multiple double couples displaced in both space and time which simulate a finite rupture velocity. This source description can produce non-symmetrical surface wave radiation, but for most earthquakes with magnitudes less than  $m_b$  6.0 observed at teleseismic distances, a point double couple source description is adequate.

Because the spectral fitting methods depend upon the shape and level of the amplitude spectra, theoretical fundamental and first higher mode Rayleigh and Love wave double couple and quadrupole amplitude spectra were generated for many source configurations. The most important observations from these spectra are: (1) for both

source types and modes, depth variations produce the largest changes in spectral levels and shapes, (2) for both modes, the double couple spectral level is generally an order of magnitude greater than that of the quadrupole, (3) for both source types, the largest changes in spectral level occur in the 10 to 20 seconds period range for the fundamental mode and 9 to 12 seconds period range for the first higher mode, and (4) the most prominent spectral holes of the two Rayleigh modes occur for either source types only when the fault is vertical strike-slip.

In order to develop procedures for obtaining improved surface wave magnitude estimates, various combinations of surface wave spectra for the fundamental and first higher mode were examined, using a double couple source, to assess invariance with respect to source parameter variations. From the spectral combinations, the most important observations are: (1) for all except very shallow sources ( $\sim 5$  km), the most reliable estimates of surface wave magnitude are obtained from azimuthal averages of total surface wave energy,  $R^2 + L^2$ , of the fundamental mode, and (2) for shallow sources it is best to use an azimuthal average of fundamental mode Rayleigh waves alone,  $R^2$ , in the period range of 20 to 30 seconds.

Finally, from the analysis of several earthquakes using both spectral fitting procedures and spectral ratios, the major conclusions are: (1) the source region earth model has little effect on the

depth estimate for shallow events ( $<10$  km), (2) the azimuthal spread of stations should be greater than  $90^{\circ}$  in order to obtain a valid solution, (3) for Eurasian events with travel paths along the Alpine-Himalayan fold system, abnormally low group velocities ( $\sim 0.5$  km/sec low) and almost twice the normal energy attenuation coefficient were observed, (4) for the Bear Valley earthquake of 22 June 1973, the far-field seismic moment is an order of magnitude greater than that obtained from near-field observations, and (5) that the use of spectral ratios was found to be a valid approach in the analysis of two pairs of events.

## TABLE OF CONTENTS

CHAPTER	TITLE	PAGE
	ACKNOWLEDGMENTS	ii
	LIST OF TABLES	viii
	LIST OF FIGURES	xi
	ABSTRACT	xxxvi
I.	INTRODUCTION	1
	A. INVESTIGATING THE SEISMIC SOURCE	1
	B. PREVIOUS SOURCE STUDIES USING FAR-FIELD SURFACE WAVE SPECTRA	3
	C. OBJECTIVES OF THIS STUDY	5
	D. A BRIEF SURVEY OF SEISMIC SOURCE THEORIES AND THEIR USE IN INTER- PRETING TELESEISMIC SURFACE WAVE DATA	11
	1. Point Source Representations	12
	2. Dislocation Source Models	15
	3. Volume Relaxation Models	18
II.	DETERMINATION OF SEISMIC SOURCE PARA- METERS USING A MULTIPOLAR SOURCE TO INTERPRET FAR-FIELD RAYLEIGH AND LOVE WAVE DATA	21
	A. CALCULATION OF SURFACE WAVE RADIATION FROM A MULTIPOLAR SOURCE IN A FLAT STRATIFIED EARTH	22
	1. Double Couple Sources	22
	2. Theoretical Extension To Higher Order Sources	33
	3. A Preliminary Estimate of the Relative Importance of Higher Order Source Terms	39
	B. CHARACTERISTICS OF THEORETICAL SPECTRA FROM BURIED MULTIPOLAR SOURCES IN A LAYERED HALF-SPACE	43
	1. General Theoretical Spectral Characteristics	43

TABLE OF CONTENTS  
(continued)

CHAPTER	TITLE	PAGE
	2. The Invariance of Combinations of Surface Wave Spectra to Source Parameter Variations	52
	3. Spectral Characteristics of a Multiple Source	59
C.	DETERMINATION OF SEISMIC SOURCE PARAMETERS FROM FAR-FIELD SURFACE WAVE AMPLITUDE SPECTRA	64
	1. Theoretical Discussion Of An Exhaustive Procedure (Tsai's Method) For Estimating Seismic Source Parameters	66
	2. Theoretical Development of Iterative Regression On Multipolar Surface Wave Spectra	79
	3. The 'Master' Event Method And Its Use of Amplitude Spectral Ratios	89
D.	SUMMARY	91
III.	DETERMINATION OF SEISMIC SOURCE PARAMETERS FOR SEVERAL EARTHQUAKES USING SURFACE WAVE AMPLITUDE SPECTRA	94
A.	DATA PREPARATION	96
	1. The Instrument Response Correction $I_1(\omega)$	96
	2. The Path Transfer Function $G(\omega, r)$	98
B.	ANALYSIS OF THE SOUTHEASTERN MISSOURI EARTHQUAKE OF 21 OCTOBER 1965	101
	1. The Far-Field Source Mechanism Solution	101
	2. The Effect of the Source Region Earth Model on the Focal Depth Estimate	120
	3. The Use of Phase Spectra in the Fitting Procedures	124
C.	ANALYSIS OF TWO EVENTS HAVING INDEPENDENT SOURCE INFORMATION	125
	1. The Eurasian Earthquake LX+CENAP+45	125

TABLE OF CONTENTS  
(continued)

CHAPTER	TITLE	PAGE
	2. The Bear Valley Earthquake of 22 June 1973	139
D.	ANALYSIS OF TWO PAIRS OF EVENTS HAVING MINIMAL INDEPENDENT SOURCE INFORMATION	149
	1. The Analysis of Two Low Magnitude Italian Events	149
	2. The Analysis of Two Eurasian Earthquakes	167
E.	SUMMARY	180
IV.	CONCLUSIONS	182
	A. MAJOR CONCLUSIONS	182
	B. RECOMMENDATIONS FOR FUTURE STUDIES	192
APPENDIX	TITLE	PAGE
A.	AN EXAMPLE OF USING THE HASKELL MOVING DISLOCATION MODEL TO DETER- MINE SOURCE PARAMETERS FROM THE VERY NEAR-FIELD	194
B.	FREQUENCY VARIATION OF THE MULTIPOLE COEFFICIENTS IN ARCHAMBEAU'S SOURCE MODEL	211
C.	UNITS OF THE HARKRIDER DESCRIPTION OF A MULTIPOLAR SOURCE IN A LAYERED HALF-SPACE	215
D.	DERIVATION OF FAR-FIELD MULTIPOLAR SURFACE WAVE RESPONSE FUNCTIONS	219
E.	REPRESENTATIVE DISPLAYS OF THEORETICAL SPECTRA	260

TABLE OF CONTENTS  
(continued)

APPENDIX	TITLE	PAGE
F.	THEORETICAL SPECTRAL VARIATIONS OF PARTICULAR COMBINATIONS OF SURFACE WAVES WITH RESPECT TO SOURCE PARAMETERS	326
G.	EXPLOSIVE SOURCE IN A LAYERED HALF-SPACE	351
H.	ITERATIVE REGRESSION ON DOUBLE COUPLE RADIATION PATTERNS	360
I.	APPROXIMATION OF SURFACE WAVE AMPLITUDE SPECTRA AND GROUP VELOCITIES BY NARROWBAND FILTERING	370
J.	REPRESENTATIVE EARTH MODELS AND EXAMPLES OF THEIR THEORETICAL SPECTRAL RESPONSE	383
	REFERENCES	417

APPENDIX C

The Nature and Origin of Seismic Coda

from NTS Explosions

Recorded at NORSAR

by

P. Glover

and

S.S. Alexander

Geophysics Program

Geosciences Department

The Pennsylvania State University

University Park, Pa. 16802

The Nature and Origin of Seismic Codas from NTS Explosions Recorded at NORSAR

On the basis of the travel-time tables and theoretical studies of explosive sources, short-period seismograms of NTS explosions recorded at NORSAR, an epicentral distance of approximately  $73^{\circ}$ , should show relatively simple waveforms. The first arrival, consisting of the direct P-wave and the surface reflection pP, should be followed 18 seconds later by PcP, also contaminated by its surface reflection, pPcP. This is in turn followed by the reflected phases, PP, at 161 seconds after P, and PPP some 263 seconds after P. Each of these arrivals could reasonably be expected to consist of 2 or 3 cycles of a predominantly 1 Hz wave when recorded by the NORSAR short period vertical seismometers. Figures 1 and 2 show typical NORSAR beams from explosions detonated in two distinct areas of NTS, Pahute Mesa and Yucca Flats respectively. The pertinent epicenter data for these events are given in Table 1. Clearly these seismograms are far from simple, particularly those from the Pahute Mesa events (Figure 1). This observation prompts the obvious question as to why. In the discussion that follows we will attempt to elucidate the nature of the seismic coda and determine the source of its generation.

One of the valuable properties of an array is its ability to resolve the speed and propagation direction of an arrival. The array can then be steered in this direction and beams formed so as to minimize the contamination of the desired signal by unwanted arrivals. Not only can the expected arrivals be separated on the basis of arrival-time at a single station, they can be separated on the basis of propagation velocity across the array. A systematic approach is to assume that all signals originating in the source region arrive at the receiver along the same azimuth as the direct P waves, and to form beams corresponding to the velocity range of the expected late arrivals. The relative power in each beam for a given

window is then displayed as a function of beaming velocity and arrival time. Contours of equal power then reveal coherent arrivals as peaks in velocity vs time space.

The lower part of Figure 3 shows such a plot for the explosion STILTON, which was detonated in Pahute Mesa, slightly to the NW of the Silent Canyon Caldera (see Table 1); the contour interval is 3 db. The first arrival has an apparent velocity of 18.0 km/sec, which is somewhat lower than the 18.8 km/sec predicted by the Herrin travel-time tables, possibly due to dipping interfaces within the crust beneath the array. However, the important feature of this plot is that the conspicuous arrival 18 seconds after the initial P-wave onset, also has an apparent velocity of 18.0 km/sec. So, although the differential travel-time is correct for PcP, the velocity is much slower than the PcP predicted value of 25.8 km/sec. In fact, all the arrivals in the 90 seconds of the beam following the initial P-wave onset have an apparent velocity of 18.0 km/sec. This is amply demonstrated by normalizing the plot by the maximum in each time window, as is shown in the upper part of Figure 3, which is contoured at 1 db intervals. A search for arrivals was conducted by steering the array toward  $\pm$  20 degrees from the P-wave back-azimuth. No significant off-azimuth arrivals were detected.

Although the velocity time plots are themselves a qualitative measure of the coherency of signals across the array, a more quantitative measure of coherency is desirable. A computationally convenient procedure is to compute the semblance

coefficient

$$S_c = \frac{\sum_{j=1}^M \left\{ \sum_{i=1}^N x_{i,j} + \tau(i) \right\}^2}{N \sum_{j=1}^M \sum_{i=1}^N x_{i,j}^2 + \tau(i)}$$

where  $x_{i,j} + \tau(i)$  is the signal at the  $i$  th channel

$M$  is the length of the time window over which  $S_c$  is computed

$N$  is the number of channels in the beam, from which the energy normalized multichannel coherency

$$C = \frac{1}{(N-1)} (NS_c - 1) \quad (2)$$

is computed, and varies in the range

$$-\frac{1}{N-1} \leq C \leq 1 \quad (3)$$

Figure 4 shows the coherency in the best-beam from STILTON as function of time; the relative power in the beam as a function of time; and the beam itself. They confirm that the arrival 18 seconds after the P-wave has the same coherency as the initial P-wave at the beaming velocity of 18 km/sec, and is only 7 db down in power. Thus, this arrival cannot be PcP. The plots show that further discrete arrivals, also coherent at the P-wave velocity, occur up to 60 seconds after the initial P-wave arrival.

Beam steering, coherency and relative power plots were produced for each of the 8 Pahute Mesa events shown in Figure 1. These tended to confirm the results from the analysis of STILTON. No evidence of PcP, or other phases arriving with velocities and propagation directions significantly different from the initial P-wave were found. The measured P-wave velocities themselves were identical to within the experimental error. The distribution in time of the coda arrivals, their relative power, and their coherencies, all varied from event to event. As an example, Figure 5 shows the coherency and relative power from KASSERI. This event clearly has many more arrivals than STILTON and the coda remains both coherent and more energetic over a longer interval. No arrivals were found with velocities significantly different than that of the initial P-wave.

To examine the coherency of the codas among events at Pahute Mesa, the 8 NORSAR beams were stacked. Each beam was normalized to unit amplitude, and time aligned on the front trough of the P-wave signal. The lower trace in Figure 6 shows the result. The maximum amplitude in the P-wave is 0.89, so that the signal loss due to dissimilarities in waveform (see Figure 1) is not severe. In this case of coda, however, the amplitudes are reduced by approximately a factor of 3 throughout the time interval, and thus are mostly incoherent from event to event.

A similar set of analyses were performed on the 8 Yucca Flat events (Figure 2). The direction and speed of propagation (apparent velocity) of this initial P-wave from these events was essentially the same as for the Pahute Mesa events. The coda also arrived with the same apparent velocity. However, as Figure 7 shows, the relative power and coherency of the coda arrivals are much lower. Despite the greater degree of similarity of the initial P-waves, there is still significant variation in time and amplitude of distinct coda arrivals from event to event. This is demonstrated by the upper trace in Figure 6 which shows the phased sum of the beams. The amplitude of the P-wave is 0.97 in this case, whereas coda is reduced by a factor of approximately 2.5, again suggesting that the coda arrivals are uncorrelated from event to event. There was no indication of significant arrivals with velocities other than that of the initial P-wave, in particular PcP.

Articles in the literature on the generation of seismic codas are legion. Discounting contributions by other phases such as pP, sP, PcP etc., published mechanisms fall into the following categories:

- (i) multiply reflected phases originating in the crust and upper mantle under the source and/or the receiver
- (ii) reflections and refractions of P-waves taking place out of the diametrical plane

- (iii) P-wave scattering of the Chernov type at the source and/or receiver
- (iv) mode conversions, namely P-to-Rayleigh waves at the receiver and Rayleigh to P-wave at the source
- (v) tectonic release including aftershocks and other source related phenomena.

Of these mechanisms, the nature of the codas themselves as discussed eliminates all possibilities with the exception of those which generate coda in the immediate proximity of the source. It is well known that explosions at NTS, particularly those at Pahute Mesa, generate considerable SH wave radiation in some instances. If coda generation is due to tectonic release, those events with high coda levels should also be correlated with events with large SH excitation. Table 3 shows the Love to Rayleigh wave amplitude ratios from seismograms recorded at 5 SDCS stations within the continental United States, for the 8 Pahute Mesa events and 6 of the Yucca Flat events. There is no obvious correlation between events having high coda levels and events with large L/R ratios. Furthermore, the Pahute Mesa events with coda/P-wave ratios of 0.5 would require aftershocks of approximately magnitude 6 to account for the observed coda levels. Although we have not examined the very near-in records for these events, there is no evidence in the literature to suggest that such events are triggered 18 to 20 seconds after similar large explosions.

Therefore, we are left with mechanisms (i), (iii) and (iv) to consider. Furthermore, reflections in a plane-layered structure can also be eliminated, because such reflections would be well-correlated, though possibly time-shifted, from event to event within the two source regions. We are inclined to discount the Chernov mechanism, because, strictly speaking, this theory is only applicable to small random variations in elastic parameters. Because of the size of the coda arrivals, a second-order or strong-scattering theory would be required. Thus we are left multiple

reflections from curved boundaries which lead to the formation of caustics of the type discussed by Hong and Helmberger (in press), and Rayleigh to P-wave conversions in the immediate vicinity of the source.

In an effort to further resolve this problem, seismograms of teleseismic events recorded by SDCS stations located within NTS are being examined. Preliminary results show that a Russian event at Novaya Zemlya generated unusually complex seismograms at NT-NV, which is within Pahute Mesa, a much simpler one at OB2NV, located in the nearby Climax Stock. Filtering of these and other seismograms from deep events will be used to determine whether these codas are primarily body or surface waves. In any case these data provide strong additional support for the conclusion that scattering near the source is the primary mechanism for coda generation associated with explosions at NTS. Structural complexities beneath Pahute Mesa are especially effective compared to other test sites in generating large and variable coda levels.

Table 1  
Epicenter Data For Pahute Mesa Events

Event	Date	Location	Origin Time	Depth (m)	$m_b$ (USGS)
STILTON	3 Jun 75	37:20:24.21N 116:31:22.36W	14:20:00Z	731	5.9
KASSERI	28 Oct 75	37:17:24.18N 116:24:41.57W	14:30:00Z	1265	6.4
INLET	20 Nov 75	37:13:29.83N 116:22:03.22W	15:00:00.1Z	817	6.0
MUENSTER	3 Jan 76	37:17:47.58N 116:19:59.47W	19:15:00.0Z	1451	6.2
FONTINA	12 Feb 76	37:16:17.07N 116:29:18.40W	14:45:00.2Z	1219	6.3
CHESHIRE	14 Feb 76	37:14:33.49N 116:25:12.76W	11:30:00.2Z	1167	6.0
ESTUARY	9 Mar 76	37:18:35.87N 116:21:51.19W	14:00:00.1Z	889	6.0
COLBY	14 Mar 76	37:18:21.58N 116:28:17.34W	12:30:00Z	1273	6.3
POOL	17 Mar 76	37:15:21.20N 116:18:42.89W	14:15:00.1Z	879	6.1

Table 2

## Epicenter Data For Yucca Flat Events

Event	Date	Location	Origin Time	Depth (m)	$m_b$ (USGS)
MIZZEN	3 Jun 75	37:05:41.39N 116:02:09.98W	14:40:00.1Z	637	5.7
STANYAN	26 Sep 74	37:07:57.5N 116:04:06.2W	15:05:00.2Z	---	5.6
ESCABOSA	10 Jul 74	37:04:30.1N 116:01:54.6W	16:00:00.1Z	640	5.7
LATIR	27 Feb 74	37:06:15.3N 116:03:10.2W	17:00:00.1Z	641	5.8
CHIBERTA	20 Dec 75	37:07:39.53N 116:03:41.64W	20:00:00.2Z	716	5.7
TOPGALLANT	28 Feb 75	37:06:22.32N 116:03:22.51W	15:15:00.1Z	713	5.7
STARMORT	26 Apr 73	37:07:23.0N 116:03:30.6W	17:15:00.2Z	564	5.6
STRAIT	17 Mar 76	37:06:26.22N 116:03:08.91W	14:45:00.1Z	780	5.8

Table 3  
PAHUTE MESA L/R RATIOS

Event/Sta.	RK-ON	CPSO	WHZYK	FN-WV	HN-ME	M <sub>b</sub>	CODA	C/P
Kasseri	0.39	0.86	0.87	1.12	6.74	6.4	H	0.5
Muenster		0.82	1.31	0.99	4.71	6.2	H	0.4
Pool		0.90	1.06	0.90	3.86	6.1	L	0.25
Cheshire	0.43	0.48	0.73	0.78	1.85	6.0	L	0.2
Fontina		0.42	0.92	0.61	1.93	6.3	H	0.3
Colby		0.16	0.28	0.18	0.26	6.3	H	0.5
Inlet	0.87	1.02	0.63	1.28	1.56	6.0	L	0.2
Estuary	0.30	0.62	0.72	0.70	1.87	6.0	H	0.45

This Table illustrates variability of tectonic release among events in Pahute Mesa and the lack of correlation between large tectonic release and teleseismic coda levels as observed at NORSAR. H denotes high coda levels and L denotes low coda levels.

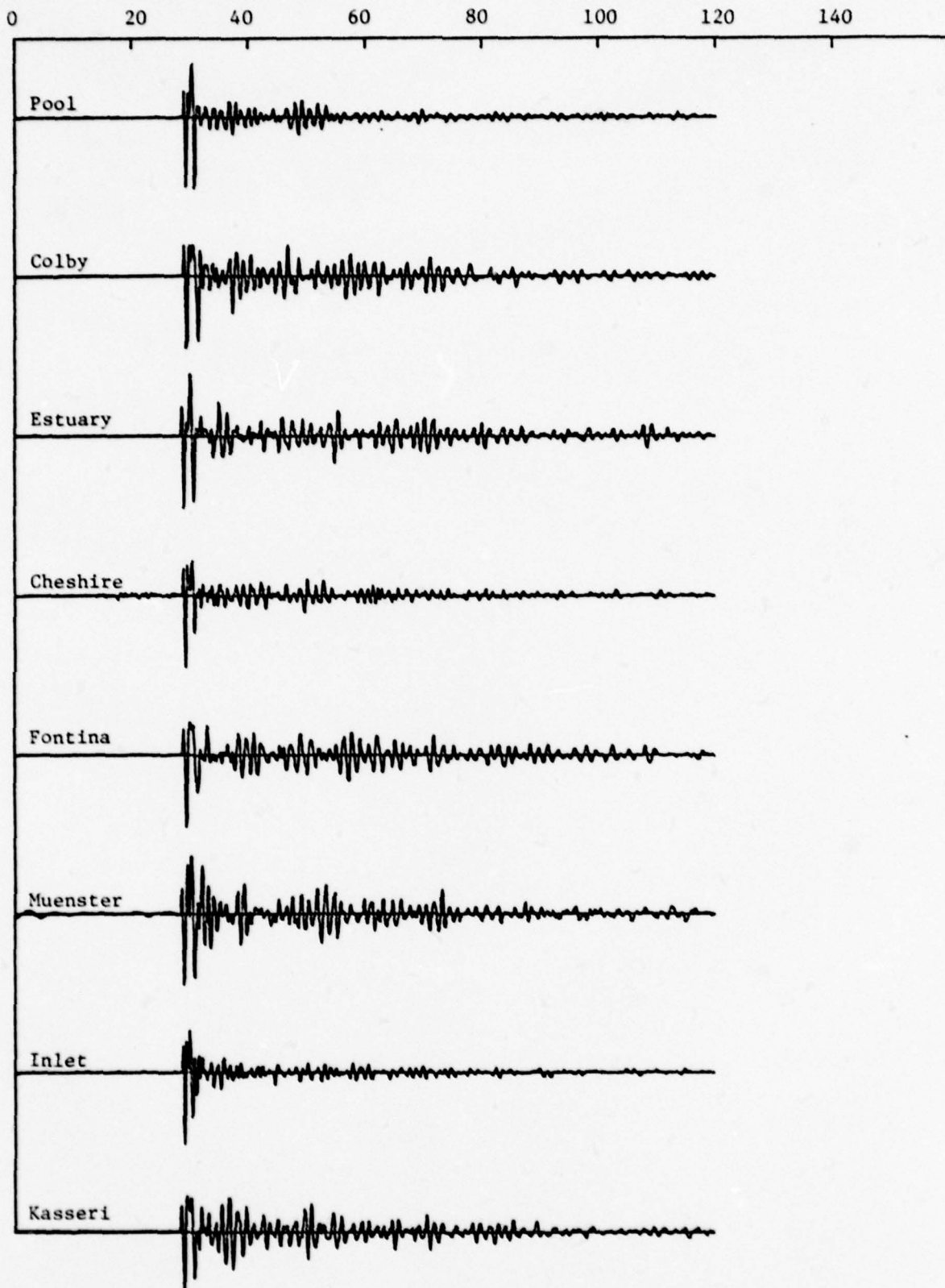


Figure 1. P-wave velocity beams for 8 Pahute Mesa events recorded at NORSAR. Numbers to right give maximum value in millimicrons.

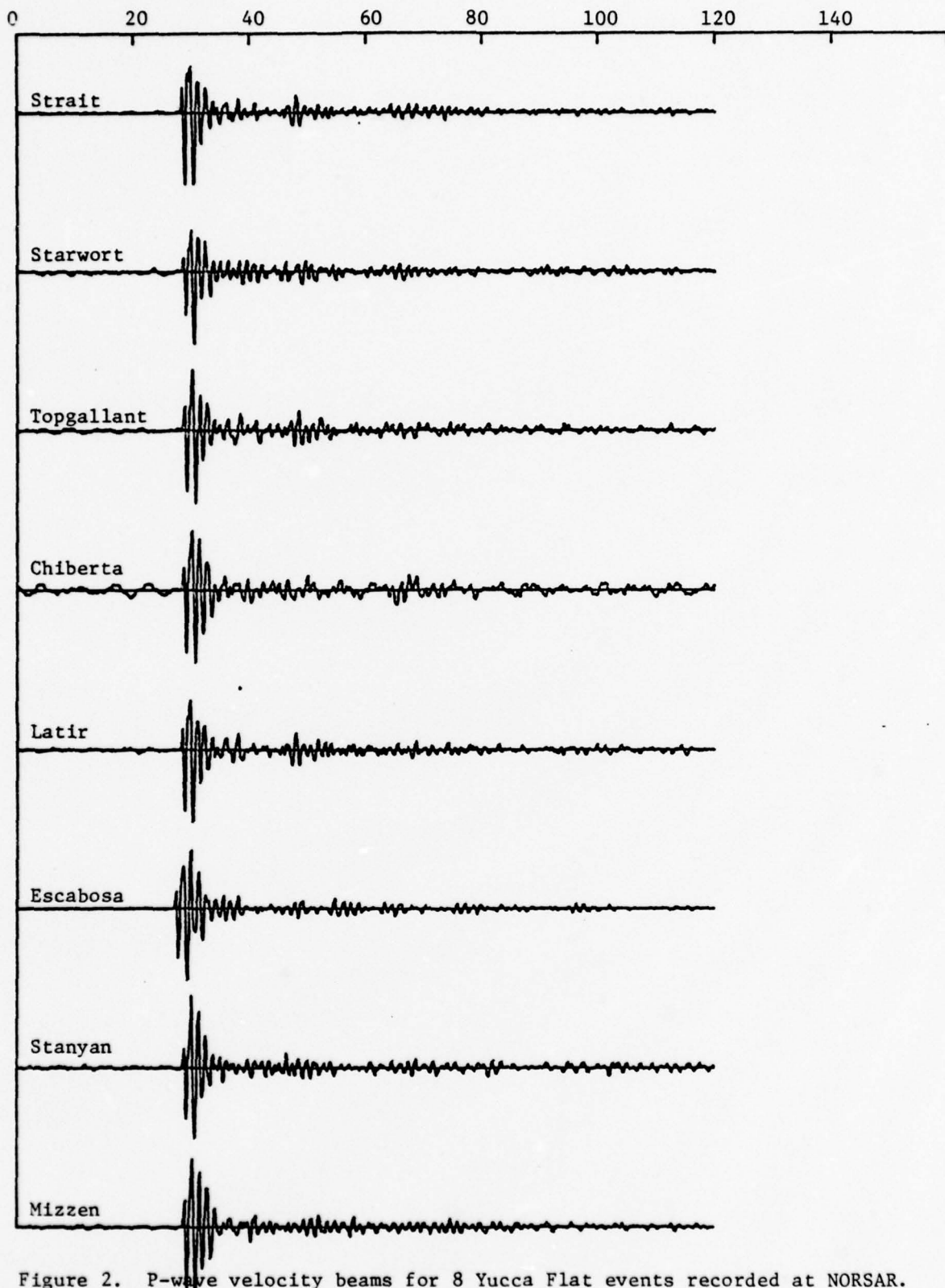


Figure 2. P-wave velocity beams for 8 Yucca Flat events recorded at NORSAR. Numbers to right give maximum value in millimicrons.

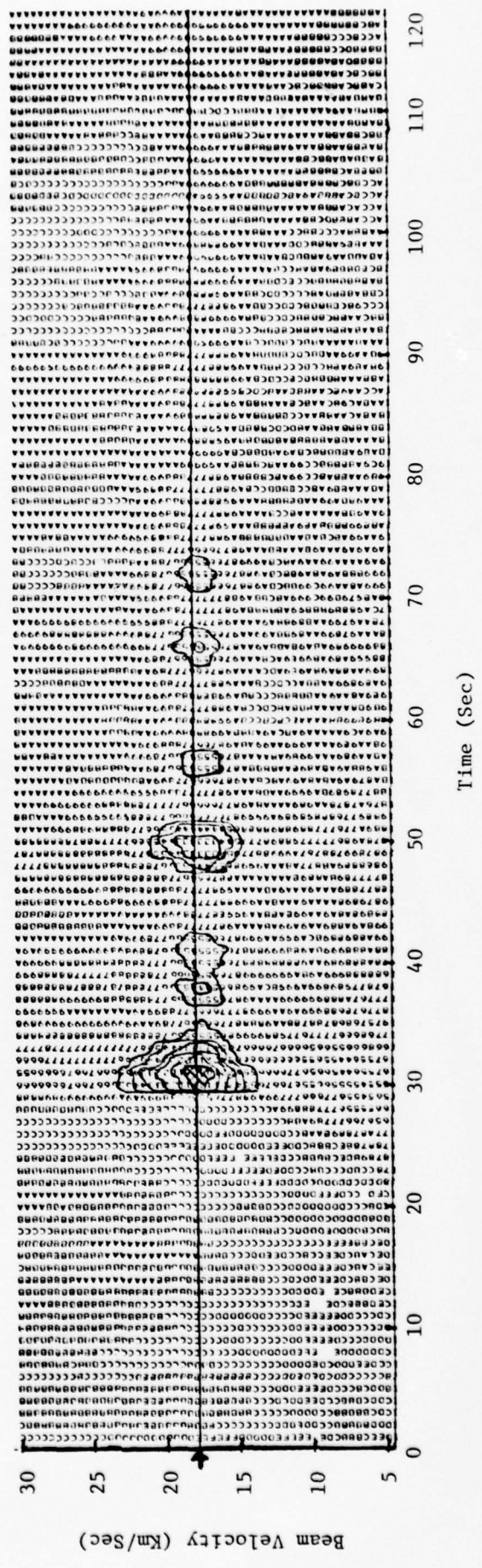
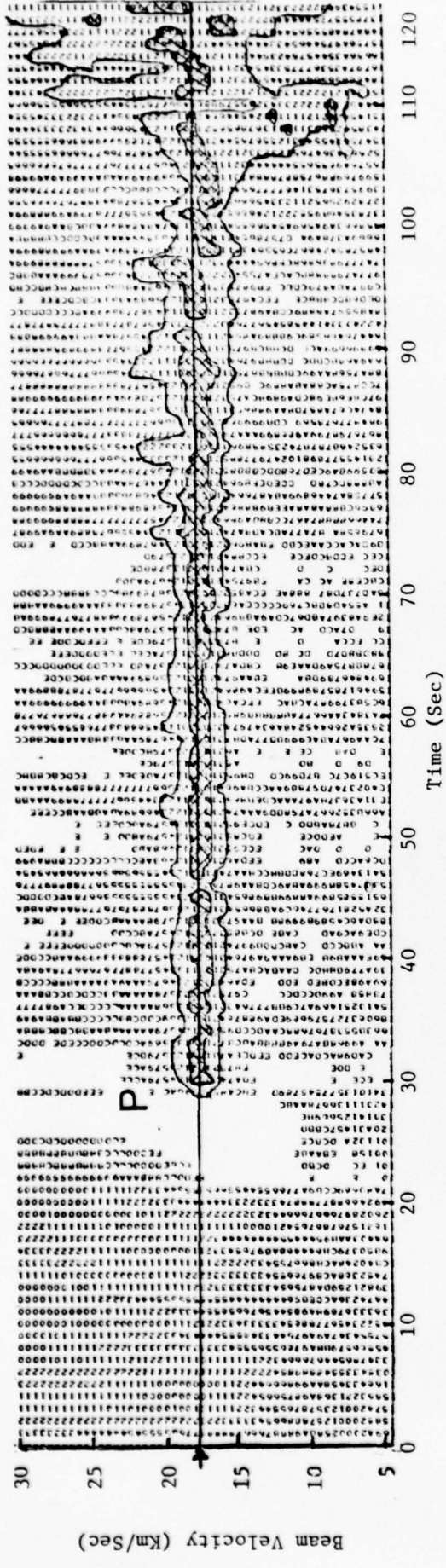


Figure 3. Relative power as a function of time and beaming velocity for STILTON. Power plot is contoured in 3 db intervals. For upper plot, which is normalized to maximum power in a 2 second window, only -1 and -3 db contours are shown. Figure 4c shows the beamed seismogram at STILTON.

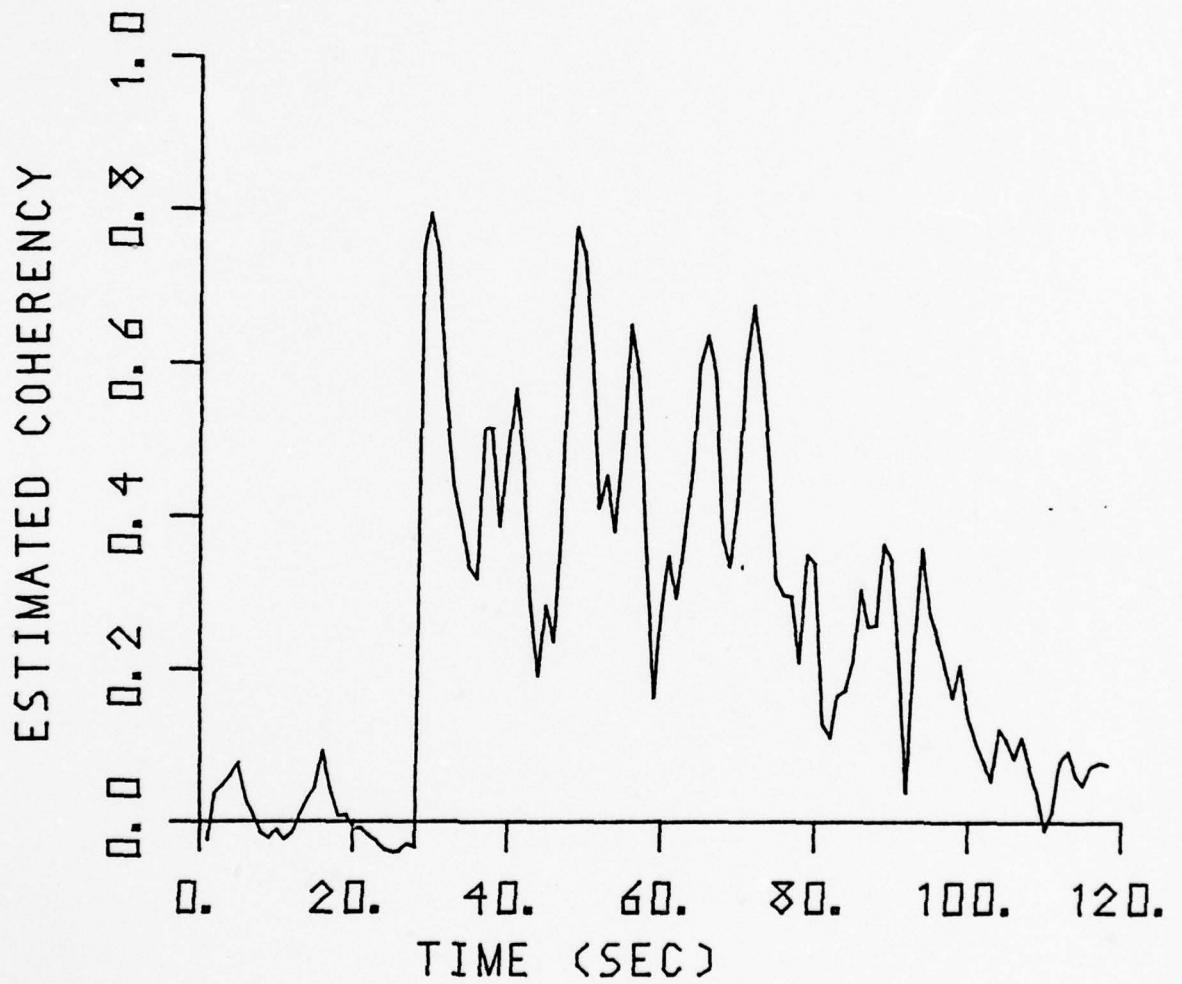


Figure 4a. Coherency of best beam for Pahute Mesa event STILTON (see Figure 4c for beamed seismogram).

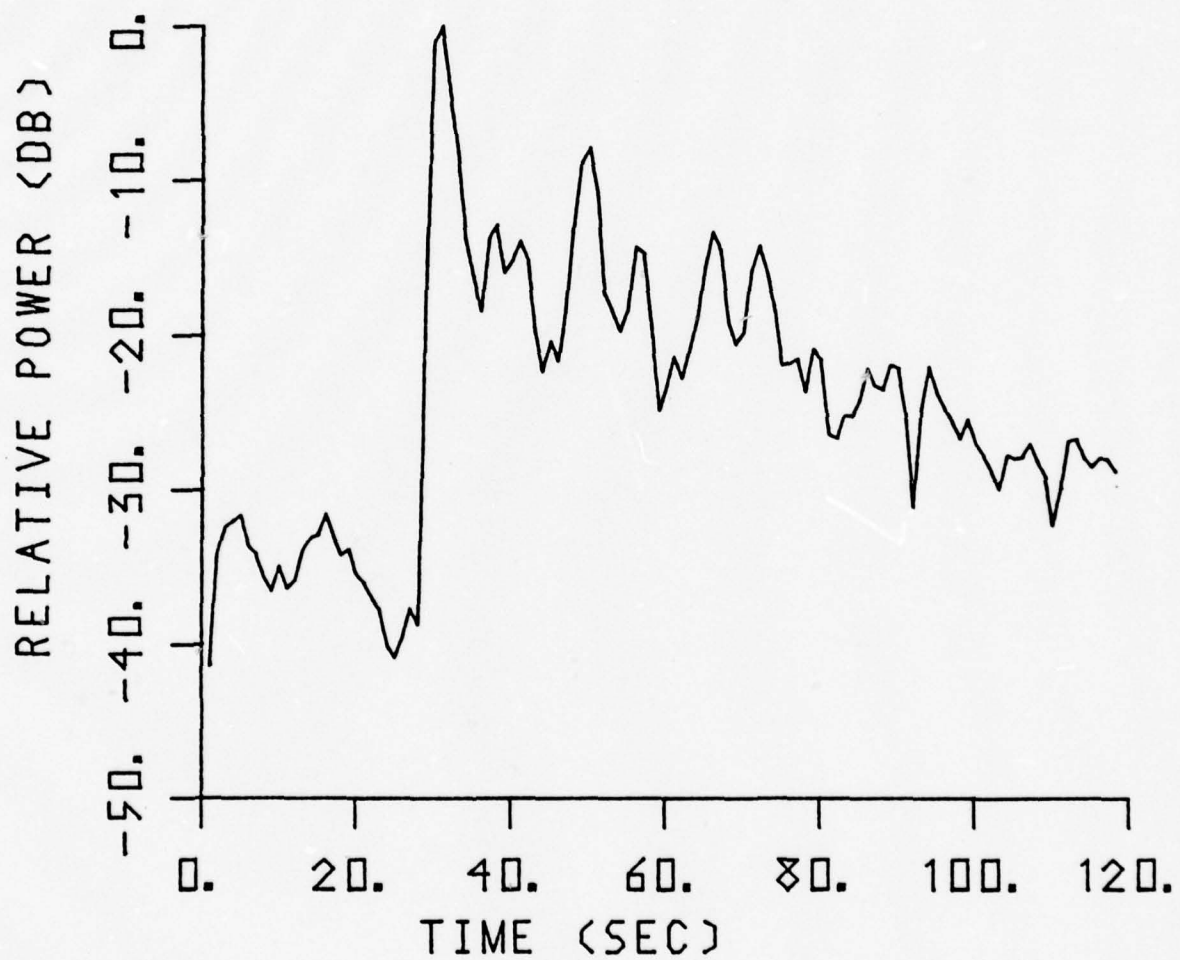


Figure 4b. Relative power of best beam for Pahute Mesa event STILTON (see Figure 4c for beamed seismogram).

APPENDIX D

Determination of Focal Parameters for the Oroville, California  
Sequence of August, 1975 Using Synthetic and  
Seismic Research Observatory Data

by

Robert W. Tifft

and

S.S. Alexander

Geophysics Program  
Geosciences Department  
The Pennsylvania State University  
University Park, Pa. 16802

## INTRODUCTION

Conventional body wave fault plane solutions for a seismic event inherently contain considerable scatter. A wide azimuthal distribution of body wave first arrivals is generally necessary in order to minimize this scatter. Fault plane solutions for events of the August, 1975 Oroville, California sequence have been determined by several groups of investigators. These solutions are both numerous and overlapping.

The main event ( $M_L = 5.7$ ) of the Oroville, California sequence occurred in a region of historically low seismicity approximately 10 kms. south of the 4 billion cubic meter man-made Lake Oroville. The sequence began seven years after the onset of filling but only one month after its most rapid filling. The largest event prior to this sequence was an event in 1940, also a magnitude 5.7, about 50 kms. north of the town of Oroville. Twenty-one foreshocks ( $M_L > 1.6$ ) preceded the main event beginning on June 28, 1975. There were approximately 300 aftershocks recorded by local stations and arrays from an area 14 by 10 kms. southeast of Oroville through August 11, 1975.

The purpose of this investigation was to more clearly define the focal mechanisms of the layer events of this sequence. The approach utilized was the synthesis of long period Love and Rayleigh waves whose time domain signatures and frequency domain

spectra were then compared with the regionally observed signatures and spectra recorded at the Seismic Research Observatory (hereafter SRO) in Albuquerque, New Mexico. The focal parameters, namely source depth, strike azimuth, fault plane dip and slip were perturbed in order to obtain the best correlation between the synthetic and observed surface wave signatures and spectra.

Two fault plane solutions were determined which would synthesize the observed signatures and spectra fairly well as recorded at the SRO station in Albuquerque. One solution corresponded to the sequence of foreshocks, main event, and some aftershocks, whereas, the second solution, which had a distinctly different source depth and orientation, corresponded to the aftershock on August 6, 1975.

#### METHODS

A suite of ten events ( $M_L > 4.3$ ) which were digitally recorded at the SRO station in Albuquerque was obtained for the Oroville, California sequence. This suite consisted of foreshocks to the main event on August 1, 1975, the main event, and the aftershocks through August 6, 1975. Locations for some of these events are shown in the map of the Oroville area of Figure 1. These long period digital recordings were sampled at one sample per second. These digital recordings were amenable to rather easy computer manipulations such as time scale changes, gain changes, rotation and Fourier analysis.

Figures 2 through 4 are the vertical, radial and transverse components, respectively, of four of these events recorded at Albuquerque. The scale factors are indicated by each trace. Note that the  $M_b$  5.8 mainshock is clipped.

The synthetic seismograms were generated assuming a plane parallel layered source structure. A three step computational scheme calculated the seismograms containing root periods ranging from 5 to 75 seconds. The resulting vertical, radial and transverse component seismograms were then compared visually to the rotated seismograms recorded at Albuquerque. The comparison was made by overlaying the observed signatures with the synthetic signatures, noting the goodness-of-fit of the relative amplitudes and duration of the individual wavelets comprising the seismograms. In addition, the Love and Rayleigh wave spectral ratios were compared as a function of frequency for the synthetic and observed events.

#### PROCEDURE FOR SYNTHESIS

The Fortran IV computer programs employed in the synthesis of surface waves propagated from Oroville, California to Albuquerque, New Mexico are the implementation of the theory developed by Harkrider (1964), Ben-Menahem and Harkrider (1964) and Harkrider (1970). The implementation required two runs of a series of three programs for the synthesis of Rayleigh and Love wave seismograms. A description of the input card formats can be found in the appendix of Alexander, et al. (1973).

An important assumption which was required to be made in this study was the specification of a suitable source structure for the Oroville area. The structure consisted of model 35 CM2 (Alexander, 1963) with the upper 33 kms. replaced by the structure determined by refraction profiles (Eaton, 1966). This upper section reflects the local geologic environment of valley sediments overlying Jurassic-Triassic metavolcanics (Ryall and Van Wormer 1975) in the Oroville region. The structure used in this study is shown in Figure 5 and tabulated in Table 1.

The dispersion programs were run first. They calculated the depth independent quantities such as phase velocities, group velocities and the amplitude response as a function of root period for Love and Rayleigh waves. The surface ellipticity was also calculated in the case of Rayleigh waves. The required input at this stage was the local source structure as given above as well as the specification of the periods at which roots were to be found. The periods ranged from 5 to 75 seconds in this study.

The output from the dispersion programs was used as the input to the punch programs. The punch programs calculated the displacement-stress quantities at specified depths in the source structure. The focal depths investigated in this study were 2, 3, 5, 7, 8, 9, 10 and 12 kms. which were consistent with the range of focal depths determined for the Oroville sequence by various investigators (see Table 2).

Outputs from both the dispersion and punch programs were then used as inputs to the step which computes the Rayleigh

and Love wave seismograms in a plane parallel layered structure. The synthetic seismograms that were computed were corrected for the instrument response of the SRO station in Albuquerque as shown in Figure 6. The attenuation coefficients employed were determined by Hermann and Mitchell (1975) for the interior of North America. These coefficient values contained considerable scatter and were therefore used only as a first approximation of the attenuation properties of the western United States. The values used in this study are tabulated in Table 3.

The additional input parameters utilized in the final step of the synthesis were those corresponding to the fault plane orientation, source type, source time function and epicentral distance. The fault plane orientations were specified following the convention of Ben-Menahem and Harkrider (1964). Synthetic Love and Rayleigh waves were computed utilizing a source function specified by either a point source or a double couple source. For the case of the double couple, the source time function was employed corresponding to a magnitude 5 event determined from Aki (1967).

#### EXPERIMENTS AND RESULTS

Numerous Rayleigh and Love wave seismograms modeling the Oroville, California events were synthesized using the aforementioned procedure. Published fault plane solutions of foreshocks, the main event and aftershocks listed in Table 2 served as a starting point for the solutions for the synthetic wave forms. The trial fault plane solutions employed in the synthesis were then perturbed to

cover the ranges of the published values.

The vertical, radial and transverse component synthetic seismograms were visually compared with a rotated event recorded at Albuquerque, New Mexico, both plotted with the same time scale (Figure 7). This event was a magnitude 4.7 (BRK) foreshock four hours prior to the August 1, 1975 magnitude 5.7 (BRK) Oroville sequence main event. The main event was not used for comparison in this study for two reasons. The surface wave coda of the main event was contaminated by the coda of a foreshock eight seconds prior to the main event. In addition, the wave form as recorded at Albuquerque was clipped (see Figures 2 through 4). This comparison of the synthetic and observed vertical, radial and transverse components permitted the rejection of many solutions as viable mechanisms for the observed wave forms. It was found that the depth of focus was not as sensitive in these eyeball matches of synthetic versus real waveforms as were the strike, dip and slip of the particular fault plane solution under scrutiny.

The depth of focus was localized by comparing the Love to Rayleigh wave spectral ratios for the synthetic and observed data as seen in Figure 8. The spectra of the observed data was obtained by employing the usual Fourier techniques. The peak in the synthetic Love to Rayleigh wave ratio was observed to shift to lower frequencies as the depth of focus was increased.

The best fitting synthetic seismogram employed a double couple extended source function. The fault plane parameters which yielded this best fit with the foreshock were azimuth,  $N 10^{\circ} W$ ;

dip,  $60^{\circ}$  W; slip,  $90^{\circ}$ . The slip angle of  $90^{\circ}$  is consistent with the angle listed in the figures,  $270^{\circ}$ . This angle is specified in the convention of Ben-Menahem and Harkrider (1964) and represents a normal dip slip mechanism. In this case the Great Valley block has moved down with respect to the Sierra Nevada block. The depth determined by spectral ratios was 5 kilometers. The epicentral distance from Oroville to Albuquerque used in this analysis was 1426 kms. The Rayleigh and Love waves computed with this fault plane solution also compared favorably with several other aftershocks of the Oroville sequence. It was therefore concluded that the main event could also be characterized by this fault plane solution.

Further examination of the aftershock data for the Oroville events revealed some marked changes in the recorded waveforms (see Figures 2 through 4). The changes in the observed waveforms for the August 6, 1975 aftershock were adequately modeled utilizing a different fault plane solution than that determined above. A set of approximate fits was chosen from the original suite of synthetic seismograms. Again, the depth was localized using the Love to Rayleigh spectral ratios. The focal parameters which best modeled the August 6 aftershock were azimuth, N  $0^{\circ}$  W; dip,  $40^{\circ}$  W; slip,  $90^{\circ}$ ; and depth 10 kms. These results can be seen in Figures 9 and 10.

#### DISCUSSION

The results of this study indicate that it is possible to determine the source mechanisms of regional-teleseismic events

utilizing broad band data recorded at only a few high quality stations. The Seismic Research Observatory network, of which there are ten installations in current operation, supply such high quality data. In this study Love and Rayleigh wave data from only one station were used.

The fault plane solutions determined in this study were found to be in good agreement with the range of solutions published previously. The change in focal parameters between the foreshock and aftershock of August 6 could be associated with the development of a non-uniform local stress distribution following the mainshock. The method employed in this study was found to be quite sensitive to small changes in fault plane parameters as seen in the two additional waveforms in Figure 9. Therefore, this approach may be of significant help in determining fault plane solutions of regional events when station coverage is poor, provided that an appropriate source structure can be provided.

In conclusion, it must be emphasized that the proper propagation structure should be employed in the synthesis of surface waves. This study revealed the rather fortuitous result that the propagation path structure was identical to the source structure given in Figure 5. Additional theoretical seismograms shown in Figures 11 and 12 which did not match the observed waveforms were synthesized using the focal parameters determined above. The source structure remained the same as used previously, but the propagation path was that of 35 CM2 (Alexander, 1963). It is quite evident that this change does not produce satisfactory results.

## References

- Aki, K. (1967). Scaling law of seismic spectrum, *J. Geophys. Res.* 72, 1217-1231.
- Alexander, S. S. (1963). Surface wave propagation in the western United States, Ph.D. thesis, California Institute of Technology, Pasadena.
- Alexander, S. S. D. W. McCowan and P. Glover (1973). Effects of source structure and site response of ground motion in the mean field of earthquakes, Final technical report of Grant # N22-125-72 (6). NOAA.
- Ben-Menahem, A., and D. G. Harkrider (1964). Radiation patterns of seismic surface waves from buried dipolar point sources in a flat stratified earth, *J. Geophys. Res.* 69, 2605-2620.
- Eaton, J. P. (1966). Crustal structure in northern and central California from seismic evidence, *Calif. Div. Mines and Geol. Bull.* 190, 419-426.
- Harkrider, D. G. (1964). Surface waves in multilayered elastic media I. Rayleigh and Love waves from buried sources in a multilayered elastic half-space. *Bull. Seism. Soc. Am.* 54, 627-679.
- Harkrider, D. G. (1970). Surface waves in multilayered elastic media II. Higher mode spectra and spectral ratios from point sources in plane layered earth models. *Bull. Seism. Soc. Am.* 60, 1937-1987.
- Hermann, R. B. and B. J. Mitchell (1975). Statistical analysis and interpretation of surface-wave anelastic attenuation data for the stable interior of North America, *Bull. Seism. Soc. Am.* 65, 1115-1128.
- Lahr, K. M., J. C. Lahr, A. G. Lindh, C. G. Bufe and F. W. Lester (1976). The August 1975 Oroville earthquakes, *Bull. Seism. Soc. Am.* 66, 1085-1099.
- Langston, C. A. and R. Butler (1976). Focal mechanism of the August 1, 1975 Oroville earthquake, *Bull. Seism. Soc. Am.* 66, 1111-1120.
- Morrison, P. W., B. W. Stump, and R. Uhrhammer (1976). The Oroville earthquake sequence of August 1975, *Bull. Seism. Soc. Am.* 66, 1065-1083.
- Ryall, A. and J. D. Van Wormer (1975). Field-seismic investigation of the Oroville, California earthquakes of August, 1975, *Calif. Div. Mines and Geol. Spec. Report* 124, 139-145.

Table 1  
Oroville Structure

Thickness, kms.	Alpha km/sec.	Beta km/sec.	Rho gm/cm <sup>3</sup>
2.0	3.75	1.72	2.20
3.0	5.90	3.40	2.80
5.0	6.80	3.88	3.03
5.0	6.80	3.88	3.03
5.0	6.80	3.88	3.03
5.0	6.80	3.88	3.03
8.0	6.80	3.88	3.03
8.0	8.00	4.40	3.26
8.0	8.00	4.40	3.26
7.5	8.09	4.65	3.37
7.5	8.09	4.65	3.37
10.0	7.96	4.56	3.42
10.0	7.96	4.56	3.42
10.0	7.84	4.48	3.43
10.0	7.84	4.48	3.43
10.0	7.82	4.43	3.44
10.0	7.82	4.43	3.44
20.0	7.86	4.41	3.45
20.0	7.92	4.39	3.46
20.0	7.97	4.40	3.48
20.0	8.03	4.41	3.52
100.0	8.51	4.66	3.58

Table 2

## Fault Plane Solutions of the Oroville Sequence

Events	Fault Plane Solutions				H(km)	Comments	Reference
	$\theta$	$\delta$	$\lambda$				
Aftershocks in northern section (see Fig. 1)	N10°W-N20°E	40°W	-	-	-	upper hemisphere projections	Morrison et al. (1976)
Aftershocks in west central section (see Fig. 1)	N60°W-N30°W	30°W	-	-	-	upper hemisphere projections	Morrison et al. (1976)
Aftershocks	N3°E±3°	60°W	-	10	-	Hypocenter determination using P wave first motions	Lahr et al. (1976)
Mainshock August 1, 1975	N0°W	65°W	70°	5.5±1.5	-	P wave first motions and waveform synthesis	Langston and Butler (1976)
Foreshock 8 sec prior to mainshock	N9°W	normal dip slip	-	-	-	P wave first motions	Ryall and Van Wormer (1975)
Aftershocks prior to August 8, 1975	N7°W	59°W normal dip slip	-	4-6	-	P wave first motions	Ryall and Van Wormer (1975)
Foreshocks Aug. 1, 1975	N10°W	60°W	90°	5	-	Surface wave synthesis	This study
Mainshock Aug. 1, 1975							
Aftershock Aug. 2, 1975							
Aftershock Aug. 6, 1975	N0°W	40°W	90°	10	-	Surface wave synthesis	This study

Table 3

## Attenuation Coefficients used in the Synthesis \*

Period	Rayleigh $\times 10^{-4}/\text{km}$	Loye $\times 10^{-4}/\text{km}$
75	2.10	1.20
70	2.00	1.15
65	1.90	1.05
60	1.75	0.95
55	1.60	0.90
50	1.50	0.80
45	1.35	0.70
40	1.30	0.60
35	1.30	0.55
30	1.25	0.50
25	1.25	0.40
20	1.25	0.30
19	1.30	0.25
18	1.35	0.25
17	1.40	0.20
16	1.45	0.25
15	1.50	0.25
14	1.60	0.35
13	1.80	0.45
12	1.90	0.65
11	2.10	1.20
10	2.30	2.30
9	2.70	3.50
8	3.30	4.70
7	5.00	5.90
6	6.10	7.00
5	7.20	7.60

\* From Hermann and Mitchell (1975)

## Figure Captions

- Figure 1 Location map of the Oroville, California region indicating some of the epicenters of the sequence. From Morrison et al. (1976).
- Figure 2 Long-period vertical component signals recorded at the Albuquerque, New Mexico SRO station (AMNO) for 4 events from Oroville, California in August, 1975. Relative signal strength is indicated by scale factors Z max. The mainshock (bottom trace) is clipped.
- Figure 3 Long-period radial component signals recorded at the Albuquerque, N. M. SRO station (AMNO) for 4 events from Oroville, California in August, 1975. Relative signal strength is indicated by scale factors R max. The mainshock (bottom trace) is clipped.
- Figure 4 Long-period transverse component signals recorded at the Albuquerque, N. M. SRO station (AMNO) for 4 events from Oroville, California in August, 1975. Relative signal strength is indicated by scale factors T max. The mainshock (bottom trace) is clipped.
- Figure 5 Plot of the Oroville structure employed for the synthetic seismograms of this study. Values are tabulated in Table 1.
- Figure 6 Amplitude response of the Seismic Research Observatory station in Albuquerque, New Mexico.
- Figure 7 Comparison of the observed (SRO) and theoretical signals at Albuquerque, N. M. for the August 1, 1975 Oroville foreshock. Source parameters for the theoretical waveforms are given in Figure 8.
- Figure 8 Comparison of observed and theoretical Love to Rayleigh spectral ratio (L/R) for the signal shown in Figure 7. The legend gives the source parameters (depth, strike, dip and slip) for the theoretical waveform synthesis.
- Figure 9 Comparison of the observed (SRO) and theoretical signals at Albuquerque, N. M. for the August 6, 1975 Oroville aftershock. Source parameters for the theoretical waveforms shown are given in Figure 10.
- Figure 10 Comparison of observed and theoretical Love to Rayleigh spectral ratio (L/R) for the signal shown in Figure 9. The legend gives the source parameters (depth, strike, dip and slip) for the theoretical waveform synthesis.

- Figure 11 Synthetic seismogram with same focal parameters and source structure as Figure 7. Propagation path structure is 35 CM2. Compare with Figure 7.
- Figure 12 Synthetic seismogram with same focal parameters and source structure as Figure 9. Propagation path structure is 35 CM2. Compare with Figure 9.

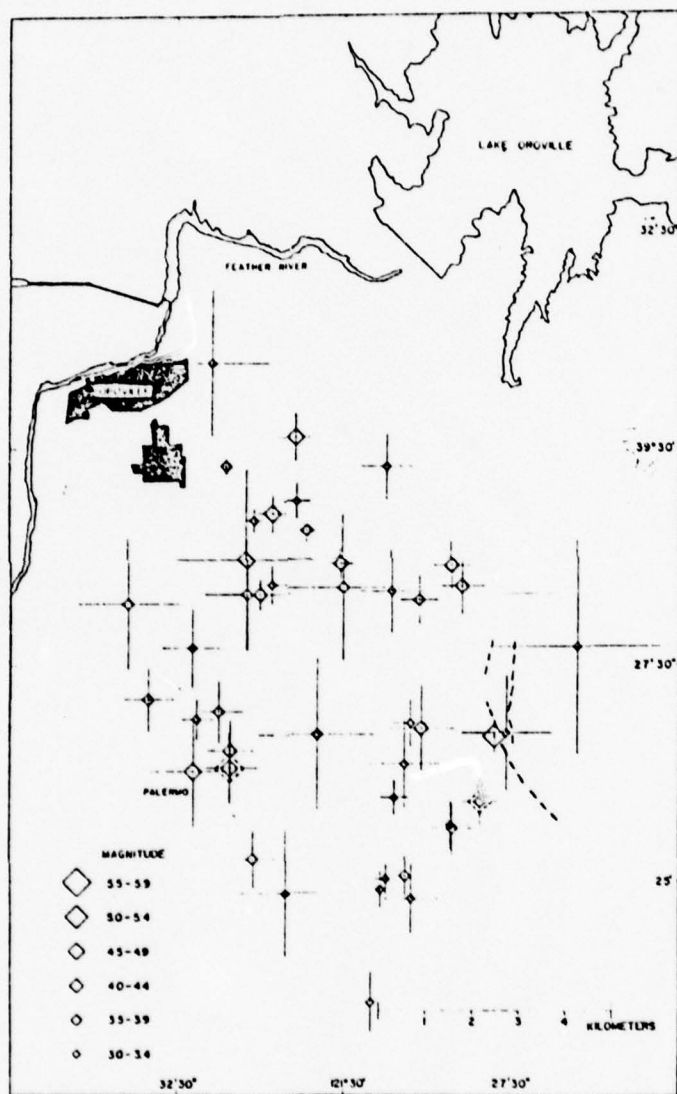


FIG. 4. Earthquake locations of the Oroville sequence. Standard errors in location estimated by least squares are indicated by bars through the epicenters. Dashed symbols represent earthquakes whose locations are assumed to be those of their immediate and masking foreshocks. The dashed lines indicate surface cracks observed after the main shock.

Figure 1

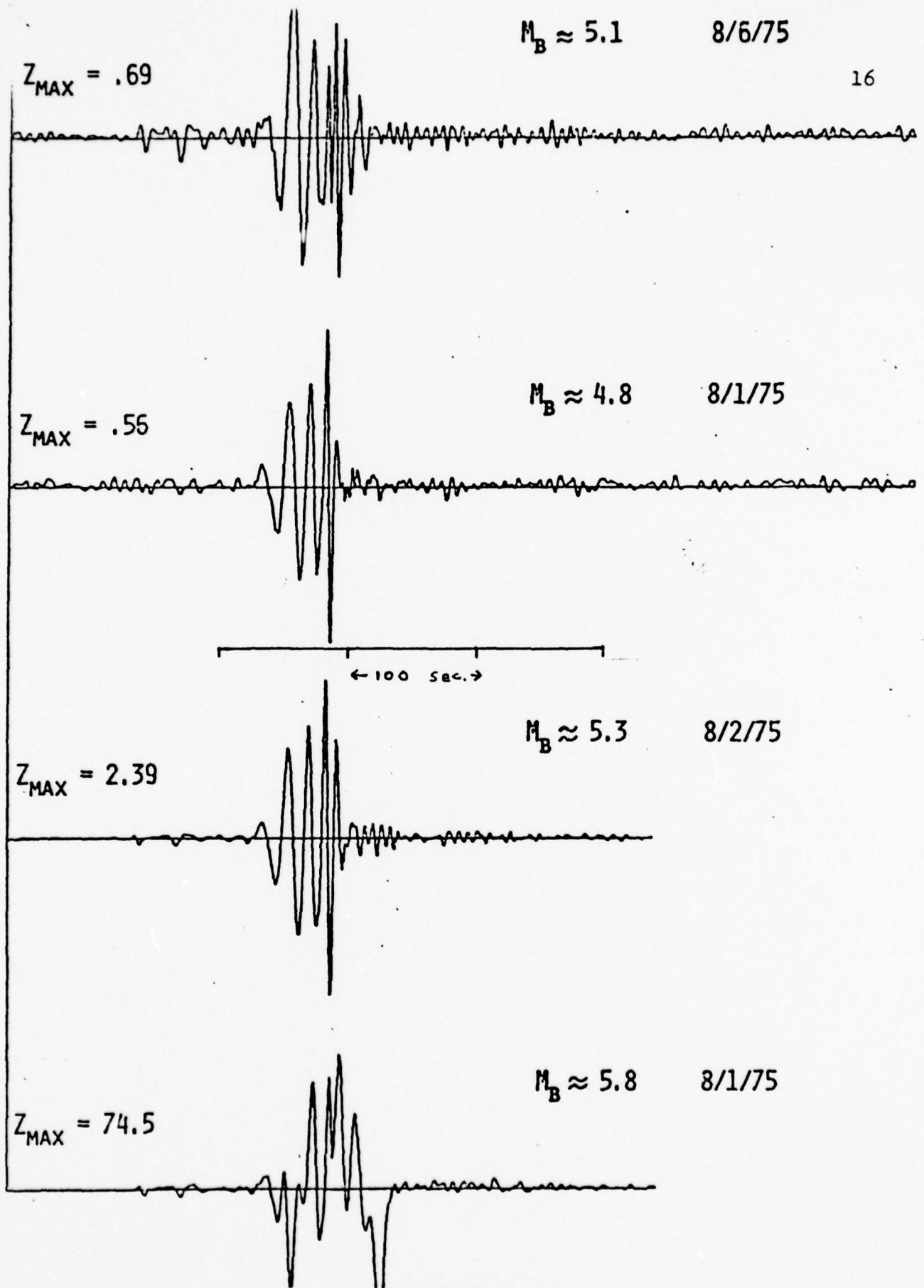


Figure 2

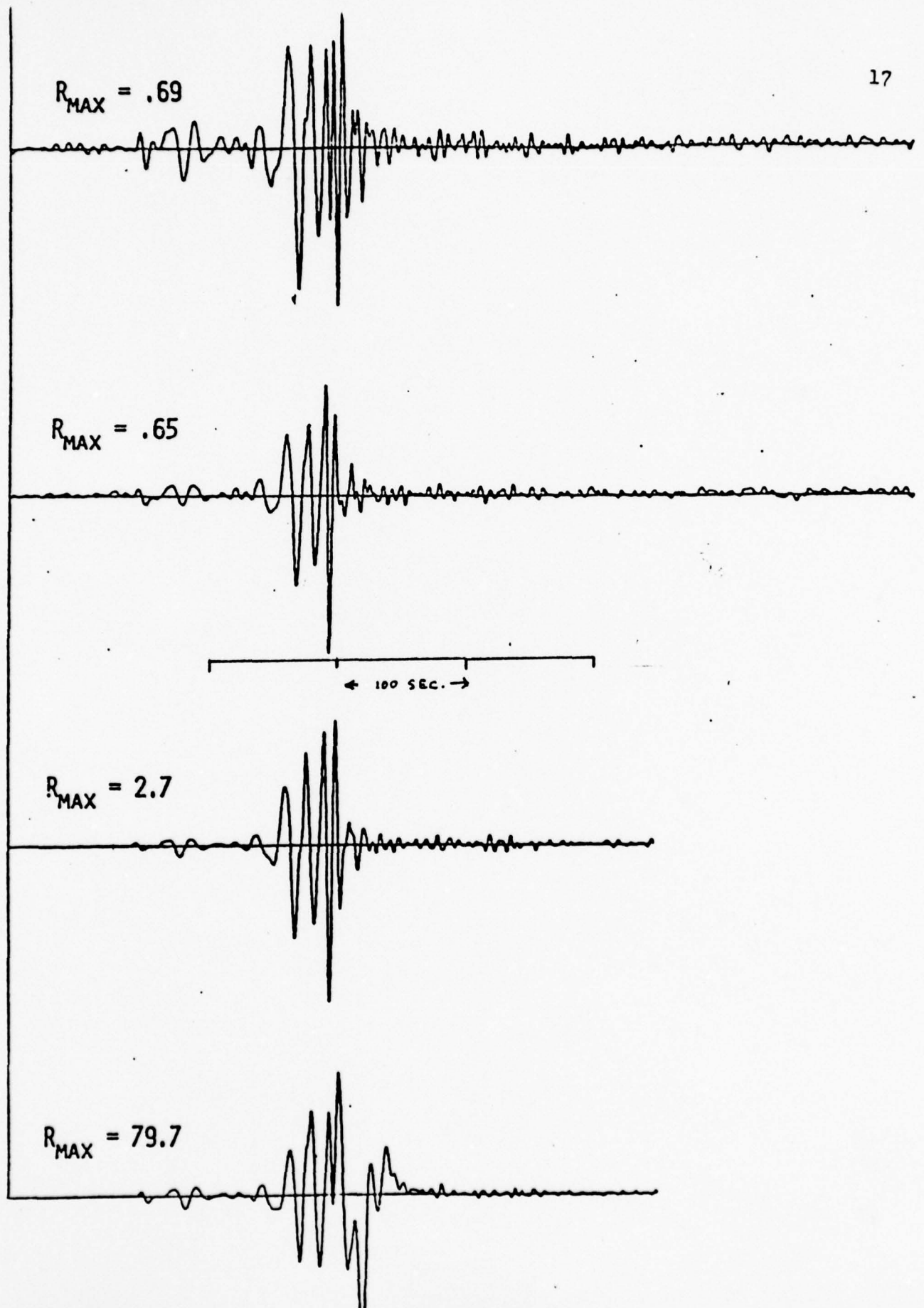


Figure 3

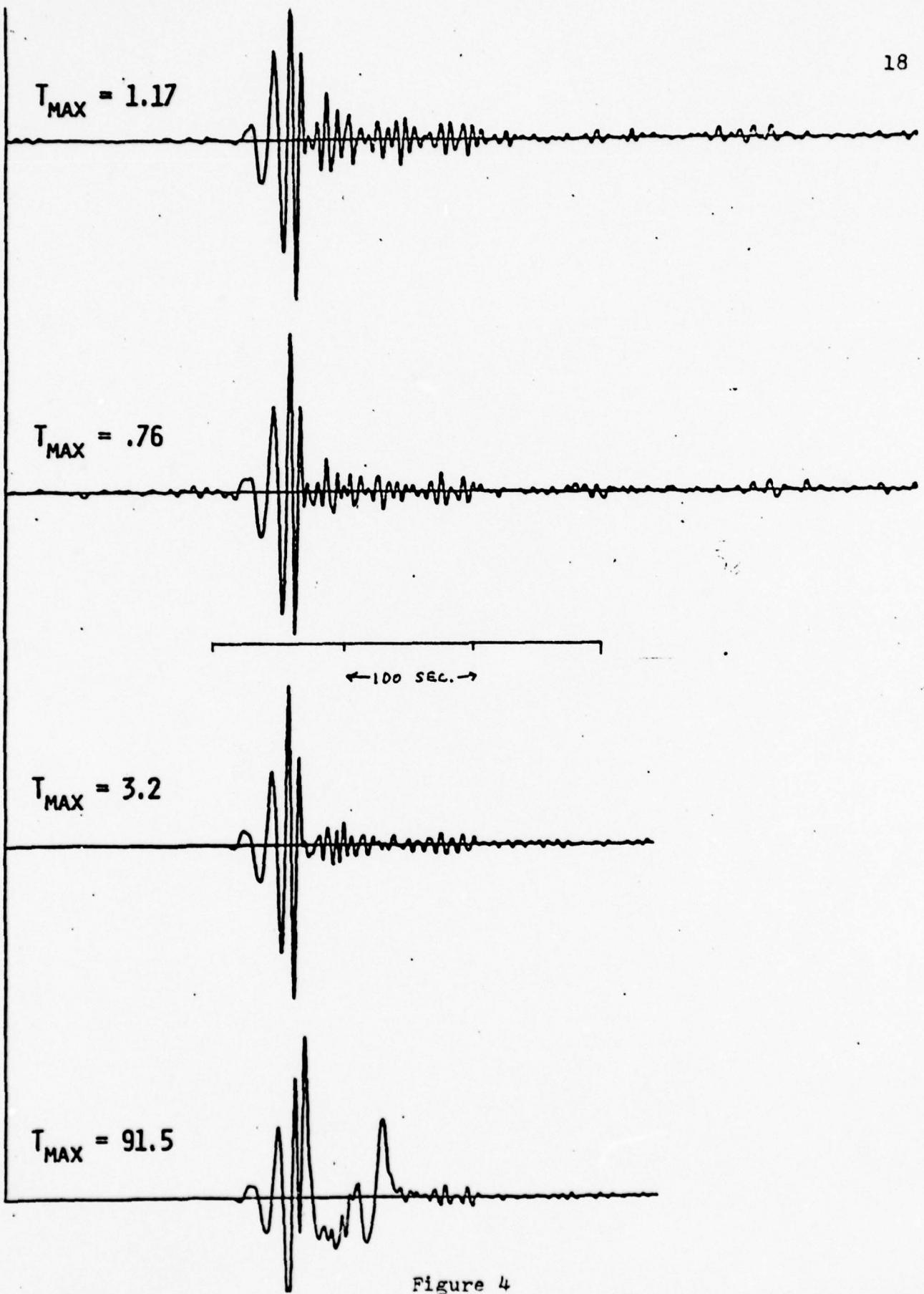


Figure 4

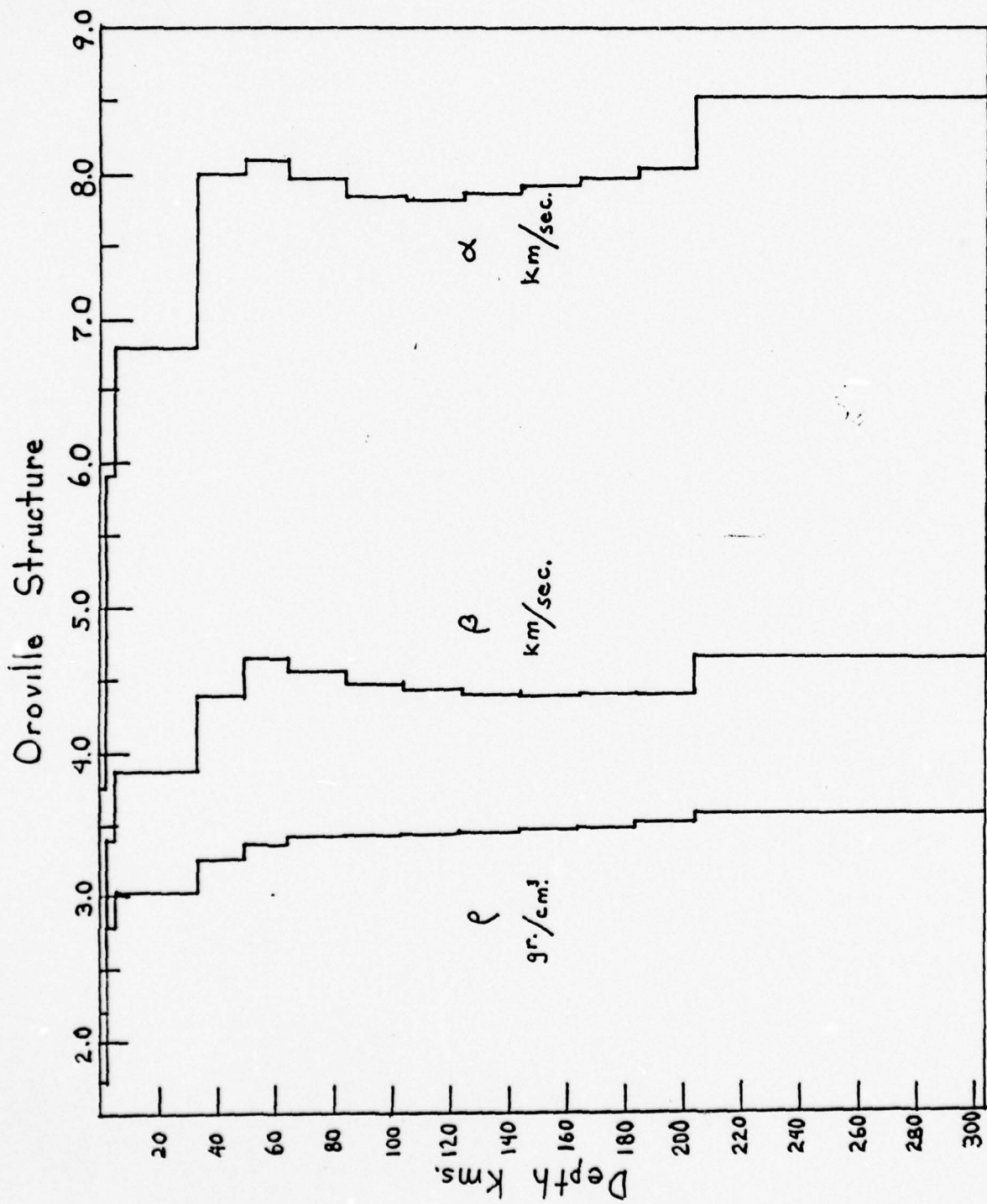


Figure 5

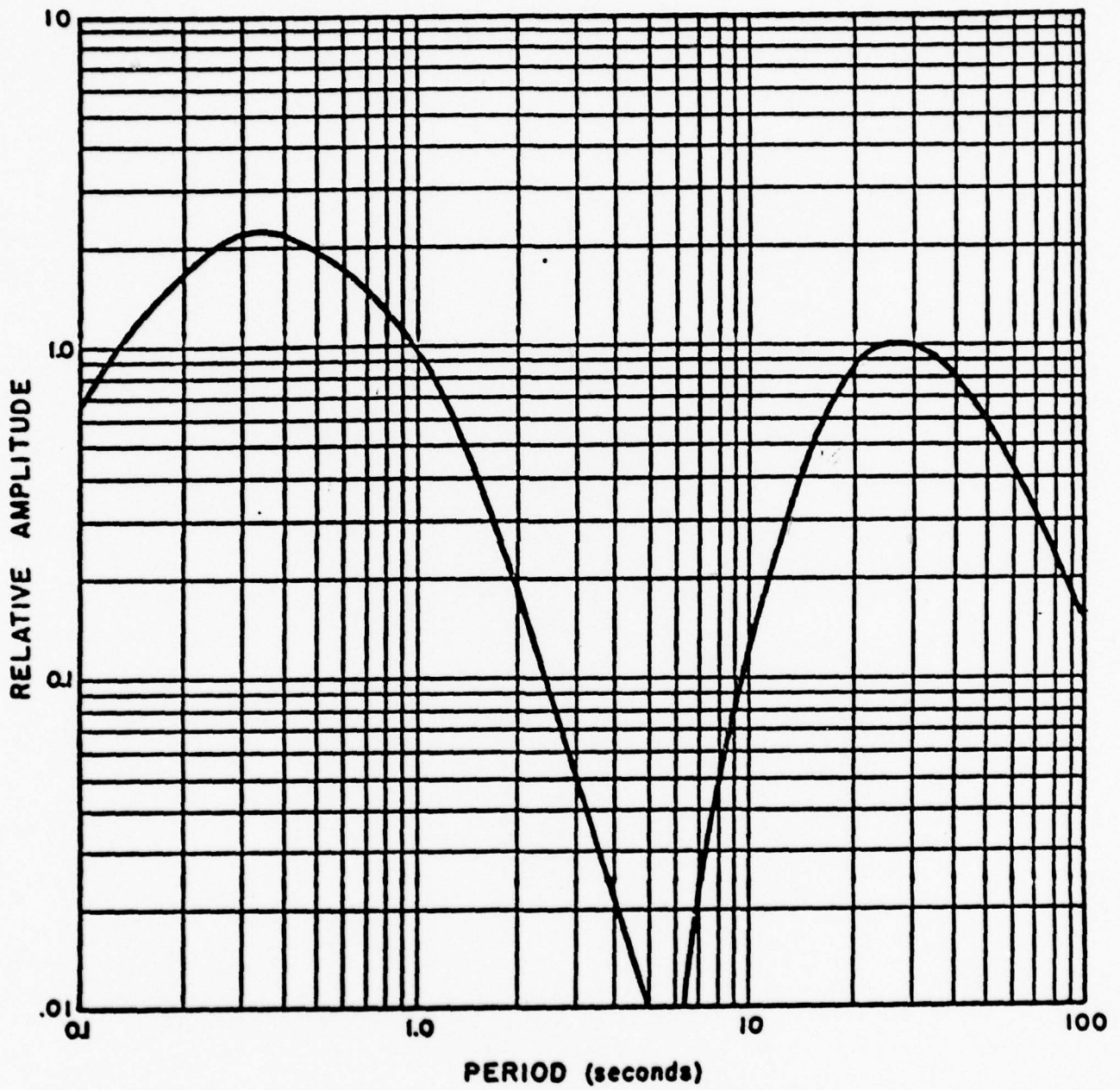


Figure 6

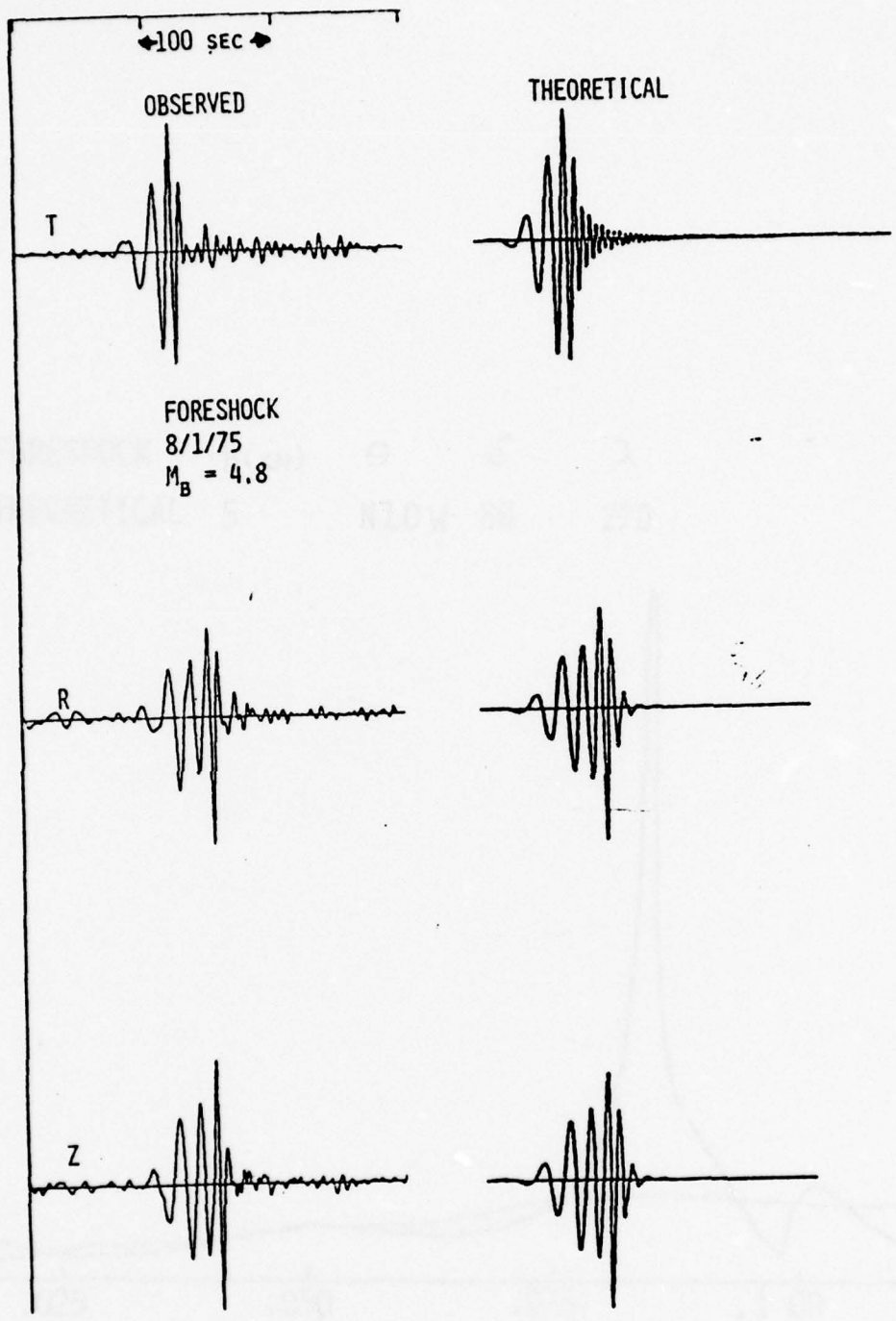


Figure 7

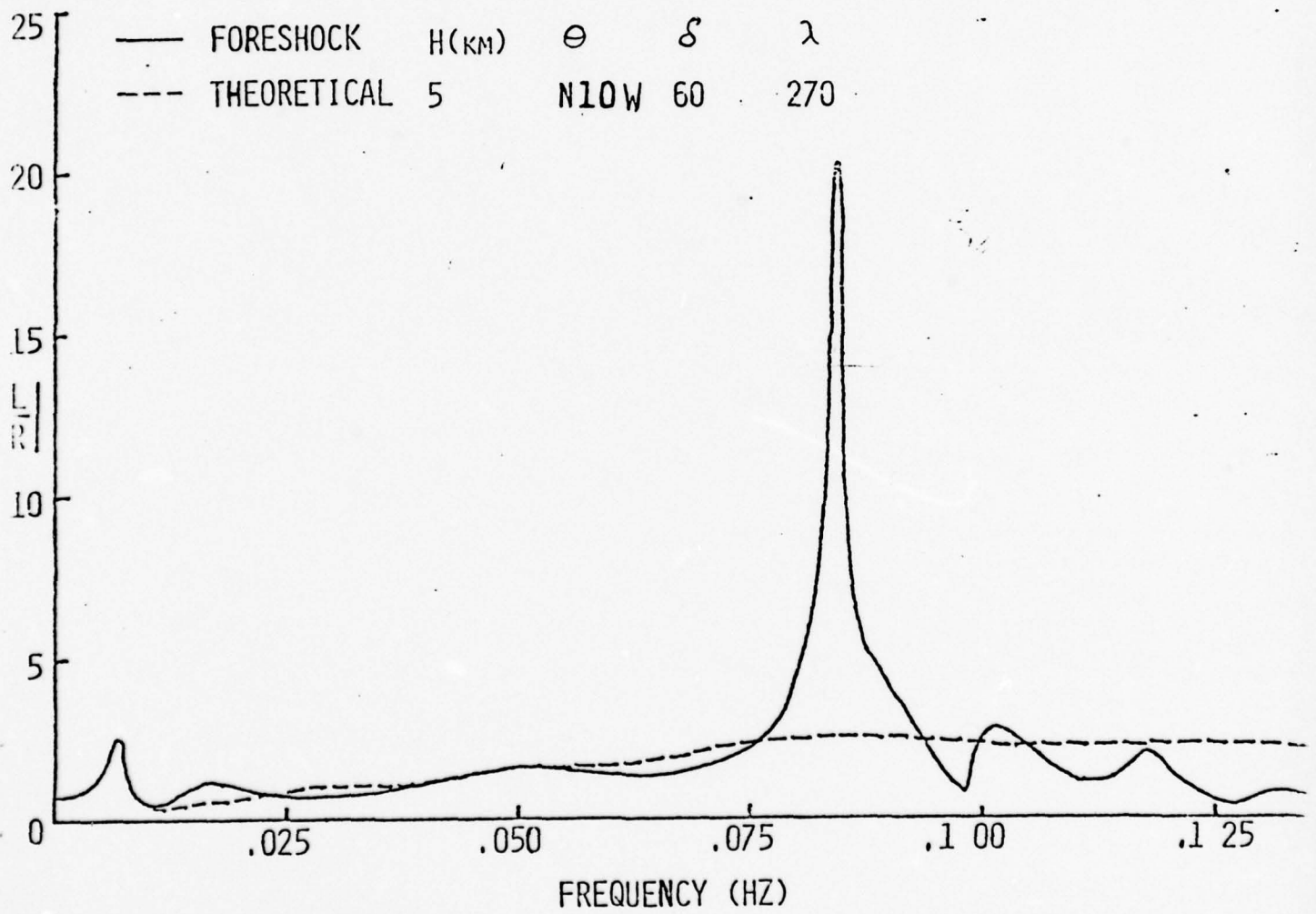


Figure 8

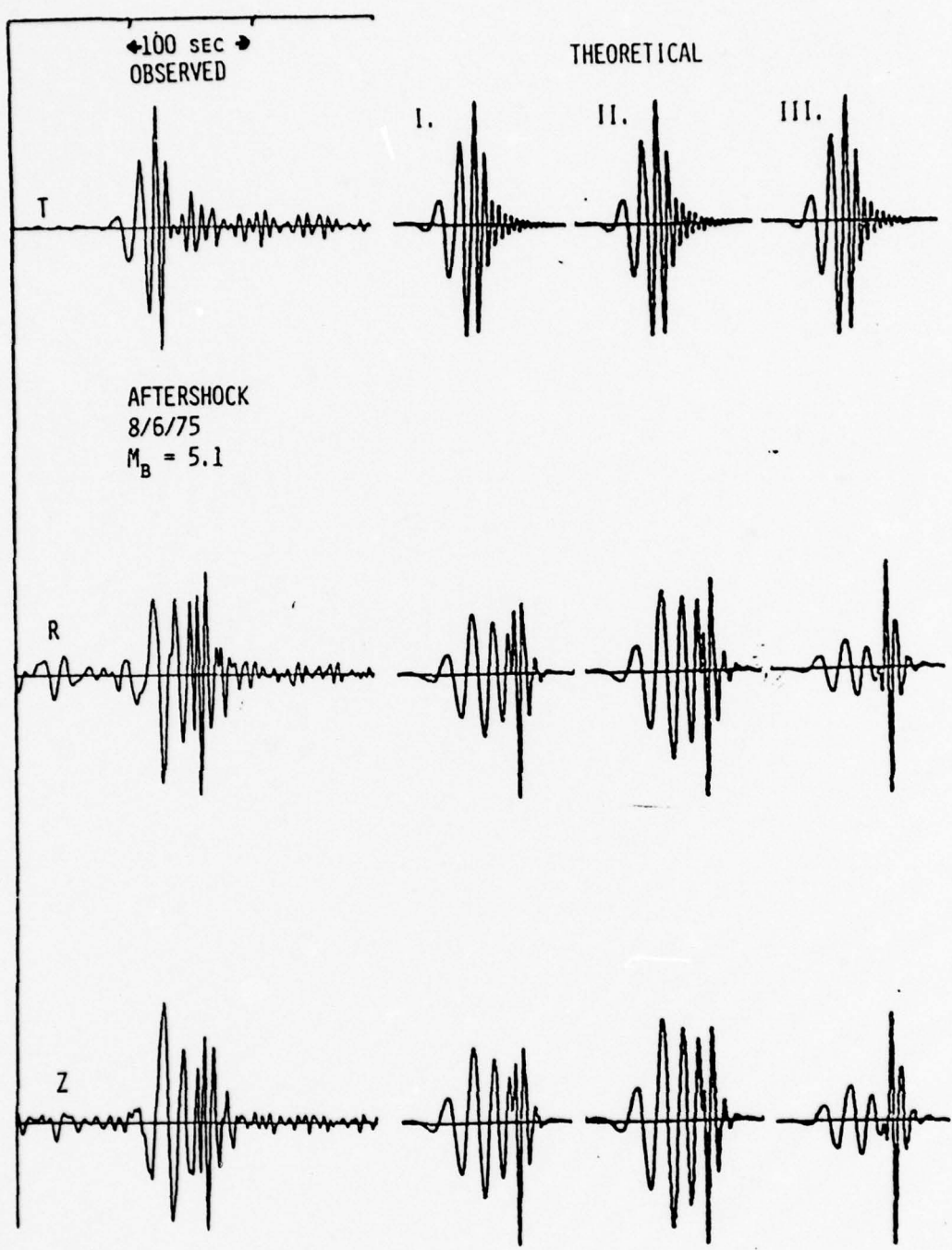


Figure 9

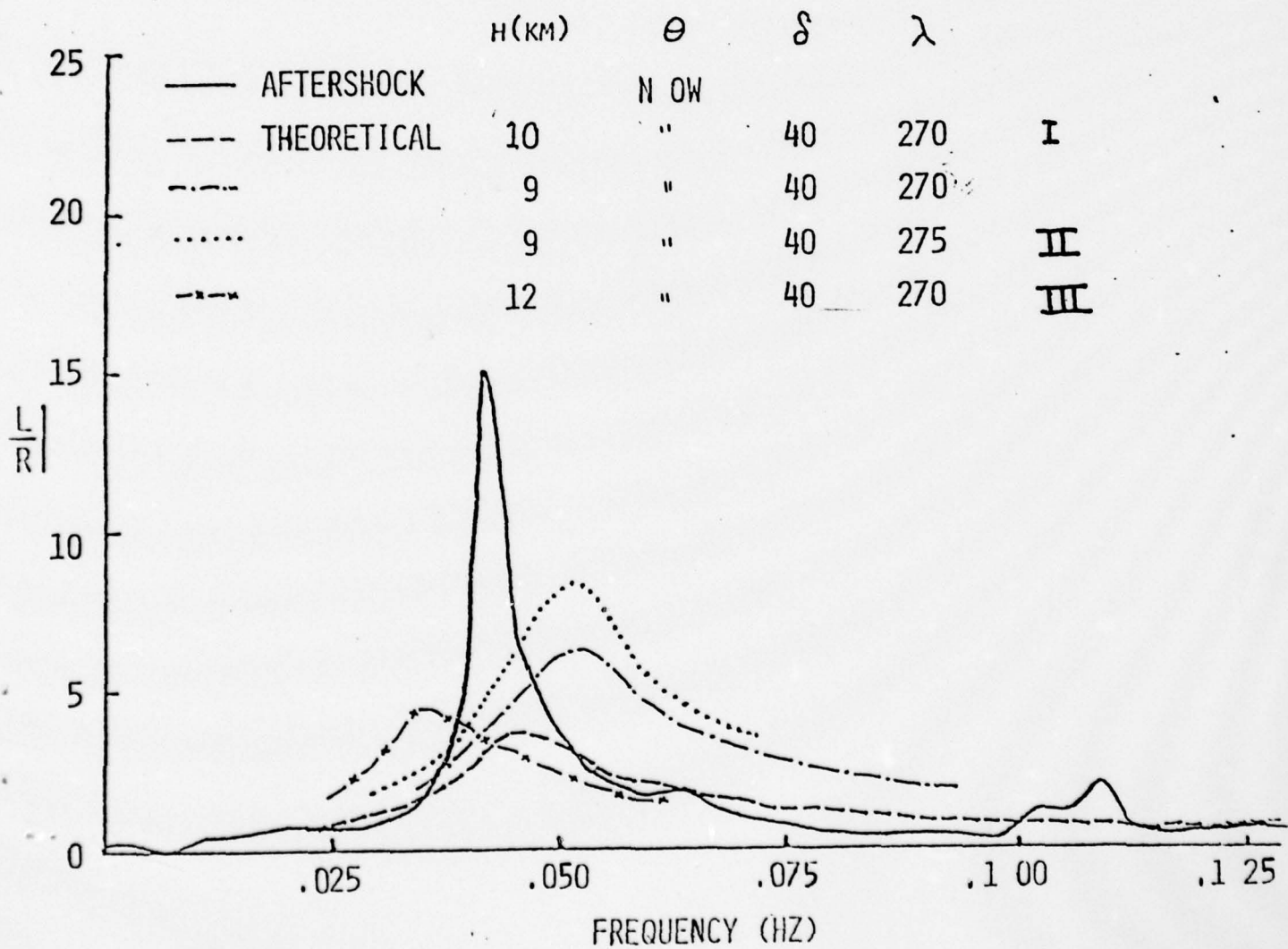
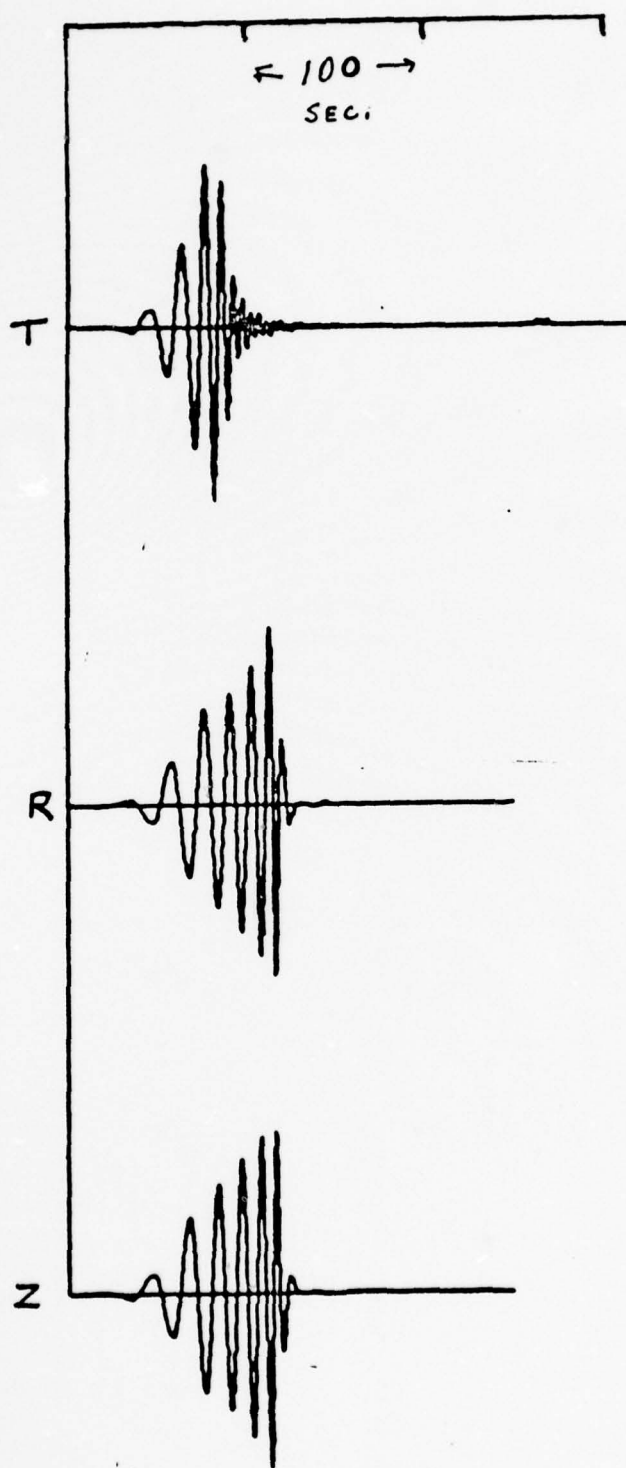


Figure 10



35 CM 2  
 $\theta = 64.2$   
 $\delta = 60^\circ W$   
 $\lambda = 270$   
 $h = 5$

Figure 11

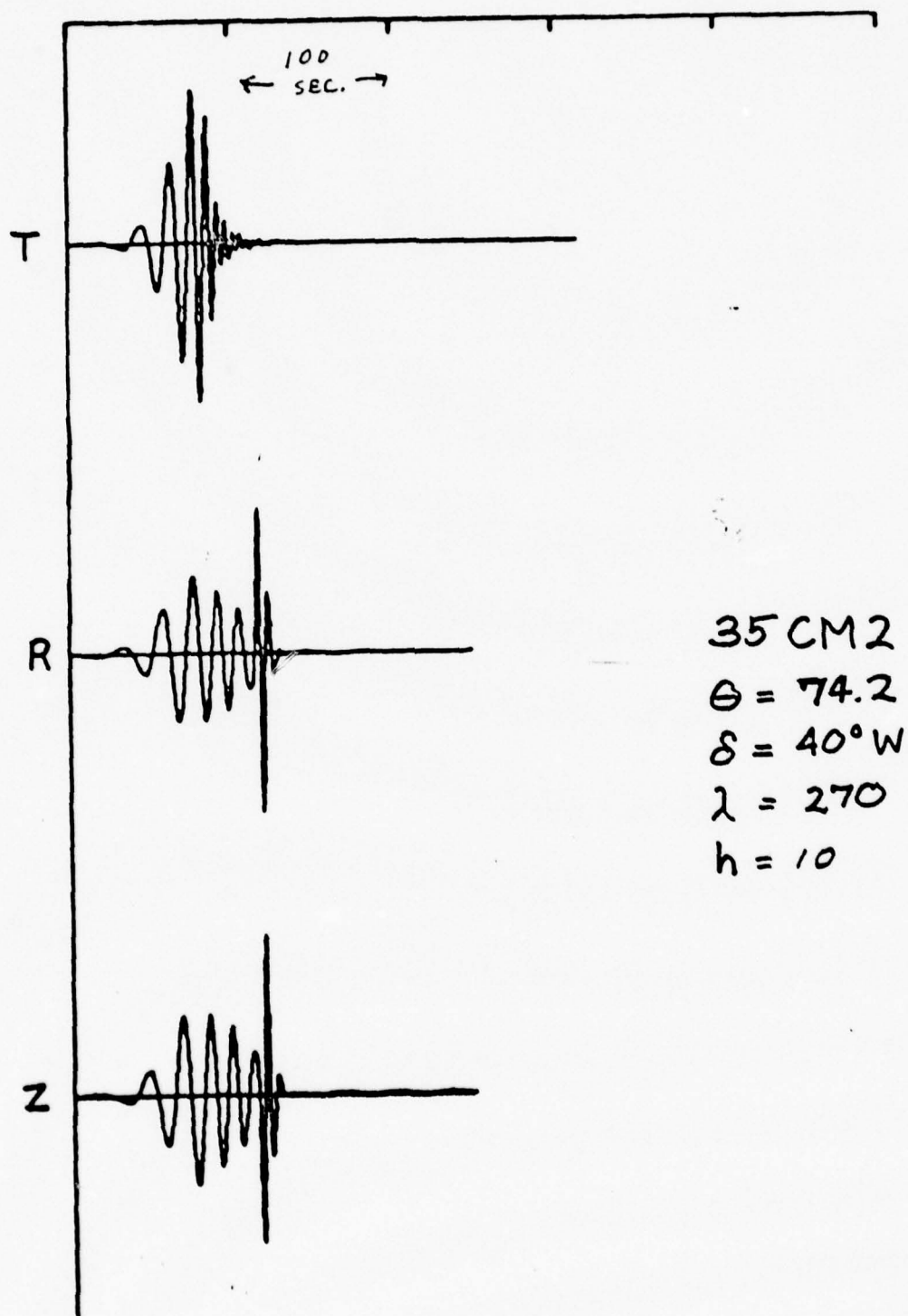


Figure 12

APPENDIX E

A CRUST AND UPPER MANTLE MODEL FOR NOVAYA ZEMLYA  
FROM RAYLEIGH WAVE DISPERSION DATA\*

by

Douglas W. McCowan  
Applied Seismology Group  
Lincoln Laboratory  
Massachusetts Institute of Technology  
Cambridge, Massachusetts 02142

Peter Glover  
Shelton S. Alexander  
Geosciences Department  
The Pennsylvania State University  
University Park, PA 16802

The views and conclusions contained in this document are those of the contractor and should not be interpreted as necessarily representing the official policies, either expressed or implied of the United States Government.

\*This work was sponsored by the Advanced Research Projects Agency of the Department of Defense at MIT Lincoln Laboratory and at The Pennsylvania State University through grant AFOSR 73-2515.

### Abstract

We derive a shear wave crust and upper mantle structure for the southern part of Novaya Zemlya by an application of the two event, single station method of Rayleigh wave phase velocity dispersion analysis. This method provides a means of isolating the surface wave dispersion characteristics of a remote source region using only teleseismic recordings. The observed phase velocity data are then systematically inverted to obtain a best-fitting model. Our preferred model has a 45 km thick crust with no shear wave low velocity zone in the upper mantle. It is similar to published structures for the southern Ural mountains and is therefore compatible with the premise that Novaya Zemlya is a northern extension of the Urals.

## Introduction

A sequence of large, presumed, explosions detonated at Novaya Zemlya between 1972 and 1975 generated unusually good Rayleigh wave seismograms. A set of five recordings of these explosions made at the Alaskan Long Period Array (ALPA) was used in an attempt to infer the crust and upper mantle structure of the source region. It appears from the epicenter information given in Table 1 that there are two distinct test sites on Novaya Zemlya. The furthest from ALPA is at the southern end of the lower island (see Figure 3). The nearer test site is located at the fiord separating the lower island from the rest of Novaya Zemlya. The average distance between the two test sites is 285 km.

Fortuitously, these two test sites lie nearly on a great circle path to ALPA (shown in Figure 2). A large portion of that path traverses the Arctic ocean basin neatly passing its way between the North American and Eurasian continental shelves. Since the propagation path to ALPA traverses relatively simple structures, we can expect the effects of anomalous propagation between the nearer test site and ALPA, that is along the common portion of the path, to be minimal.

The combination of the above factors affords the unique opportunity to isolate the phase velocity dispersion due to propagation in the source region itself. The method, due to Alexander (1969) and used by Taylor (1972) to study the mid-Atlantic ridge, is a modification of the usual two station, single event procedure (e.g., Glover & Alexander, 1969). However here, instead of finding the phase velocity dispersion between the two stations, the combination of one station and two events facilitates finding the phase velocity dispersion in

the source region.

#### Method

We first computed the array-averaged cross power spectrum for different north-south pairs of events at Novaya Zemlya using a group velocity window of 2.6 to 4.0 km/sec. Symbolically this is:

$$R(t) = \frac{1}{N} \sum_{j=1}^N \sum_{\tau} X_j(\tau) Y_j(t+\tau)$$
$$P(\omega) = \int R(t) e^{-i\omega t} dt \quad (1)$$

Here  $X_j$  and  $Y_j$  are the seismograms from the event pair recorded at the  $j^{\text{th}}$  ALPA sensor,  $R$  is the array-averaged cross correlation function, and  $P$  is the resulting cross power spectrum. This can then be expressed as an amplitude and phase:

$$P(\omega) = |P(\omega)| e^{i\phi(\omega)} \quad (2)$$

If the original seismograms contain common instrument and source phases, these cancel when computing the cross power spectrum.  $|P(\omega)|$  then becomes the average cross power and  $\phi(\omega)$  is related to the phase velocity in the source region,  $C(\omega)$ , by:

$$\phi(\omega) = \frac{\omega D_{\text{eff}}}{C(\omega)} \pm 2n\pi \quad (3)$$

where  $D_{\text{eff}}$  is the projection of the event separation on the great circle path shown in Figure 1. Our average event separation, 285 km, allowed us to pick the arbitrary integer easily by trial and error. An

earth structure model is then obtained by matching its phase velocity dispersion to that obtained by the data analysis.

Implicit in this analysis are the following four assumptions:

1. The source region can be characterized by an average plane layered structure
2. The Rayleigh waves from all events traverse a common path from the nearer (northern) events to the ALPA array
3. Interference due to multipathing can be neglected
4. The source phase for the two events is identical

#### Data Analysis

For this study we had five events, three northern and two southern. The pertinent epicenter information is given in Table 1 and ALPA center sensor seismograms are shown in Figure 4. As can be seen, these are all large explosions which excited sufficiently strong Rayleigh waves, despite their non-slip source mechanisms, so that low signal-to-noise ratios were not a problem. In order to remove location bias, all five events were relocated using P-waves observed at a common set of 35 stations. After constraining the depth of each event to zero, the areas of the resulting epicenter confidence error ellipses were all approximately  $1.6 \text{ km}^2$ . The relocation procedure was necessary because the resulting phase velocities are strongly dependent on the relative event separation. The PDE and relocated epicenters are plotted in Figure 3.

We read the WSSN film chips for all five events in our attempt to determine whether the source mechanisms were isotropic and explosive. We found between 21 and 29 readable LP polarities for each event all of which were compressional; i.e., up. There was no evi-

dence of anomalous amplitude patterns with azimuth indicative of significant strain energy release or of propagating ruptures. Furthermore, an examination of the long period horizontal WSSN records from a set of stations approximately  $40^{\circ}$  from Novaya Zemlya and well distributed in azimuth showed that no strong SH waves were excited by these events as is commonly the case from explosions at NTS.

The phase velocity data from the six possible north-south event pairs are shown plotted in Figure 5. The error limits are due to the observed spread in phase velocity at each frequency. It appears that some of this spread is the result of residual epicenter errors because data from each event pair tended to parallel that from the others. The rms error of the data over the band shown in Figure 5 was 0.082 km/sec. This figure includes the bad point at 64 sec period which our model was unable to fit. Typically, the angle between the event and the great circle path to ALPA was approximately  $7^{\circ}$ . This leads to a systematic error in phase velocity of  $-0.75\%$ .

#### Results of the Data Inversion Experiment

We inverted the dispersion data along with its estimated errors to obtain the theoretical dispersion curve indicated by the solid line in Figure 5. This was done with a generalized inverse program operating on the phase velocity partial derivatives (e.g., Wiggins, 1972; Rodi, et al., 1975). Our best fitting model, whose layer parameters are given in Table 2, was obtained by varying the P and S velocities of a Gutenberg continent (Dorman, et al., 1960) starting model. Several tries were made varying the crustal thickness in each case. The best fitting model in terms of rms error of fit and absence of oscillations between adjacent layer parameters had a 45 km thick crust.

Its rms error of fit to the mean data values was 0.045 km/sec. However, our data can also be fit by a model with a 40 km thick crust and a 3% reduction in the shear wave velocity of the first layer below the Moho. The rms error of this fit is slightly greater but still within the rms error of the data.

The best fitting model is shown plotted (on a logarithmic scale) in Figure 6. A comparison between the S velocity profiles of our model and the Gutenberg continent starting model is shown in Figure 7. Averaging, or resolution, kernels for the first four layer S velocities are shown in Figure 8. These are measures of the independence of the corresponding parameter. The first three S velocities are well-determined by this data set; however, the fourth and, as it turns out, succeeding S velocities are relatively poorly resolved. Our best fitting model, therefore, is principally a crust and uppermost mantle structure. Nevertheless, the data do not require an S wave low velocity zone in the upper mantle in order to provide a satisfactory fit for our preferred model.

#### Discussion

There is little information available in the literature on the crustal structure of Novaya Zemlya. Geologic maps (e.g., Yanshin, 1966) indicate that the island is a northern extension of the Ural mountain belt. However, whereas the Urals are a generally linear feature in the continental USSR, they are twisted in an S-shaped curve towards the edge of the continental shelf. On Novaya Zemlya rocks of the western Paleozoic miogeosyncline are exposed (Hamilton, 1970). Thus, we would infer the crustal structure of Novaya Zemlya to be a modified version of the Ural mountains structure.

Contour maps of crustal thickness for the USSR, reproduced as Figures 9 and 10, (Kosminskaya, et al., 1969; Volvovskii, 1973) clearly show the relation of Novaya Zemlya to the Ural mountain belt. However both indicate, from the plotted contours, that the crust in the southernmost island is between 35 and 40 km thick. The map by Kosminskaya et al. includes all of Novaya Zemlya between the 35 and 40 km thick contours. On the other hand, the map by Volvovskii, presumably the result of more analysis, places the 35 km contour near the fiord separating the southern island from the rest of Novaya Zemlya. However, the deep seismic sounding profiles indicated by Kosminskaya et al., which were used to produce these maps, are all well to the south of Novaya Zemlya. A crustal thickness of 50 km is indicated for the southern Urals, based on the work of Khalevin, et al. (1966). They also give the P velocities just above and just below the Moho as 6.4 and 8.2 km/sec respectively.

The Novaya Zemlya structural model we present here (Table 2) agrees in some respects with that derived by Khalevin, et al. (1966) for the southern Urals. In particular, our crustal thickness is 45 km compared to 50 km, our lower crust P velocity is 6.55 km/sec compared to 6.4 km/sec, and our Moho P velocity is 8.18 compared to 8.2 km/sec. Also, our third layer is 26 km thick while theirs is 32 km thick. Unfortunately there appear to be no pertinent S velocities available for comparison and, since our model is primarily an S wave structure, these would be desirable to have.

#### Conclusions

We have demonstrated a method for isolating the Rayleigh wave phase velocity dispersion of a source region from teleseismic Rayleigh

wave recordings and applied it to the southern island in Novaya Zemlya. The preferred crust and upper mantle structure we derived by inverting our phase velocity data is characterized by a 45 km thick crust and the absence of a shear wave low velocity zone in the upper mantle. Although little information is available in the literature concerning the crustal structure of Novaya Zemlya, our structure is compatible published P-wave structures for the southern Ural mountains. We conclude that this method is capable of providing reliable information about inaccessible source region structures.

#### References

1. Alexander, S. S., Unpublished Research Note, The Pennsylvania State University, University Park, PA, 1969.
2. Dorman, J., M. Ewing, and J. Oliver, Study of shear velocity distribution in the upper mantle by Rayleigh waves, Bull. Seismol. Soc. Am., 50, 87-115, 1960.
3. Glover, P. and S. S. Alexander, Lateral variations in crustal structure beneath the Montana LASA, J. Geophys. Res., 74, 505-431, 1969.
4. Hamilton, W., The Uralides and the motion of the Russian and Siberian platforms, Geol. Soc. Am. Bull., 81, 2553-2576, 1970.
5. Khalevin, N. I., V. S. Druzhinin, V. M. Rybalka, E. A. Nezoleno-va, and L. N. Chudakova, Results of deep seismic sounding of the earth's crust on the Middle Urals, Izv. Akad. Nauk. SSSR, Phys. Earth, 1966(4), 36-44, 1966.
6. Kosminskaya, I. P., N. A. Belyaevsky, and I. S. Volvovskii, "Explosion Seismology in the USSR," The Earth's Crust and Upper Mantle, Geophysical Monograph 13, AGU, Washington, D.C., 1969.
7. Rodi, W. L., P. Glover, T. M. C. Li, and S. S. Alexander, A fast, accurate method for computing group velocity partial derivatives for Rayleigh and Love modes, Bull. Seismol. Soc. Am., 65, 1105-1114, 1975.
8. Taylor, R. W., Relative event analysis with application to the mid-Atlantic ridge, Ph.D. Thesis, the Pennsylvania State University, University Park, PA, 1972.
9. Volvovskii, I. S., Seismic Investigations of The Earth's Crust in the USSR, Nauka, Moscow, 1973 (in Russian).

10. Wiggins, R., The general linear inverse problem: implications of surface waves and free oscillations on earth structure, Rev. Geophys. Space Phys., 10, 251-285, 1972.
11. Yanshin, A. L., Tectonic Map of Eurasia, Geological Institute of the Academy of Sciences, USSR, Moscow, 1966 (in Russian).

### Figure Captions

1. Geometry for the two event, single station method.  $D$  is the event separation.  $D_{\text{eff}}$  is the effective separation which is the projection of the event separation on the great circle path to the station.
2. Map showing the locations of the two test sites on Novaya Zemlya and their common propagation path to the Alaskan Long Period Array (ALPA).
3. Map of the southern part of Novaya Zemlya showing the PDE and re-located epicenters of the five events used in this investigation.
4. ALPA center sensor seismograms from the five events used in this investigation. All data are plotted to the same amplitude and time scales.
5. Rayleigh wave phase velocity dispersion data, estimated errors, and the computed dispersion from our Novaya Zemlya structural model.
6. Logarithmic scale plot of the layer parameters from our Novaya Zemlya structural model. First layer parameters are outside the range of the plot.
7. Logarithmic scale plot of the shear velocity from our Novaya Zemlya structural model compared to that from the starting Gutenberg continent model. First layer parameters are outside the range of the plot.
8. Shear velocity averaging kernels for the first four layer shear velocities as functions of the shear and compressional wave velocities in the model.
9. Moho depth contour map of the USSR. Taken from Kosminskaya, et

al., 1969.

10. Moho depth contour map of the USSR. Taken from Volvovskii, 1973.

TABLE 1  
PDE Epicenters

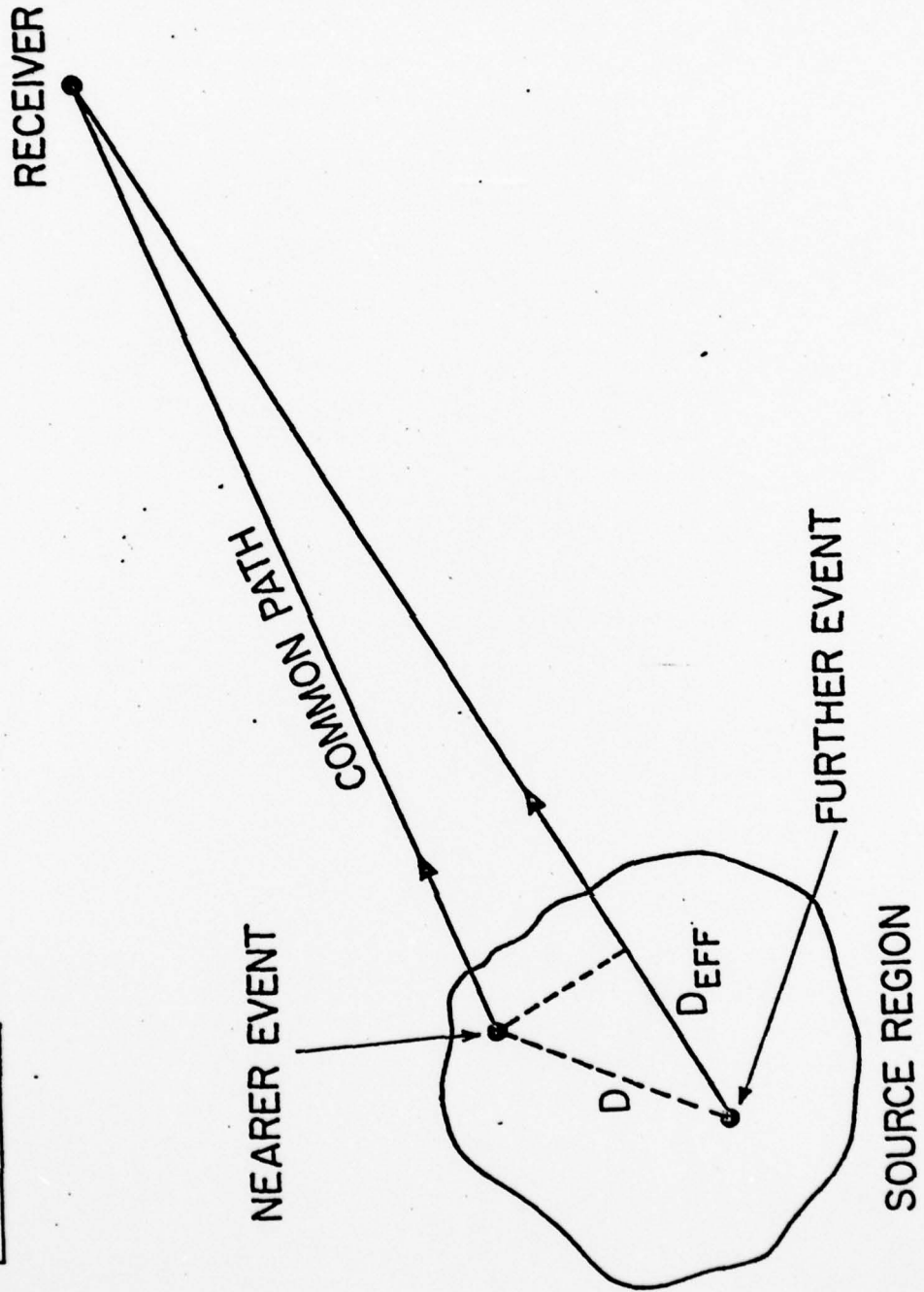
Event	Origin Time	Latitude	Longitude	$m_b$
8/28/72	05 59 56.5	73.34	55.09	6.3
11/2/74	04 59 56.7	70.82	54.06	6.7
8/23/75	08 59 57.9	73.37	54.64	6.4
10/18/75	08 59 56.3	70.84	53.69	6.7
10/21/75	11 59 57.3	73.35	55.08	6.5

TABLE 2

## Novaya Zemlya Structural Model Layer Parameters

Layer	Thickness (km)	P Velocity (km/sec)	S Velocity (km/sec)	Density (km/sec)
1	9	6.01	2.83	2.74
2	10	6.13	3.16	2.74
3	26	6.55	3.98	3.00
4	32	8.18	4.36	3.33
5	30	8.07	4.45	3.37
6	75	7.90	4.44	3.42
7	75	8.10	4.45	3.48
8	100	8.50	4.60	3.55
9	100	9.00	4.95	3.65
10	∞	9.75	5.37	3.95

Figure 1.



18-2-13815

Figure 2.

18-2-13816



Figure 3.

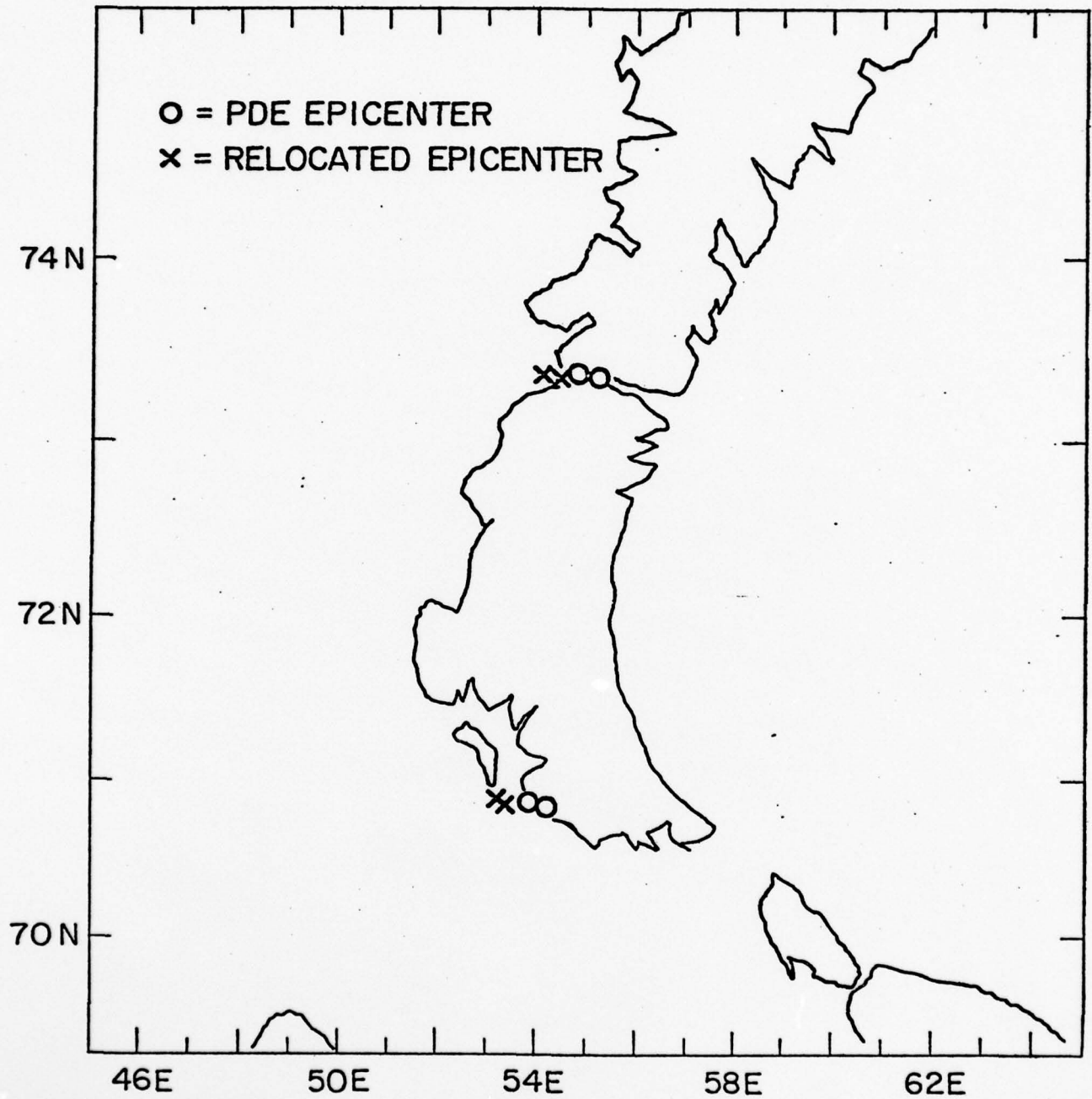


Figure 4.

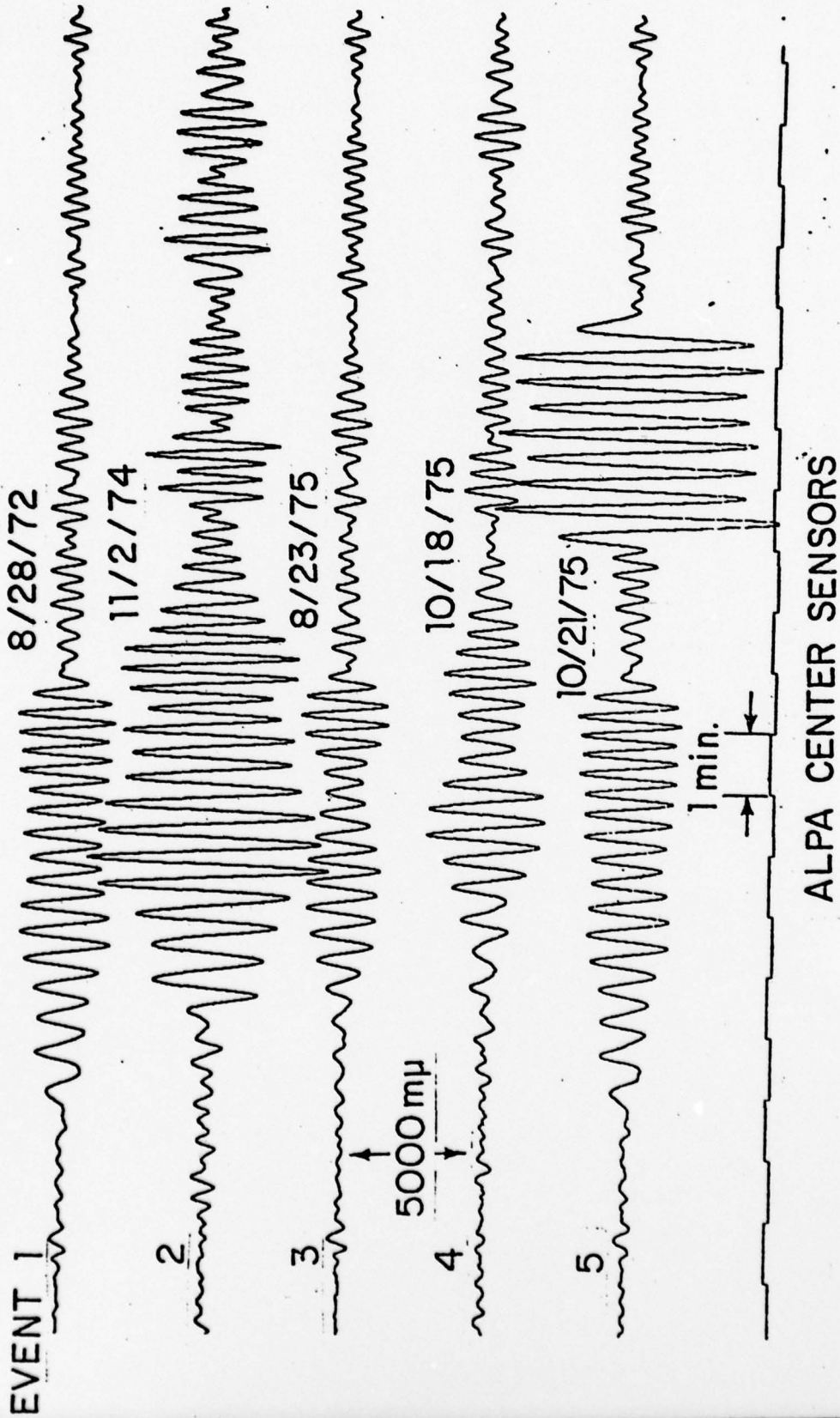


Figure 5.

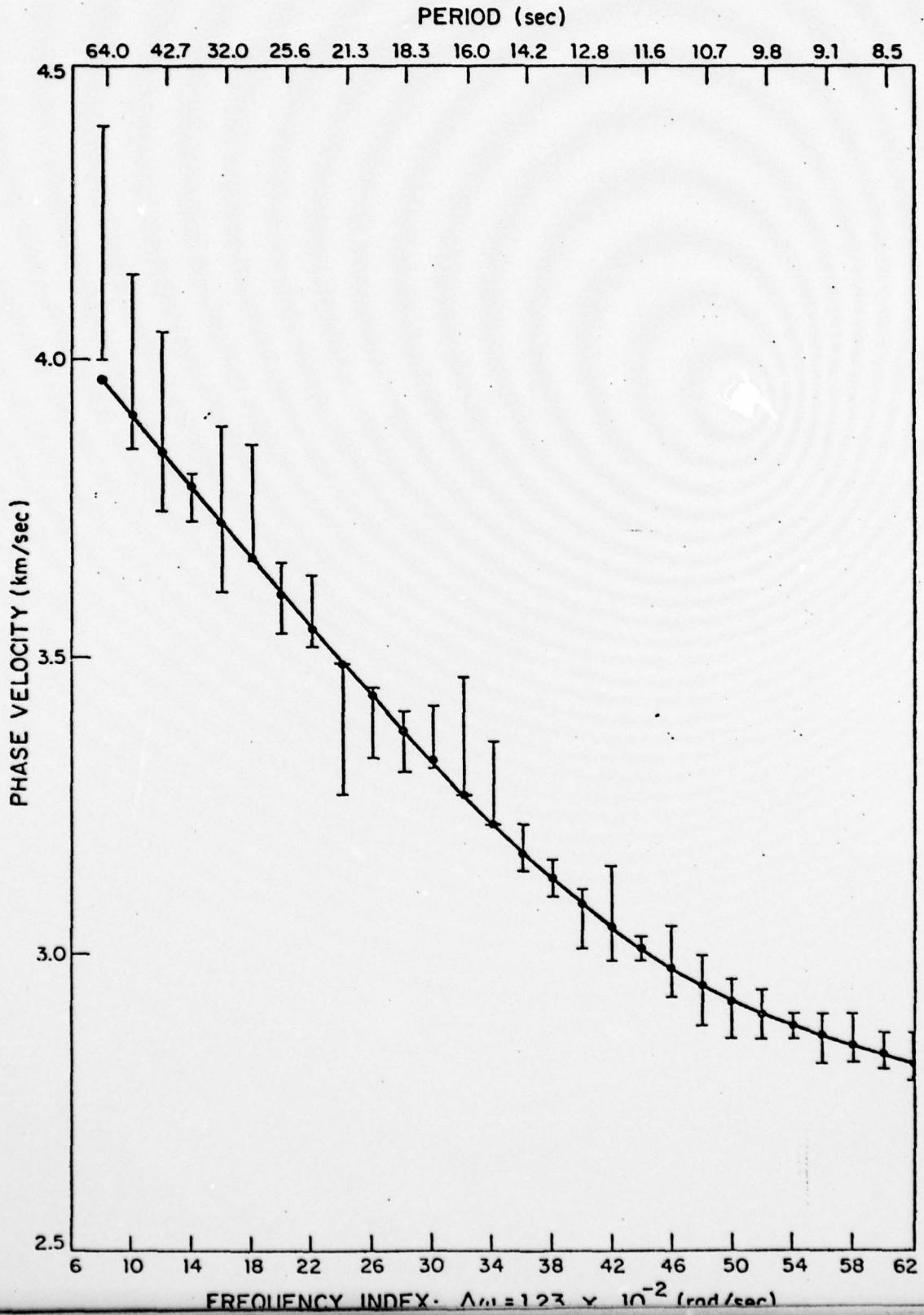


Figure 6.

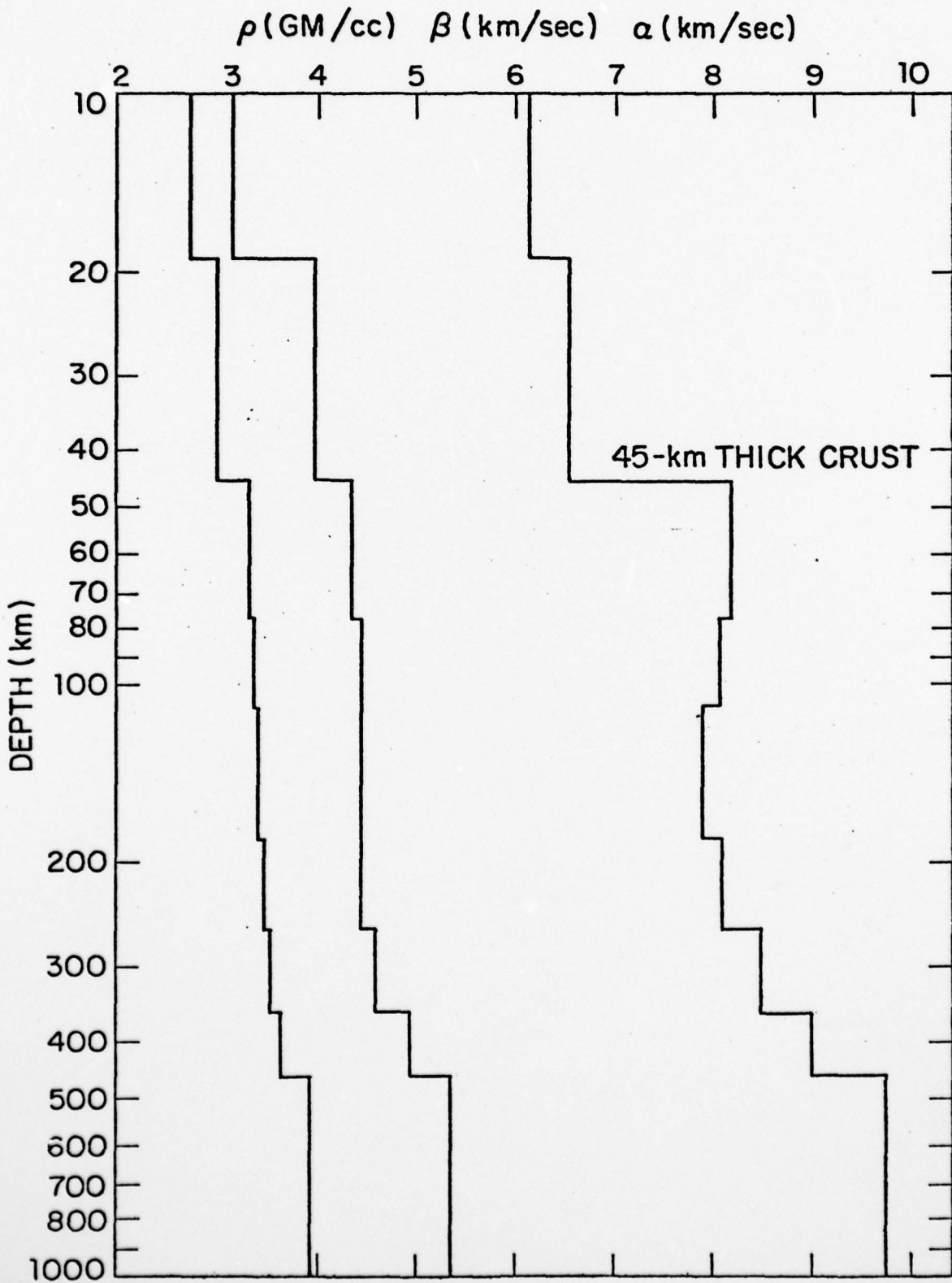


Figure 7.

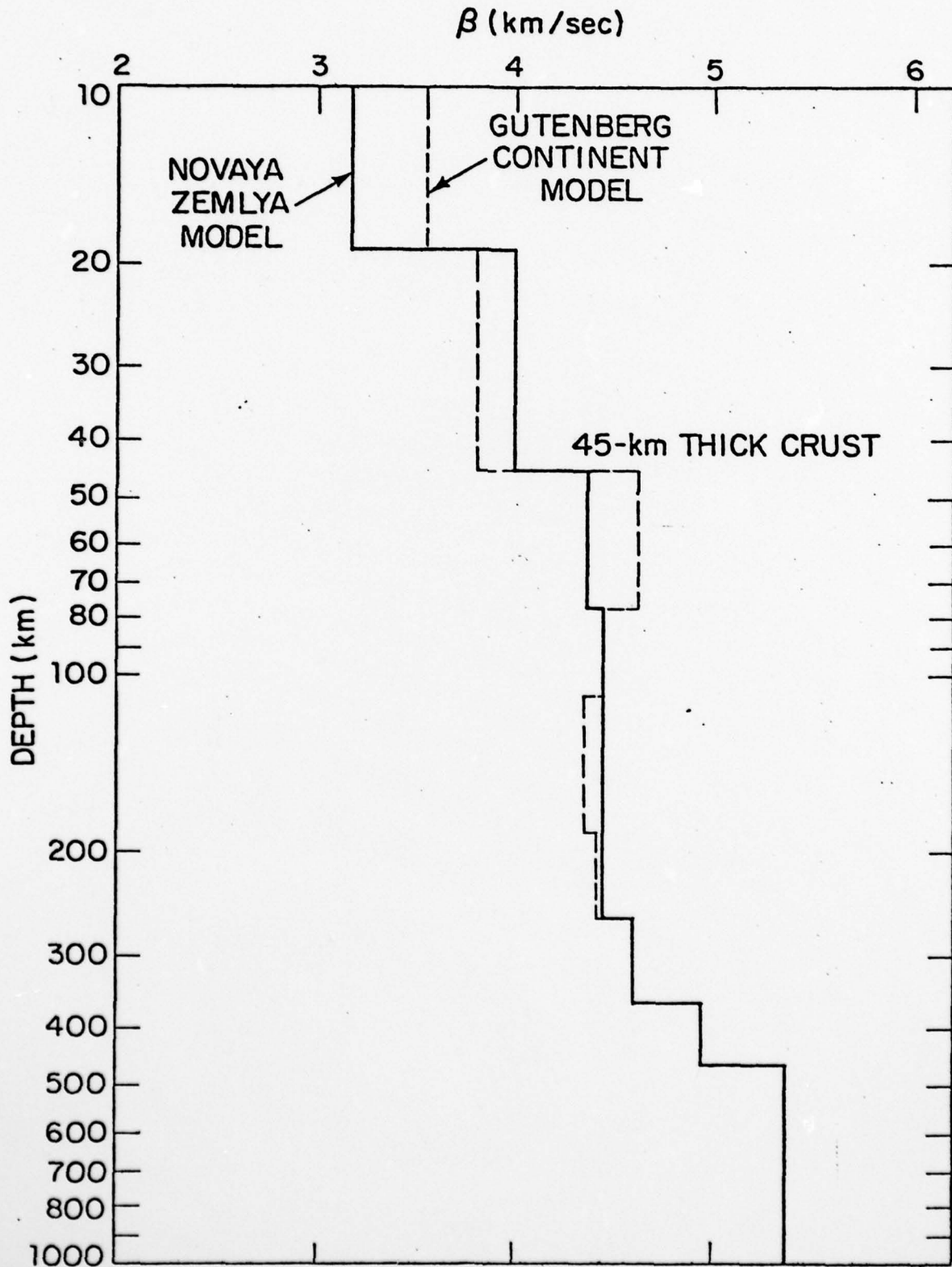


Figure 8.

18-2-13820

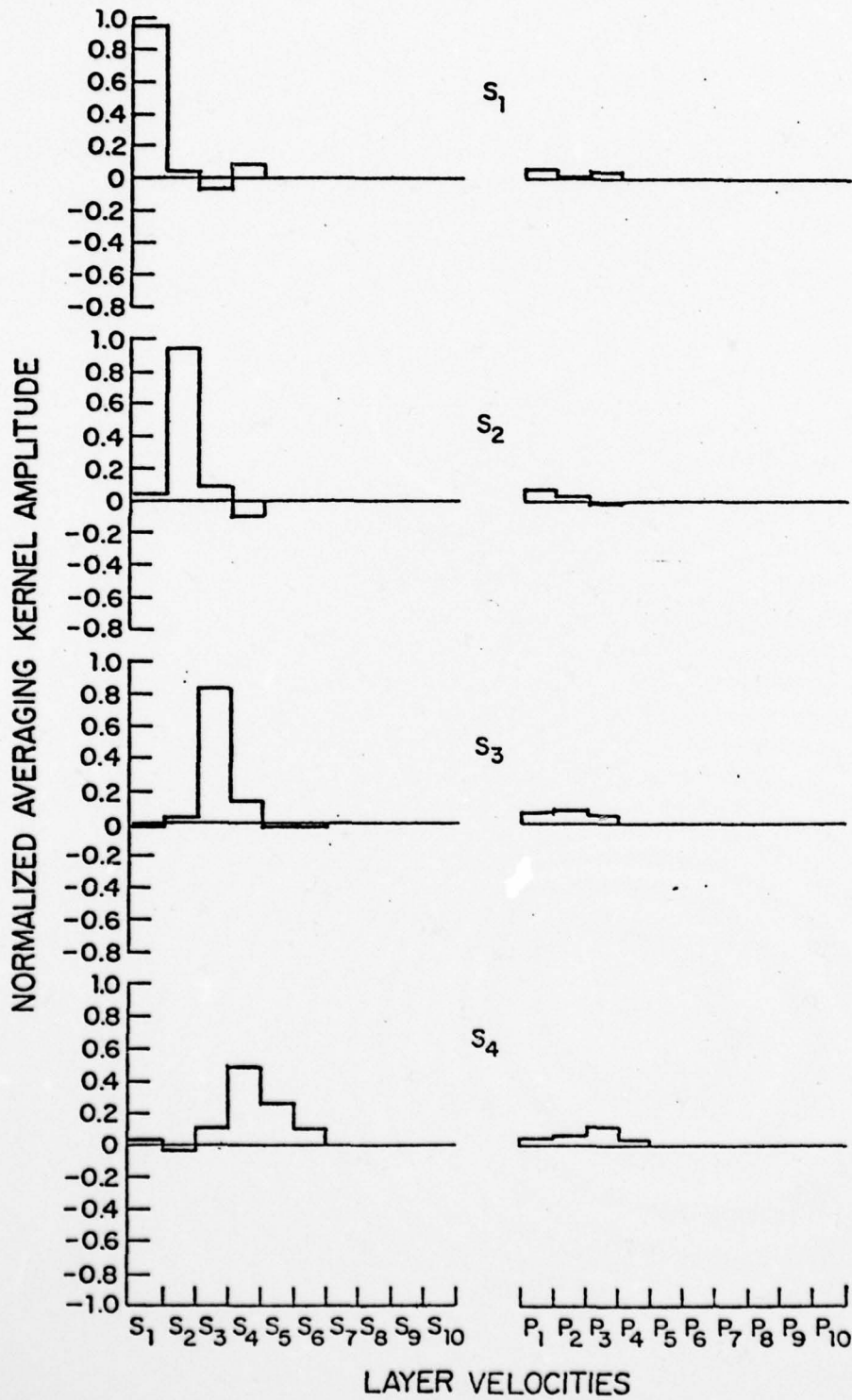


Figure 9.

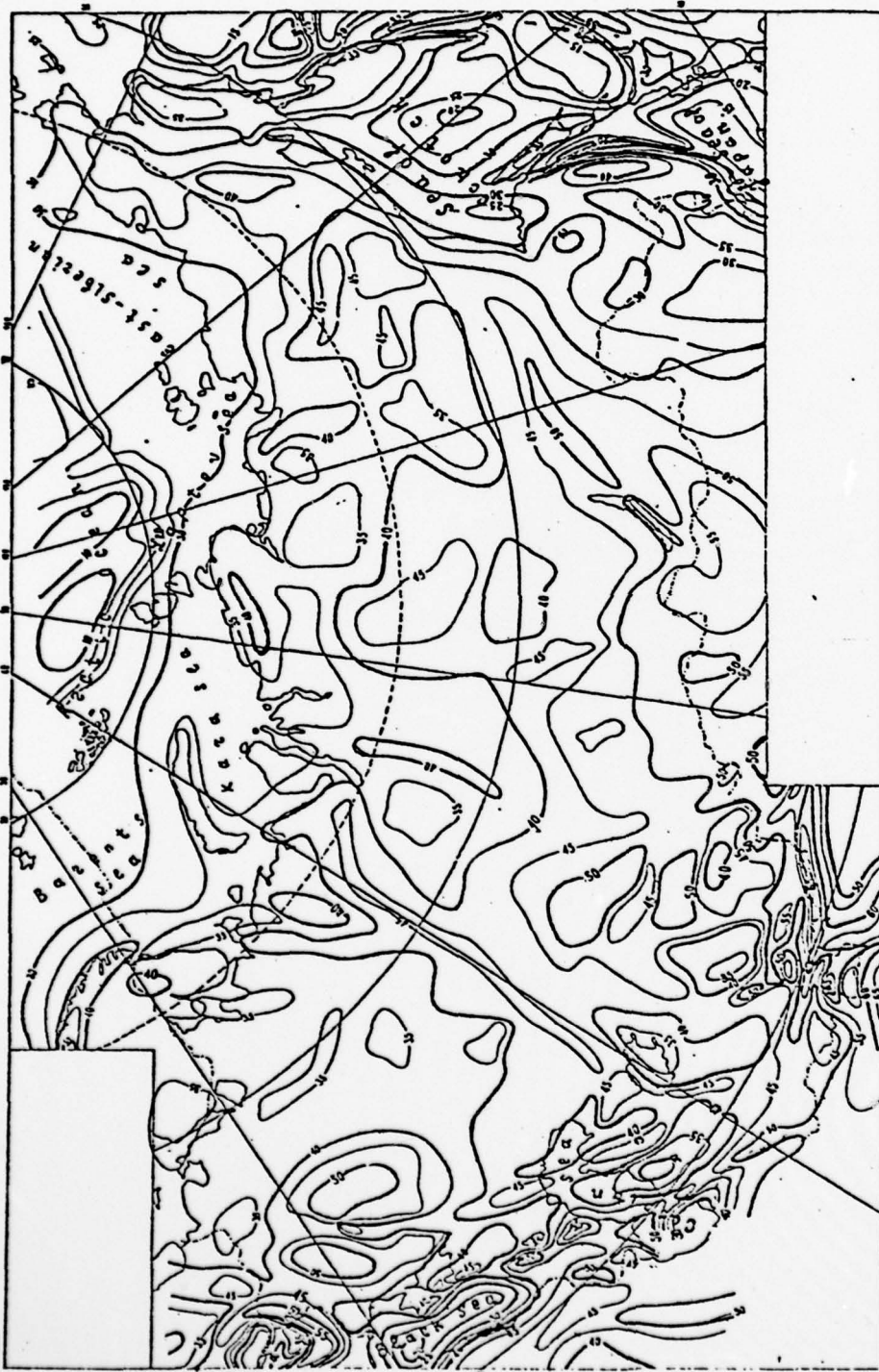


Fig. 11. Relief map of the M boundary for the USSR and adjacent territory. Numbers are depth below sea level in kilometers (see Figure 4, p. 318).

Kosminskaya, I. P., N. A. Belyaevsky, and I. S. Volvovskii,  
Explosion seismology in the USSR, in The Earth's Crust  
and Upper Mantle, AGU, Washington, 1969.

Figure 10.



Рис. 84. Схема рельефа поверхности Мохоровичича территории СССР и сопредельных стран. Составил И. А. Боллепский, А. А. Борисов, И. С. Волынецкий, 1970 год.

1 — изолинии поверхности Мохоровичича (в км); 2 — отметки глубин до поверхности Мохоровичича в отдельных точках по сейсмологическим данным (в км от уровня моря).

Volvovskii, I. S., Seismic Investigations of the Earth's Crust  
in the USSR, Moscow, 1973.

APPENDIX F

## A static and dynamic finite element analysis of the 1971 San Fernando, California, earthquake

D. W. McCowan\* *Applied Seismology Group, Lincoln Laboratory,  
Massachusetts Institute of Technology, Lexington, Massachusetts 02173, USA*

P. Glover and S. S. Alexander *Geophysics Section, Department of  
Geosciences, Pennsylvania State University, University Park, Pennsylvania 16802, USA*

Received 1976 August 5; in original form 1976 February 22

**Summary.** A two-dimensional finite element model was developed for the source region of the San Fernando earthquake. Stochastic inversion of the surface displacement data of Alewine was carried out to obtain estimates of the displacements and stress drops along the actual fault surface in the finite element model. We calculate an average slip of 222 cm with a rms fit to the data of 8 cm. The average computed stress drop was 290 bar, with a maximum of 650 bar. Using these calculated stresses in a dynamic model of the earthquake, we compute theoretical accelerograms for the Pacoima Dam site. For frequencies less than 2 Hz, we found that the observed accelerograms were fitted best by a model with a propagating source having a rupture velocity of approximately  $2.5 \text{ km s}^{-1}$ . These results suggest that the dynamic finite element method can be used to estimate strong earthquake ground motion from extended sources (earthquakes) in many different complex geologic structures.

### Introduction

The San Fernando, California earthquake of 1971 February 9 provided seismologists with a large quantity of unusually accurate near-field observational data. Despite the numerous investigations to date, there remains considerable controversy about its fault mechanism particularly the rupture history and the identification of individual seismic phases in the accelerograms. The present study is not intended to settle the controversy. Rather, we demonstrate how a two-step procedure: (i) an inversion calculation based on a static two-dimensional finite element method (FEM) with a simple mesh configuration and faulting model and, (ii) a dynamic finite element (DFEM) calculation with the same model, can be used to predict ground motion for extended earthquake sources such as the San Fernando event. In constructing best-fitting models, both static and dynamic, for the San Fernando earthquake, considerable insight is gained as to the nature of the faulting process and the interpretation of the energy arrivals recorded by the Pacoima Dam accelerograms.

\* Formerly at: Geophysics Section, Department of Geosciences, Pennsylvania State University, University Park, Pennsylvania 16802, USA.

### Choice of FEM mesh and fault model

Studies of the fault-plane solutions for the main San Fernando event and the aftershock sequence (Allen *et al.* 1971; Wesson, Lee and Gibbs 1971; Wyss & Hanks 1972; Whitcomb *et al.* 1973; Hanks 1974) indicate that faulting took place on a three-dimensional curved surface dipping  $20\text{--}25^\circ$  near the Earth's surface and increasing to  $50\text{--}55^\circ$  with depth. The hypocentre is placed at depths of 8–13 km by these authors. The maximum width of the initial fault, estimated from the spatial distribution of the aftershock sequence, is 15 km. The fault plane solutions such as Whitcomb (1971) obtained (strike  $N64^\circ W$ , dip  $52^\circ NE$ , rake  $64^\circ$ ) and the observed ground displacements both indicate that the fault mechanism was predominantly thrusting in a south-west direction.

In order to make our finite element experiment computationally feasible, it is necessary to develop a two-dimensional model of this fault and its surrounding geologic structure. Jungels & Frazier (1973) have shown that a test of the applicability of two-dimensional (plane strain) analysis is the ratio of the fault length to fault width of the actual earthquake being modelled. For models where this ratio is greater than unity, they found that plane strain analysis is accurate to within a few per cent. If we construct a model with a focal depth for the initial point of rupture at 9.5 km, with a fault plane dipping at  $45^\circ$ , we get 13.4 km for the fault length and the aspect ratio is approximately one. This, of course, is only a geometric criterion as to the appropriateness of the plane strain approximation. However, the fact that the fault mechanism indicates a predominance of thrust faulting suggests that by considering a profile perpendicular to the strike of the faulting, we may ignore edge effects.

To construct our finite element model, we consider the geologic structure along the profile A–B in Fig. 1. In the region of the San Fernando fault, the profile which passes through the epicentre and the Pacoima Dam, corresponds to the BB' profile of Jungels & Frazier (1973) as well as the profile used by Alewine & Jordan (1973).

Fig. 2 shows the actual finite element mesh superimposed on the geologic profiles. The elastic properties of the six rock types were obtained from well-drilling data published by Duke *et al.* (1971). The large elements are placed around the periphery of the mesh to eliminate reflections in the dynamic calculations given below. No attempt was made, therefore, to include mantle structure in the mesh.

The fault model, which is similar to that used by Espinoza, Harding & Lopez-Arroyo (1973), allows the fault surfaces to move along planes at  $45^\circ$  to the Earth's surface. Furthermore, only the San Fernando fault is allowed to move; i.e. the San Gabriel fault remains locked. Fig. 3 is a schematic diagram of the kinematics of this fault model. In the figure, the direction of motion of the two fault surfaces is indicated by the unit vectors  $n_1$  and  $n_r$ .

Obviously this is not a very complicated fault model. It consists of only a single unburied fault whose plane of motion is 'locked' into the mesh, i.e. not permitted to warp or translate relative to the coordinate system. The stresses necessary to deform the mesh into its final configuration are taken to be the negative of the tectonic stresses which were released by the earthquake. For the model, the stresses are applied to produce the deformation. But, for the earthquake, the excess tectonic stresses are balanced by equal and opposite frictional stresses along the fault until they are removed by the physical fault mechanism which produced the earthquake. Thus, although stress in our model is applied rather than released, the values are equivalent. Historically, this description of the faulting process is due to Reid (republished 1969) and is known as the elastic rebound theory. With the advent of the 'new global tectonics', it is the generally accepted (simplified) description of the mechanism of earthquakes (Brune 1974).



**SAN FERNANDO EARTHQUAKE PROBLEM  
WITH BOTTOM PINNED**

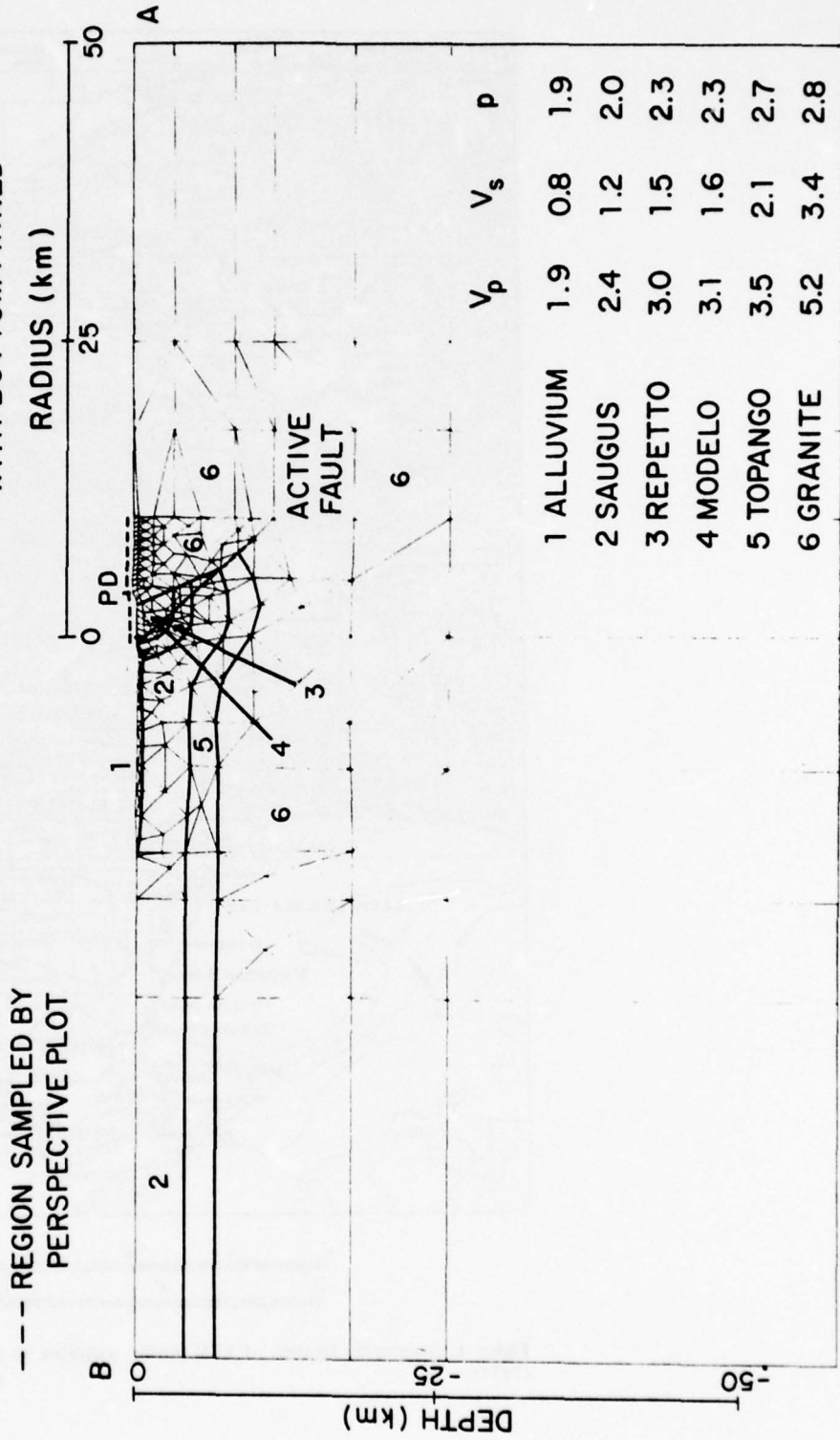


Figure 2. Finite element mesh superimposed on geologic profile shown in Fig. 1. Location of the Pacoima Dam is indicated by the letters PD, and the extent of the profile shown in the perspective plot is indicated by dashes.

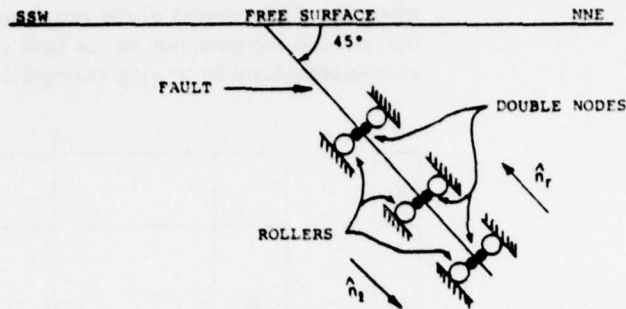


Figure 3. Schematic diagram of the fault model showing double row of nodes which are constrained to move parallel to the fault.

**Static finite element analysis**

Taken together, the mesh and fault model provide the basis of a straightforward static FEM problem in the form of

$$Kx = f \tag{1}$$

where  $K$  represents the stiffness matrix for the mesh, which is itself composed of individual element stiffnesses computed from the static properties of each element material (e.g. see Zienkiewicz 1971; McCowan 1975 for computational details),  $x$  is the vector of node point displacements, and  $f$  is the node point force vector (the unknown in our problem) which generates the displacements. Formally we may rewrite (1) as

$$K^{-1} f = x \tag{2}$$

and ask: given a set of known displacements  $x_s$  what are the corresponding forces  $f$ ? For this static problem, the appropriate rhs vector is a profile of surface displacements. Applying this approach to the San Fernando earthquake, we used the vertical surface displacements reported by Alewine (1974) which were obtained from levelling and gravity surveys.

To set up a canonical inverse problem, equation (1) must first be manipulated in order to separate the known from unknown quantities. This can be done through partitioning. By identifying the vertical surface and fault displacements in the node displacement vector  $x$  and the fault forces in the force vector  $f$ , the system can be written:

$$\begin{array}{c}
 K \\
 \boxed{\phantom{K}}
 \end{array}
 \begin{array}{c}
 x \\
 \begin{array}{c}
 x_f \\
 x_s \\
 x_R
 \end{array}
 \end{array}
 =
 \begin{array}{c}
 f \\
 \begin{array}{c}
 f_f \\
 0 \\
 0
 \end{array}
 \end{array}
 \tag{3}$$

where the displacements of the remaining nodes in the mesh are in  $x_R$  and the forces on all the nodes in the mesh not on the fault surface are zero. This problem can be formulated as an inverse problem by 'solving' the equations to give

$$\begin{array}{c} x \\ x_f \\ x_s \\ x_R \end{array} = \begin{array}{c} K^{-1} \\ B \\ \end{array} \begin{array}{c} f \\ f_f \\ 0 \\ 0 \end{array} \quad (4)$$

where the inverse stiffness matrix (sometimes called the compliance matrix) has been partitioned in the same way as the vectors. The vertical surface displacements of the problem are therefore related to the generating force system acting on the fault nodes by

$$Bf_f = x_s. \quad (5)$$

The  $B$  matrix is the FEM Green's function for the earthquake, i.e. it is the set of vertical displacement profiles for a set of unit forces on the fault nodes.

Equation (5) now has the three key elements of a linear inverse experiment. It has a 'theory', expressed in terms of the matrix  $B$ , which is to be used in explaining the data. It has a 'model' in terms of the fault force vector  $f_f$  which constitutes the set of unknowns in the experiment, i.e. the set of actual values of the parameters needed to complete the theory. Thirdly, it produces a trial 'data' vector  $x_s$  for each model by the indicated matrix multiplication which can be compared with the actual data vector to judge the accuracy of the 'fit'. Expressed in this form, the experiment can be inverted by standard optimization methods to yield a description of the fault behaviour. Because the problem is overdetermined (47 data points are to be explained by 25 unknowns), the weighted least-squares (WLS) procedure is the obvious first approach. It has the advantage that additional information is introduced into the estimate by including the relative errors of observation in the data. A summary of this method is presented in the Appendix.

Fig. 4 shows the vertical displacements of the free surface calculated along the profile. Also shown in Fig. 4 are the observed data points which are represented by circles. The lines in the circles are the estimated observational errors. This solution fits the observed data with an rms error of 2.5 cm. Fig. 5 shows the corresponding slip along the fault as a function of depth. It is obvious that, although the rms error of the overall fit is small, the calculated slip on the fault, with maximum values of 210 m, is quite unrealistic. These slips correspond to calculated stress drops of the order of tens of kilobars which are not plausible in a shallow earthquake.

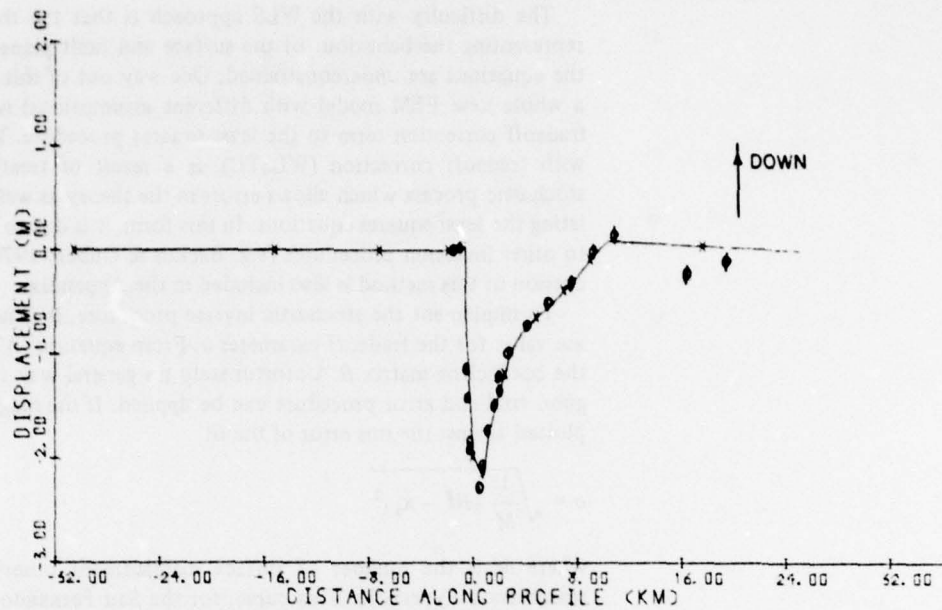


Figure 4. Static vertical displacement of the free surface. Displacements calculated from the FEM model using WLS approach are indicated by the solid line, the circles represent the observed data from Alewine (1974), the vertical bars indicate the uncertainty in the latter.

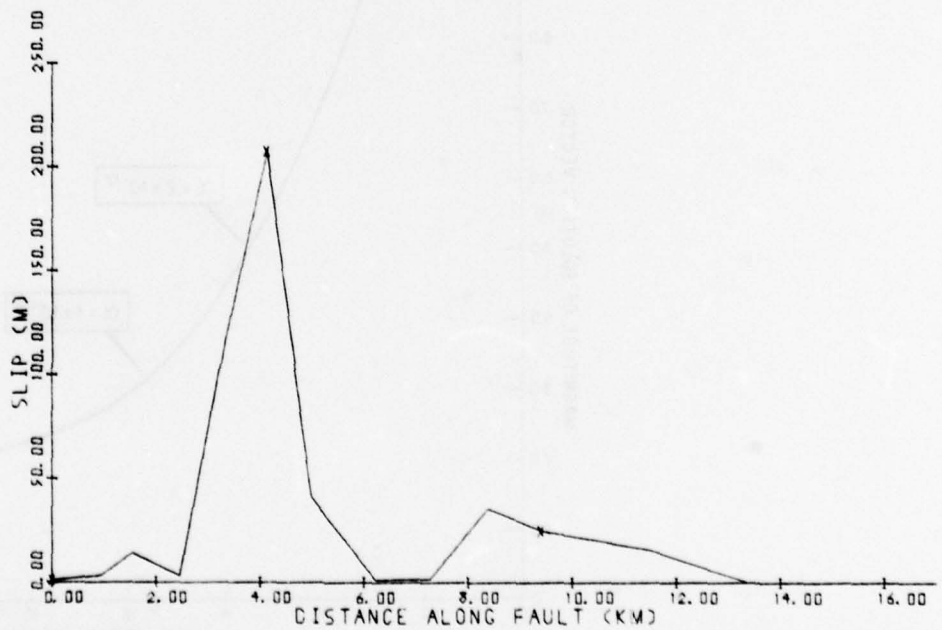


Figure 5. Relative displacement along the fault surface calculated from the FEM model using WLS approach.

The difficulty with the WLS approach is that the theory is not capable of accurately representing the behaviour of the surface and fault plane at the same time. In other words, the equations are underconstrained. One way out of this difficulty (aside from constructing a whole new FEM model with different assumptions) is to relax the 'theory' by adding a tradeoff correction term to the least-squares procedure. The method, weighted least-squares with tradeoff correction (WLSTC), is a result of treating the inversion procedure as a stochastic process which allows errors in the theory as well as errors in the data when formulating the least-squares equations. In this form, it is due to Foster (1961) but it is also related to other inversion procedures (e.g. Backus & Gilbert 1970; Jordan & Franklin 1971). A discussion of this method is also included in the Appendix.

To implement the stochastic inverse procedure, it is necessary to determine an appropriate value for the tradeoff parameter  $\alpha$ . From equation (A7), it is apparent that  $\alpha$  depends on the coefficient matrix  $B$ . Unfortunately no general way to set  $\alpha$  seems to work, but a very good trial and error procedure can be applied. If the magnitude of the estimate vector  $|f|$  is plotted against the rms error of the fit

$$\sigma = \sqrt{\frac{1}{M} |Bf - x_s|^2}$$

where  $M$  is the number of surface displacement observations  $x_s$ , a curve results which resembles a hyperbola. This curve, for the San Fernando earthquake problem, is shown in Fig. 6. As Gilbert (1970) noted: 'the place to be is down at the corner' (of the tradeoff curve). Thus the 'optimum' value of  $\alpha$  in this case,  $\alpha = 1 \times 10^{-16}$ , produces an estimate of  $f$  which, in terms of slope, is halfway between the two extremes of the curve.

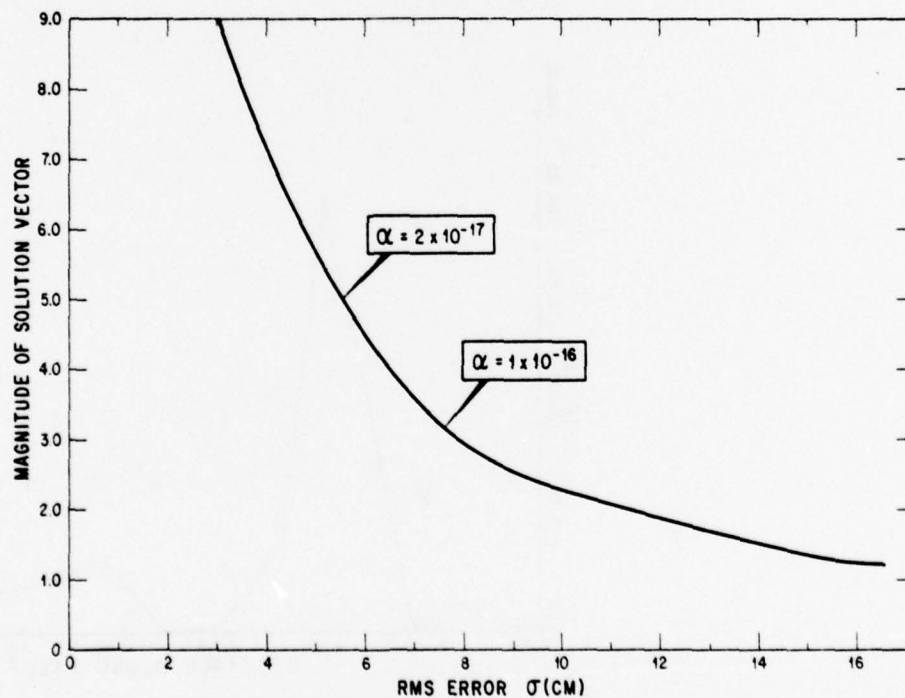


Figure 6. Trade-off parameter curve. The value of the tradeoff parameter  $\alpha = 1 \times 10^{-16}$  is optimum.

The results of using the WLSTC procedure for this optimum value of the trade-off parameter  $\alpha$  are shown in Figs 7-10. Fig. 7 shows the calculated and observed vertical surface displacements. The rms error in fitting the observed data is now 8.0 cm. The most visible effect of using the optimum tradeoff correction is not forcing the model to fit the two data points approximately 9 km north-east of the surface faulting. The corresponding horizontal

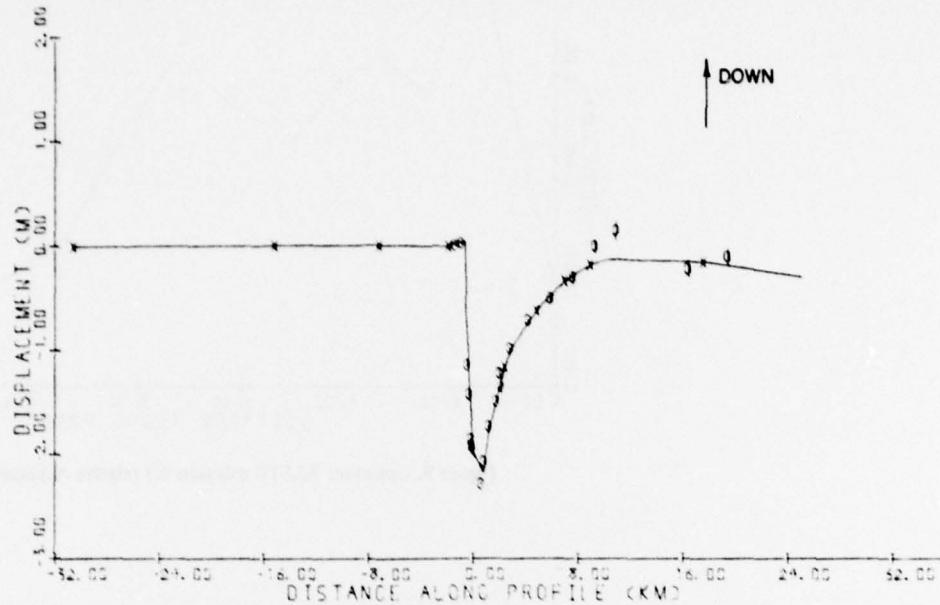


Figure 7. Static vertical displacements of free surface calculated using optimum value of  $\alpha$  in the WLSTC procedure.

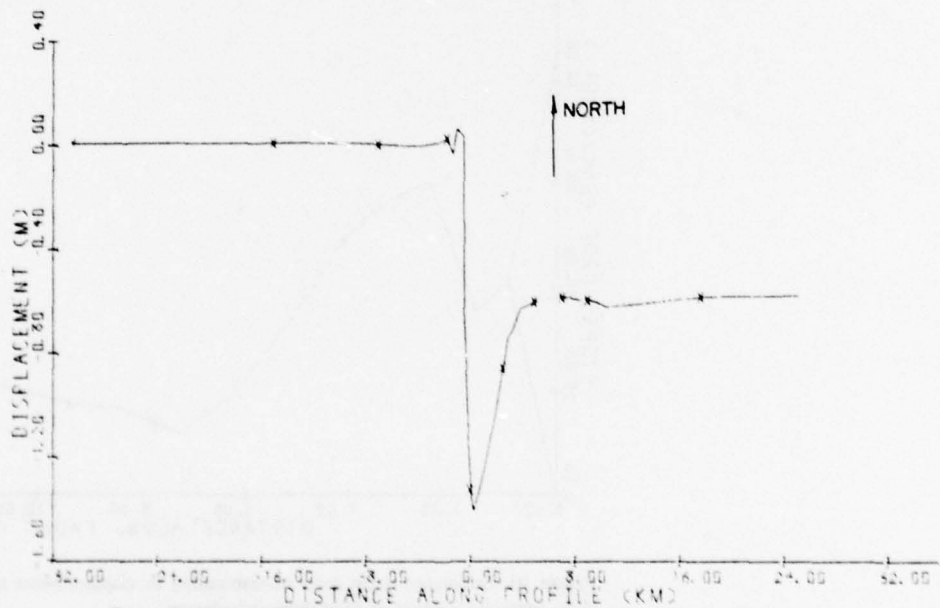


Figure 8. Horizontal displacements of free surface corresponding to those in Fig. 7.

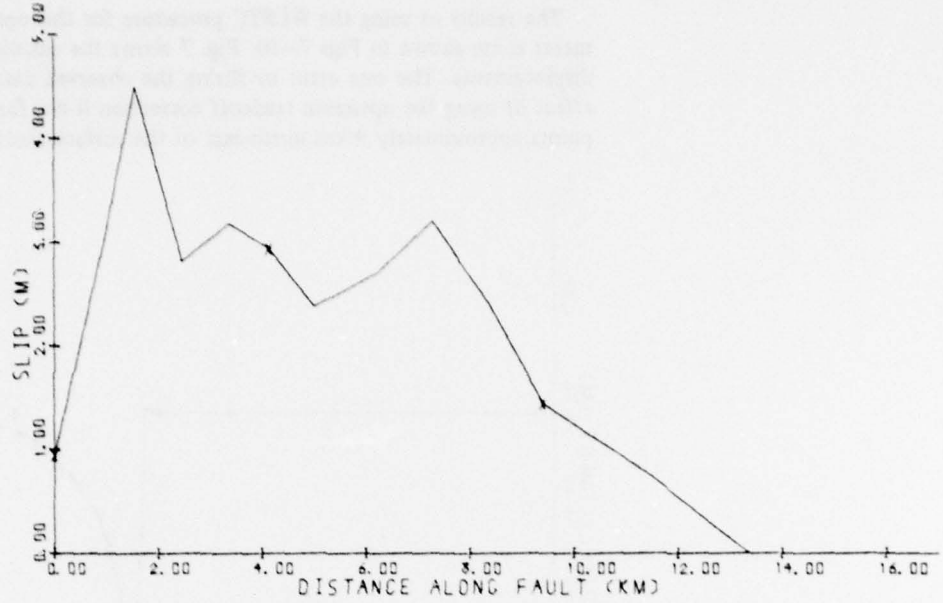


Figure 9. Optimum WLSTC solution for relative displacements along fault surface.

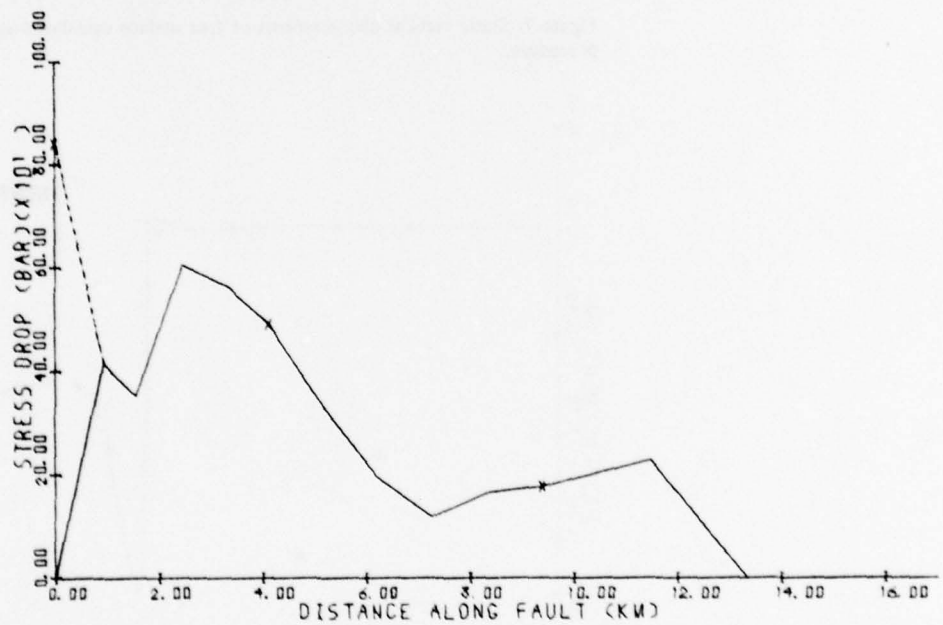


Figure 10. Calculated stress drop corresponding to displacements shown in Fig. 9. The dashed line indicates anomalous region of FEM stress calculation.

surface displacements are shown in Fig. 8. Here the use of the tradeoff parameter results in a displacement profile closely resembling that of an ideal thrust fault. The calculated displacements along the fault surface are shown in Fig. 9. The maximum slip is now 4.5 m at a point 1.56 km down the fault, with a second local maximum of 3.7 m located at 7.23 km down the fault. The maximum computed stress drop (Fig. 10) is 650 bar, at a point 2.4 km from the free surface. The average stress drop is 290 bar. (The apparent peak in the stress drop at the surface, indicated by the dashed part of the curve in Fig. 10, should be disregarded as it is an artefact of the way stress is computed from the spatial derivatives of the displacement solution.)

As a check, we recomputed an inverse solution using a tradeoff parameter equal to one-fifth of the optimum value. The rms fit of this solution was 5.7 cm. The fault slip and stress drop which resulted from the non-optimum tradeoff-corrected model follow the overall behaviour of the corresponding optimum solutions. Thus, over the range shown in these examples, the principal results of the WLSTC models are relatively insensitive to a change in the tradeoff parameter of a factor of 5 in the vicinity of the 'optimum' value.

#### Dynamic finite element analysis

If the mesh does not change with time, then the dynamical problem mesh can be developed from the static case by simply assigning mass and damping to each element. These quantities, however, must be distributed throughout each element in a manner consistent with the stiffness distribution (McCowan 1975). The resulting set of equations is

$$M\ddot{\mathbf{a}} + D\dot{\mathbf{v}} + K\mathbf{x} = \mathbf{f}$$

where  $M$  and  $D$  are the mass and damping matrices and  $\mathbf{a}$  and  $\mathbf{v}$  are the node point acceleration and velocity vectors, respectively. To complete the definition of the problem, relations linking acceleration and velocity to displacement must be supplied. A common set of such relations are the finite difference equations due to Newmark (1959)

$$\mathbf{v}_{n+1} = \mathbf{v}_n + \frac{h}{2} (\mathbf{a}_n + \mathbf{a}_{n+1})$$

$$\mathbf{x}_{n+1} = \mathbf{x}_n + \mathbf{v}_n h + \left(\frac{1}{2} - \beta\right) h^2 \mathbf{a}_n + \beta h^2 \mathbf{a}_{n+1}$$

where  $\beta$  is the integration parameter, and  $h$  the integration time step. With these equations  $\mathbf{a}$ ,  $\mathbf{v}$ , and  $\mathbf{x}$  at time  $n+1$  can be computed from their values at time  $n$ . Throughout, a value  $\beta = 0.25$  was used as this leads to an unconditionally stable integration scheme (McCowan 1975). The integration time step  $h$  was chosen so as not to exceed the Courant limit given by

$$h < \frac{d}{\alpha}$$

where  $\alpha$  is  $P$ -wave velocity, and  $d$  is the smallest mesh spacing. A damping matrix appropriate to this integration scheme and suitable for use in problems concerned with Rayleigh waves (Frazier *et al.* 1973; McCowan 1975) is

$$D = \frac{h}{2} K.$$

In this form, the damping matrix attenuates waves proportional to their frequency squared and its effects are most pronounced in coarse regions of the mesh. Since the large elements

in Fig. 2 are placed around the periphery of the mesh to prevent reflections from the boundaries occurring during the time window of interest, the effect of damping is minimal in the region of the Pacoima Dam.

The optimum fault force model derived from the static calculation above provides important constraints on the dynamics of the San Fernando earthquake. Specifically, it limits the number of possible dynamic fault models by setting the asymptotic behaviour of the faulting process. That is, the force time history acting on each fault node must approach the calculated static value for large times. The time history itself is therefore an unknown in the dynamic inversion experiment. Unfortunately, the number of possible time histories is too large to be economically inverted by formal methods so the problem was parameterized by assuming various functional forms for the stress time history and comparing the observed and calculated accelerograms.

The simplest earthquake stress time history is a propagating step function of applied stress. Following Hanks (1974), the initial rupture is placed in the hypocentral region and is assumed to propagate along the fault towards the surface. As the rupture reaches each fault node, the applied force goes to the static or asymptotic value instantaneously. Symbolically, this source-time function is

$$f(s, t) = f_{\infty}(s) H(t - s/V_R)$$

where  $s$  is the distance along the fault from the hypocentre,  $f_{\infty}$  is the static force,  $H$  is the unit Heaviside step function, and  $V_R$  is the rupture velocity. In this idealized earthquake mechanism model, the only undetermined parameter is the rupture velocity.

The results of trying two rupture velocities, 2.0 and 2.5 km s<sup>-1</sup> are presented in Figs 11–17. Fig. 11 is a pair of perspective plots of the horizontal and vertical components of surface displacement along the profile indicated by dashes in Fig. 2 for the 2.5 km s<sup>-1</sup> rupture velocity. The corresponding plots for the 2.0-km s<sup>-1</sup> case (not shown) are similar. It appears that most of the energy intersects the surface as a vertically travelling wave because the apparent velocity of the principal disturbance on the surface (> 10 km s<sup>-1</sup>) is higher than the  $P$ -wave velocity in any element of the mesh. There is no evidence of significant energy propagating along the Earth's surface from the fault break towards the Pacoima Dam. The perspective plots also show that the surface motion has a local maximum near Pacoima Dam. Ground motion on either side of this peak is about a third smaller than at the Pacoima Dam node.

Fig. 12 is a schematic diagram of possible energy paths from the hypocentre to the Pacoima Dam. The travel times  $t_1$  and  $t_2$  are for the direct  $P$  and  $S$  waves. Times  $t_3$  and  $t_4$  include the time of the rupture propagating up the fault and the time of seismic energy to propagate from the fault to the Pacoima Dam. For the  $t_3$  path, the seismic energy is assumed to propagate as a shear wave from the point on the fault nearest the Pacoima Dam. The  $t_4$  path is the time of a Rayleigh wave to reach the receiver from the fault after the rupture has broken the surface. These times are indicated on the figures which follow showing the calculated ground motion at the Pacoima Dam location.

The principal results of the dynamic experiment are shown in Figs 13–16. Both components of acceleration, velocity, and displacement are plotted for each of the two rupture velocities. The major arrival for both cases occurs around  $t_3$ . The direct  $P$  and  $S$  body-wave phases are smaller than the  $t_3$  arrival by an order of magnitude in both cases. Furthermore, the result noticed on the perspective plots is confirmed: there are no large amplitude phases at or later than  $t_3$ . The particle motion of the  $t_3$  part of the time history is up and south for both rupture velocities, i.e. parallel to that of the hanging wall side of the fault. This is consistent with the arrival being due to a shear wave propagating up and north in a direction

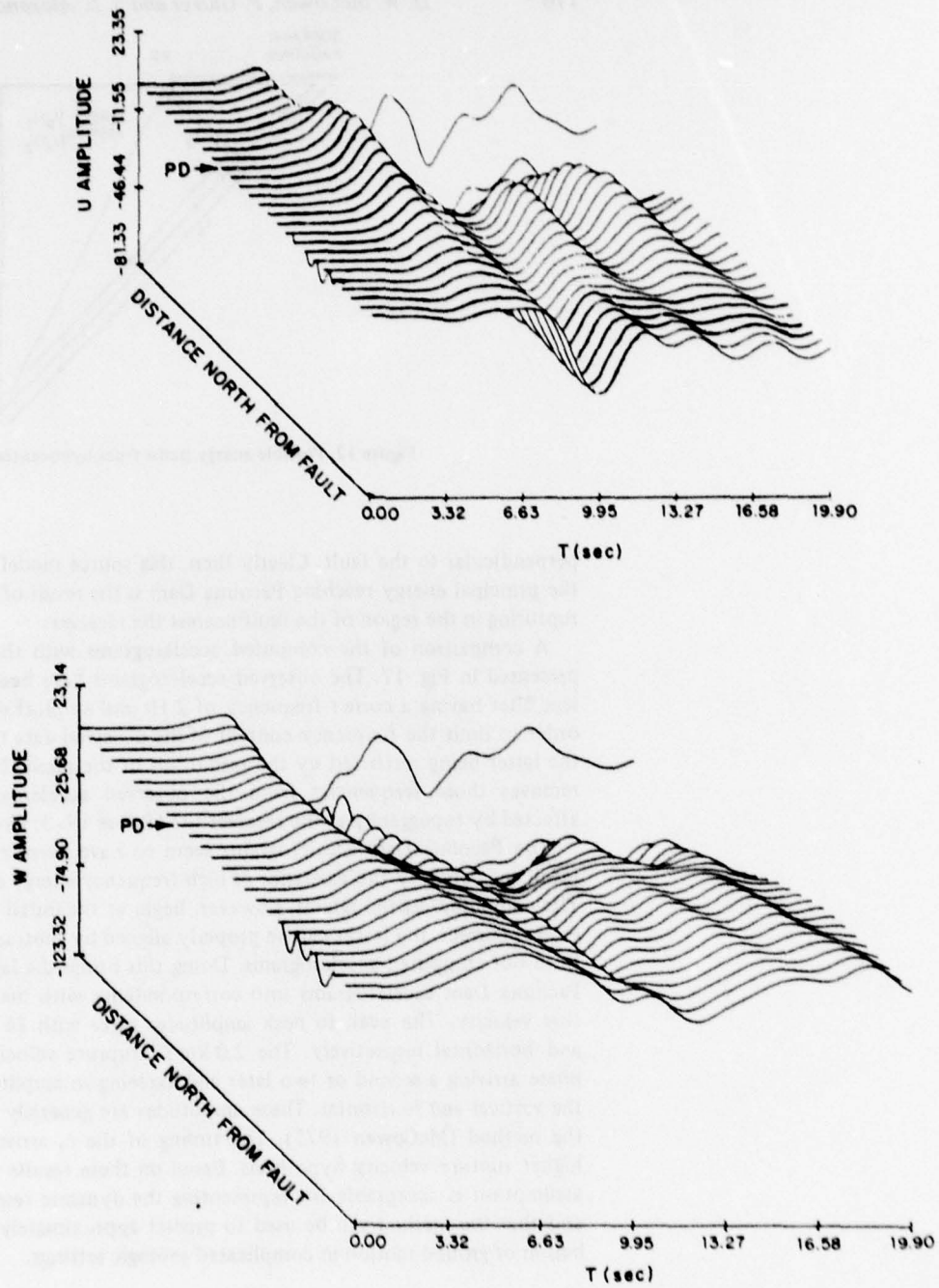


Figure 11. Calculated dynamic ground displacements at the free surface plotted as a function of distance north from the fault, for a rupture velocity of  $2.5 \text{ km s}^{-1}$ . PD indicates location of Pacoima Dam. Positive  $U$  and  $W$  amplitudes indicate displacement northward and upwards, respectively.

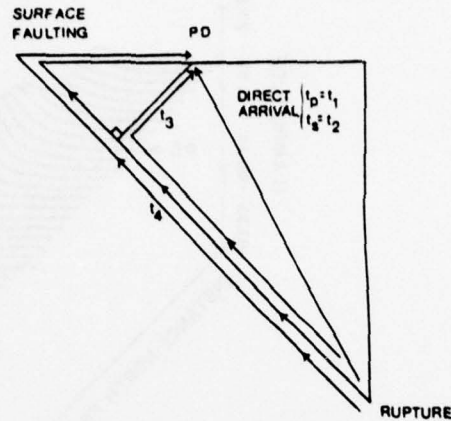


Figure 12. Possible energy paths from hypocentre to Pacoima Dam.

perpendicular to the fault. Clearly then, this source model favours the  $t_3$  arrival hypothesis: the principal energy reaching Pacoima Dam is the result of the shear waves generated by the rupturing in the region of the fault nearest the receiver.

A comparison of the computed accelerograms with those observed at Pacoima Dam is presented in Fig. 17. The observed accelerograms have been low-pass filtered with a phaseless filter having a corner frequency of 2 Hz and a rolloff of 12 dB/octave. This was done in order to limit the frequency content of the observed data to that of the DFEM calculations, the latter being restricted by the resolution of the mesh. In addition, the low-pass filtering removes those frequencies from the observed accelerograms most likely to have been affected by topography at the receiver site (Boore 1973; Wong & Jennings 1975).

The Pacoima Dam accelerograms seem to have been triggered by the direct  $P$  arrival, a result indicated by the existence of high frequency energy early in the record (Hanks 1974). The computed accelerograms, however, begin at the initial rupture time. So, if Hanks' inference is correct, the traces can be properly aligned by subtracting the  $P$  travel time (about 2 s) from our computed accelerograms. Doing this brings the large arrival occurring at 5 s on the Pacoima Dam accelerograms into correspondence with the  $t_3$  phase for the  $2.5 \text{ km s}^{-1}$  rupture velocity. The peak to peak amplitudes agree with 18 and 40 per cent for the vertical and horizontal respectively. The  $2.0 \text{ km s}^{-1}$  rupture velocity case is characterized by a  $t_3$  phase arriving a second or two later and agreeing in amplitude within 33 and 8 per cent for the vertical and horizontal. These amplitudes are generally within the accuracy expected of the method (McCowan 1975). The timing of the  $t_3$  arrival, though, tends to support the higher rupture velocity hypothesis. Based on these results we can infer that the stress step assumption is acceptable for representing the dynamic response at frequencies below 2 Hz and that the method can be used to predict approximately the spatial and temporal distribution of ground motion in complicated geologic settings.

### Discussion

It is instructive to compare our static FEM results with those obtained by previous investigators. Several authors examined the San Fernando earthquake problems by inverting analytic or piecewise-analytic solutions. All employed three-dimensional fault models in

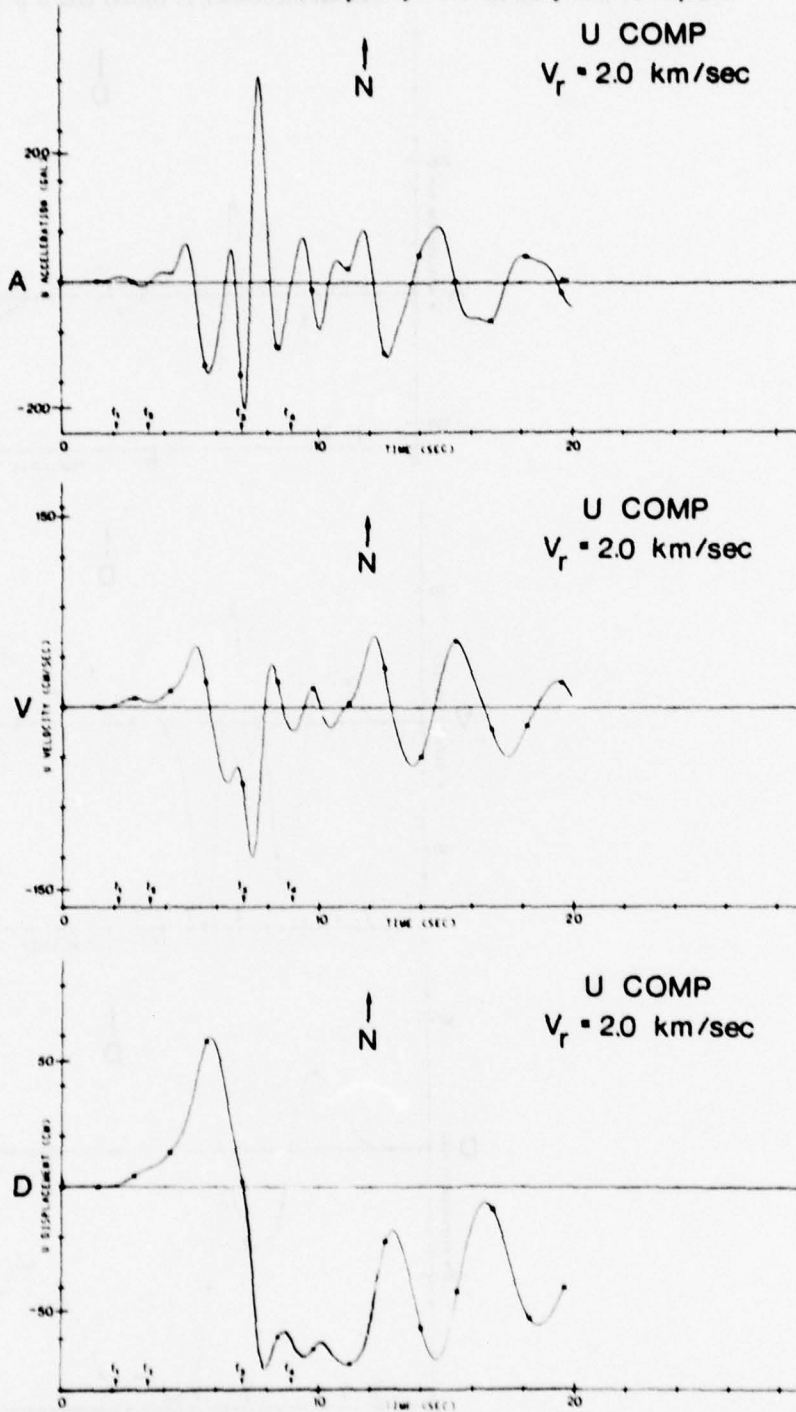


Figure 13. Computed horizontal component acceleration (A), velocity (V), and displacement time histories at the Pacoima Dam assuming a rupture velocity of  $2.0 \text{ km/s}$ . The arrival times indicated correspond to paths shown in Fig. 12. Arrow indicates motion towards north.

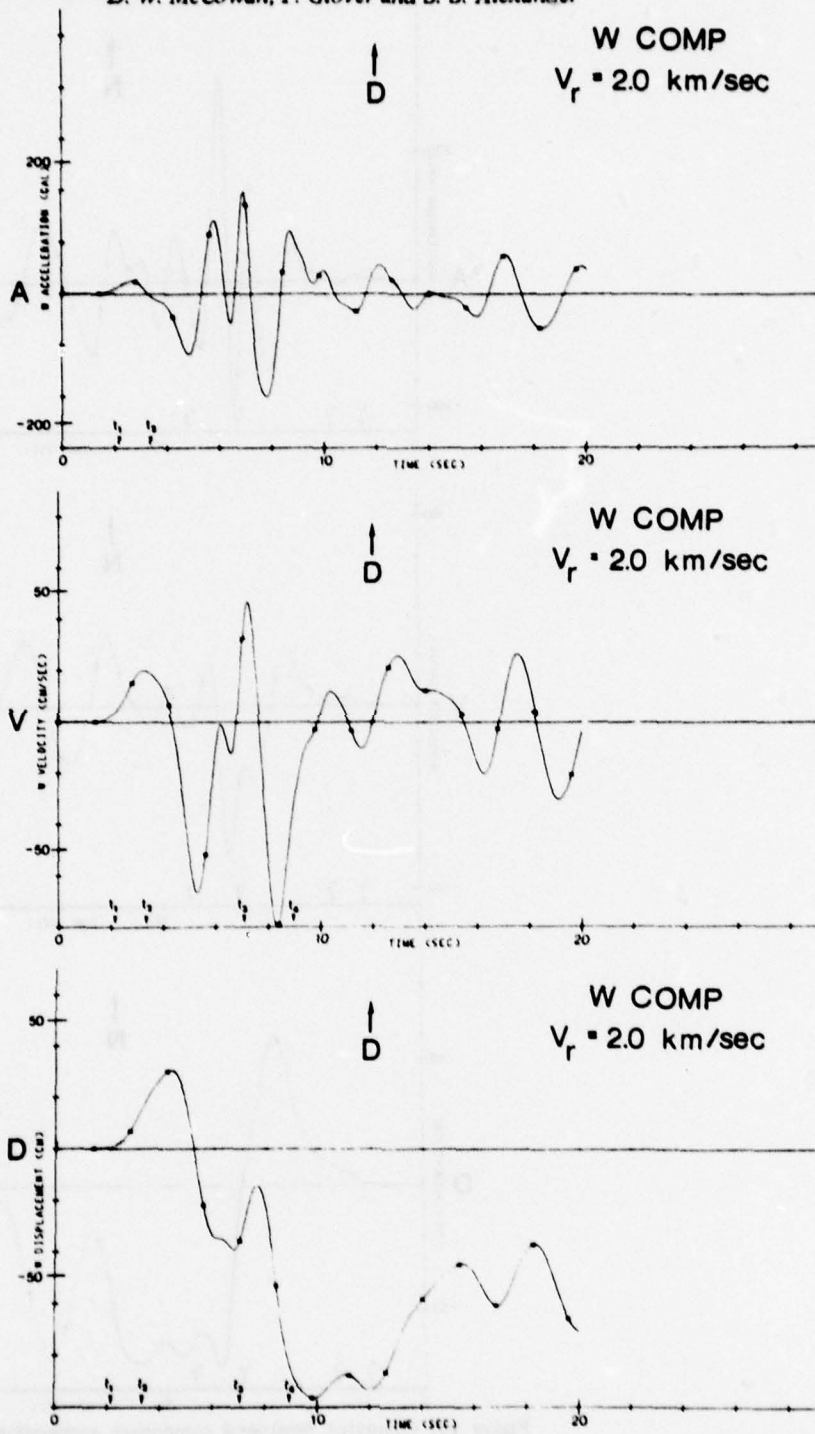


Figure 14. Computed vertical components corresponding to those of Fig. 13. Arrow indicates motion into the ground.

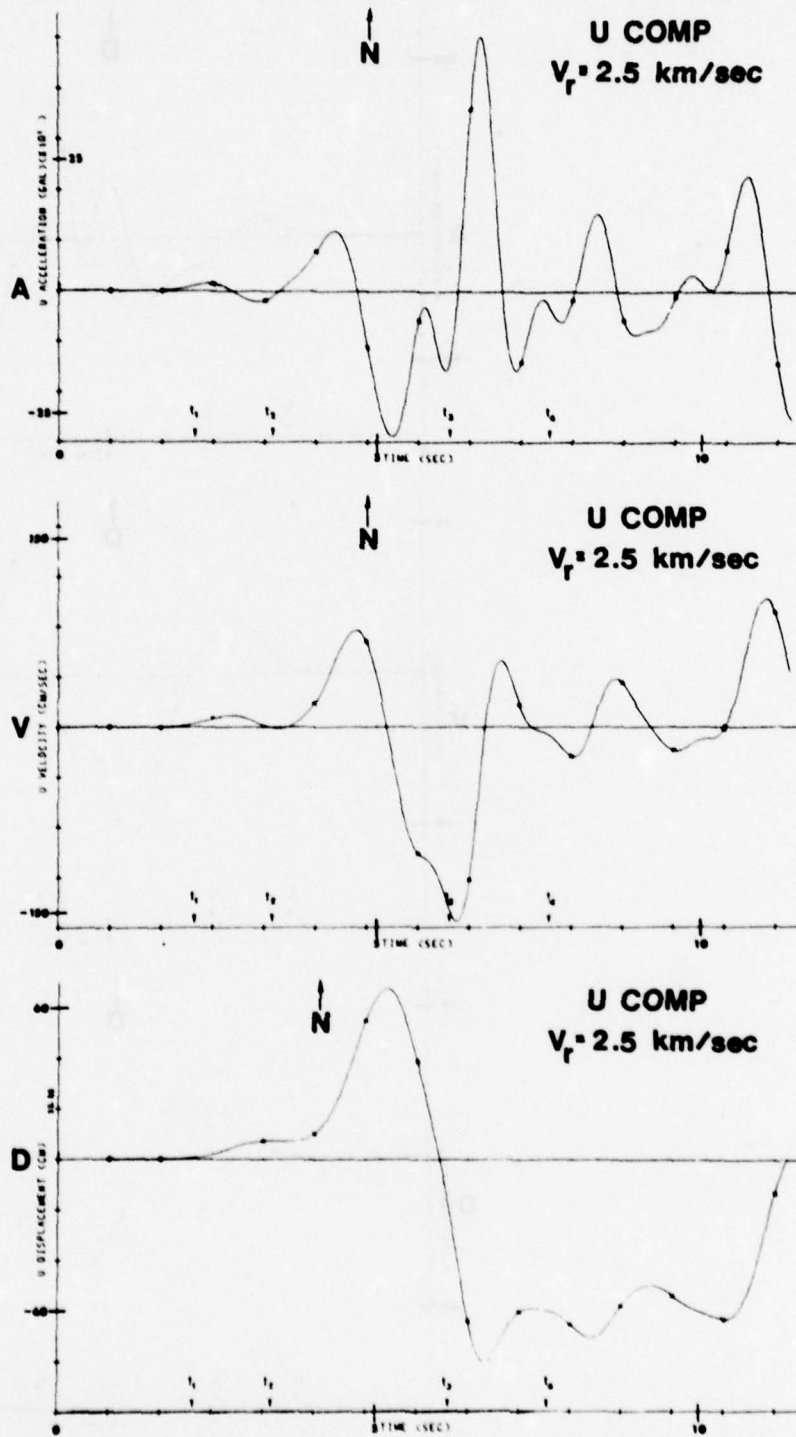
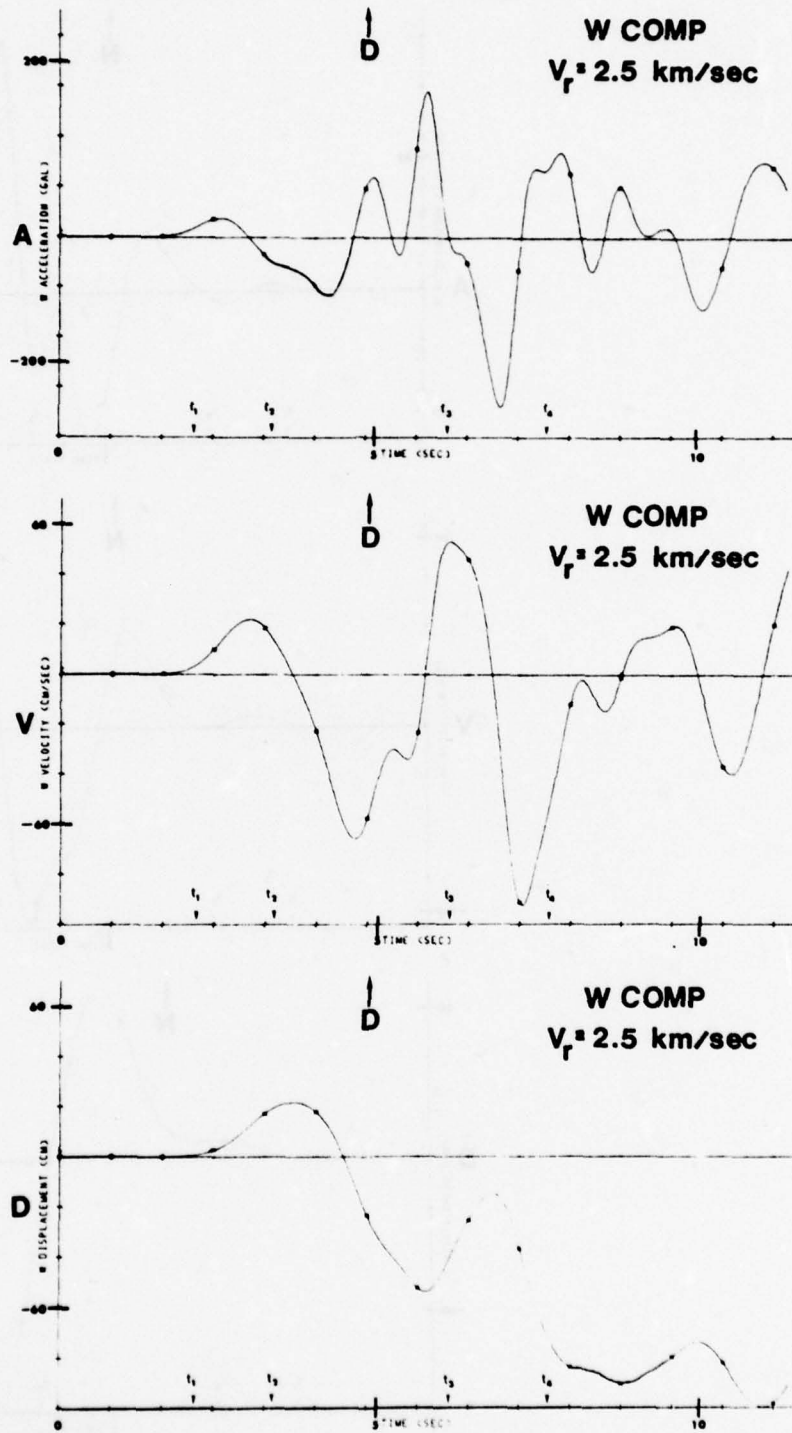


Figure 15. Same as Fig. 13 but for a rupture velocity of  $2.5 \text{ km s}^{-1}$ .

Figure 16. Same as Fig. 14 but for a rupture velocity of  $2.5 \text{ km s}^{-1}$ .

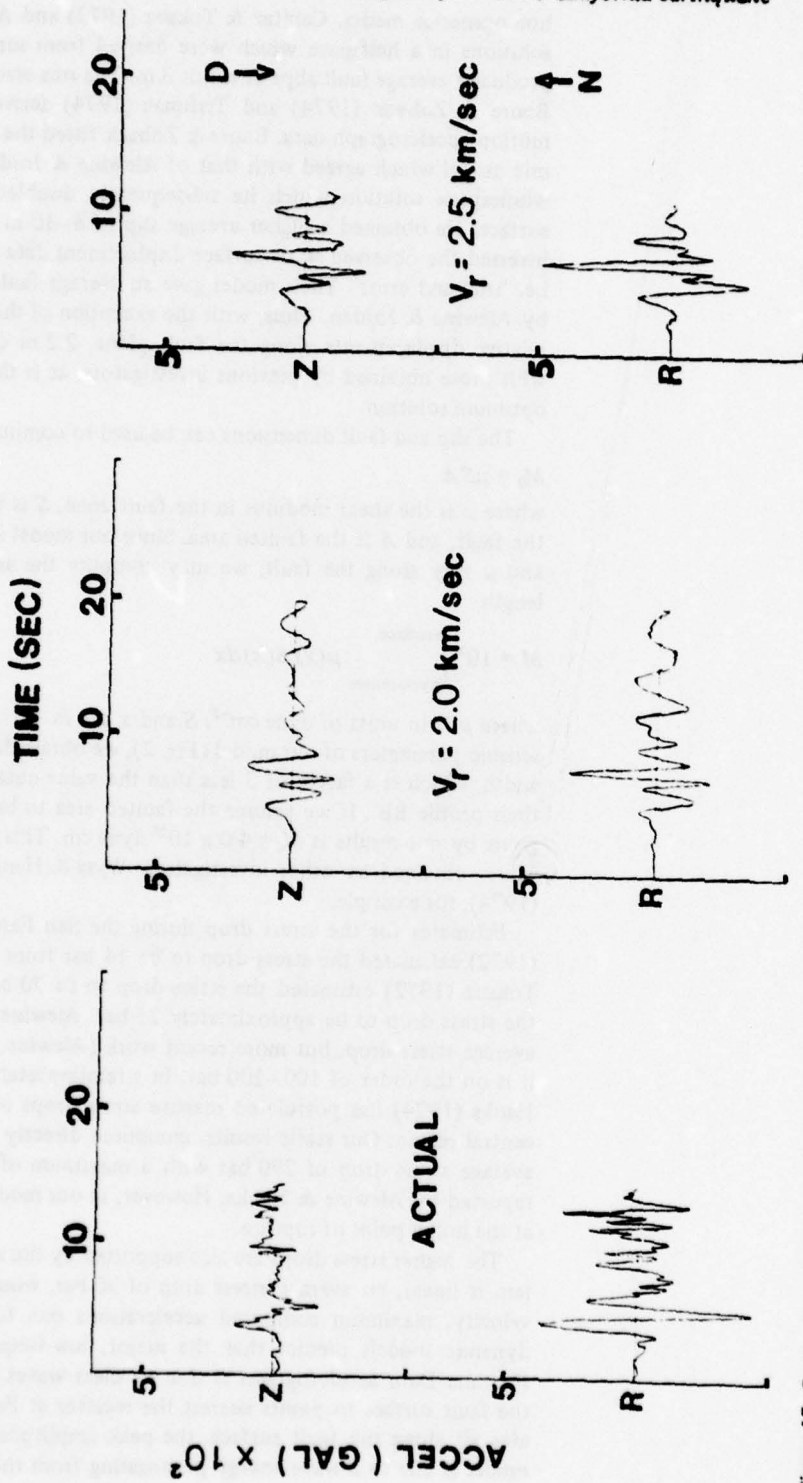


Figure 17. Comparison of the vertical (Z) and radial (R) components of the actual recorded accelerograms with those computed using rupture velocities of 2.0 and 2.5 km s<sup>-1</sup>.

homogeneous media. Canitez & Toksoz (1972) and Alewine & Jordan (1973) found static solutions in a halfspace which were derived from surface displacement data. Both models produced average fault slips of about 3 m. The rms error of Alewine & Jordan's fit was 6 cm. Boore & Zoback (1974) and Trifunac (1974) derived dynamic models from the strong-motion accelerograph data. Boore & Zoback fitted the peak velocity in the data with a dynamic model which agreed with that of Alewine & Jordan in the static limit. Trifunac used a wholespace solution which he subsequently doubled to simulate the effect of the free surface. He obtained a higher average slip of 8–10 m. In contrast, Jungels & Frazier (1973) inverted the observed static surface displacement data with a FEM model by direct methods, i.e. 'trial and error'. Their model gave an average fault slip much the same as that obtained by Alewine & Jordan. Thus, with the exception of the work by Trifunac, our results for the relative displacements along the fault plane, 2.2 m on average, are in excellent agreement with those obtained by previous investigators, as is the rms error of our fit; 8.0 cm for the optimum solution.

The slip and fault dimensions can be used to compute the seismic moment

$$M_0 = \mu SA$$

where  $\mu$  is the shear modulus in the fault zone,  $S$  is the average slip or displacement across the fault, and  $A$  is the faulted area. Since our model is two-dimensional, and because both  $S$  and  $\mu$  vary along the fault, we may compute the seismic moment per kilometre of fault length

$$M = 10^5 \int_{\text{hypocentre}}^{\text{surface}} \mu(x) S(x) dx$$

where  $\mu$  is in units of dyne  $\text{cm}^{-2}$ ,  $S$  and  $x$  are in cm. From the slips given in Fig. 9 and the seismic parameters of our model (Fig. 2), we obtain  $M = 0.27 \times 10^{25}$  dyne cm per km of fault width, which is a factor of 3 less than the value obtained by Jungels & Frazier (1973) from their profile BB'. If we assume the faulted area to be 15 km wide, then the seismic moment given by our results is  $M_0 = 4.0 \times 10^{25}$  dyne cm. This value is in general agreement with the values obtained by other investigators: Wyss & Hanks (1972), Alewine (1974), and Hanks (1974), for example.

Estimates for the stress drop during the San Fernando earthquake vary. Wyss & Hanks (1972) calculated the stress drop to be 14 bar from teleseismic body-wave data. Canitez & Toksoz (1972) estimated the stress drop to be 70 bar. Jungels & Frazier (1972) estimated the stress drop to be approximately 25 bar. Alewine & Jordan (1974) did not calculate the average stress drop, but more recent work (Alewine, private communication) indicates that it is on the order of 100–200 bar. In a reinterpretation of the Pacoima Dam accelerograms, Hanks (1974) has postulated massive stress drops of 350–1400 bar localized in the hypocentral region. Our static results, computed directly from the finite element model, give an average stress drop of 290 bar with a maximum of 650 bar and support the higher values reported by Alewine & Hanks. However, in our model, the highest stress drop is not located at the initial point of rupture.

The higher stress drops are also supported by the dynamic results. Because the FEM problem is linear, an average stress drop of 30 bar, would produce, for any reasonable rupture velocity, maximum computed accelerations one tenth the value of those observed. The dynamic models predict that the major, low-frequency energy in the early part of the Pacoima Dam accelerograms is due to shear waves generated as the rupture propagates up the fault surface to points nearest the receiver at Pacoima Dam. Although the rupture radiates all along the fault surface, the peak amplitude in the accelerograms predicted by this model is due to  $S$ -wave energy propagating from the point on the fault nearest the receiver.

The predicted amplitudes are generally in agreement with those observed for the corresponding portion of the Pacoima records and the calculated vs observed arrival times indicate a rupture velocity nearer to  $2.5 \text{ km s}^{-1}$  than  $2.0 \text{ km s}^{-1}$ .

The  $t_3$  arrival hypothesis advanced by this DFEM model agrees with the results presented by Bolt (1972) who found that different frequency bands in the Pacoima Dam accelerograms contained different energy arrivals. In particular, energy originating from the rupture as it propagated up the fault predominates below 2 Hz. Thus our dynamic model, constrained to low frequencies by virtue of its limited bandwidth, corresponds to and agrees with Bolt's interpretation of the data.

The local maximum in the surface motion near Pacoima Dam shown in Fig. 11 appears in similar halfspace problems run by Geller & Frazier (1976). In our model, the effect may have been accentuated by the high impedance contrast across the nearby geologic contact between the sediments of the Modelo formation and the crystalline rocks (granite) to the north (see Fig. 2). Geller & Frazier also found the effect of crustal structure on their computed waveforms to be significant.

All these results are, of course, dependent on the FEM mesh design, its resolution, and number of degrees of freedom, as well as the assumptions implicit in the dynamics of the fault model. In the region of the fault and Pacoima Dam, the average mesh spacing was on the order of 10 nodes per wavelength of the body waves being propagated. This figure is commonly used as a criterion for accuracy in DFEM calculations (e.g. McCowan 1975; Geller & Frazier 1976). A finer mesh would immediately serve to extend the frequency content of the arrivals beyond the present 2-Hz limit.

The effects of mesh coarseness on static FEM calculations are more difficult to assess. There is much civil engineering literature and lore on the subject (e.g. Zienkiewicz 1971). As a general rule, coarser elements exhibit more stiffness in linear elastic problems. Thus the unknown force vector in equation (5) and the corresponding stresses in Fig. 10 may be artificially large in our model. How much so can be estimated by noting, as above, that our fault slip solution generally agrees in magnitude with that from other investigators. Then the average strain from 7 to 13 km down the fault is approximately  $5 \times 10^{-4}$  (see Fig. 9). Using a shear modulus for granite appropriate to our structure,  $\mu = 4 \times 10^{11} \text{ dyne cm}^{-2}$ , gives an average stress difference of 200 bar in this region of the fault. Thus to believe fault slips as we and others predict, means the stresses must be on the order of hundreds of bars. Any improvement due to mesh refinement cannot be substantial when the fault offset and stresses agree as they do.

Against this must be balanced the effects of our two-dimensional model. Since the profile shown in Fig. 1 passes through the earthquake epicentre, our computed stresses in Fig. 10 will be the maximum occurring anywhere on the fault surface. Stresses averaged over the horizontal extent of the fault must be somewhat smaller.

The results of this FEM experiment, with its small mesh and idealized fault model, demonstrate that it is feasible to predict the spatial and temporal distribution of ground motion for earthquakes in other complicated geologic settings with a reasonable computational effort. While a similar treatment of three-dimensional heterogeneous structures can be readily developed, the computational effort involved is prohibitive except on the largest, and fastest digital computers presently available.

#### Acknowledgments

It is a pleasure to acknowledge the assistance afforded us by R. W. Alewine. S. T. Harding kindly supplied us with a preliminary copy of his FEM mesh from which the mesh used in

this paper was developed. This research was supported by the National Oceanic and Atmospheric Administration under Grant N-22-125-72(G) and the US Advanced Research Projects Agency under Grant AFOSR-73-2515. One of the authors (DWM) was also supported by the Advanced Research Projects Agency of the Department of Defense.

### References

- Alewine, R. W., 1974. Application of linear inversion theory toward the estimation of seismic source parameters, *PhD thesis*, 303 pp., California Institute of Technology, Pasadena.
- Alewine, R. W. & Jordan, T. H., 1973. Generalized inversion of earthquake static displacement fields, *Geophys. J. R. astr. Soc.*, **35**, 357-361.
- Allen, C. R., Engen, G. R., Hanks, T. C., Nordquist, J. M. & Thatcher, W. R., 1971. Main shock and larger aftershocks of the San Fernando earthquake, February 9, through March 1, *US geol. Surv. Prof. Paper*, **733**, 17-20.
- Backus, G. & Gilbert, F., 1970. Uniqueness in the inversion of inaccurate gross Earth data, *Phil. Trans. R. Soc. Lond. A.*, **266**, 123-192.
- Bolt, B. A., 1972. San Fernando rupture mechanism and the Pacoima strong-motion record, *Bull. seism. Soc. Am.*, **62**, 1053-1961.
- Boore, D. M., 1973. The effect of simple topography: implications for the accelerations recorded at Pacoima Dam, San Fernando Valley, California, *Bull. seism. Soc. Am.*, **63**, 1603-1609.
- Boore, D. M. & Zoback, M. D., 1974. Two-dimensional kinematic fault modeling of the Pacoima Dam strong-motion recordings of the February 9, 1971, San Fernando earthquake, *Bull. seism. Soc. Am.*, **64**, 555-570.
- Brune, J. N., 1974. Current status of understanding quasi-permanent fields associated with earthquakes, *Trans. Am. geophys. Union*, **55**, 820-827.
- Canitez, N. & Toksoz, M. N., 1972. Static and dynamic study of earthquake source mechanism: San Fernando earthquake, *J. geophys. Res.*, **77**, 2583-2594.
- Duke, C. M., Johnson, J. A., Kharraz, Y., Campbell, K. W. & Malpiede, N. A., 1971. Subsurface site conditions and geology in the San Fernando earthquake area, *UCLA Engineering Report*, 188 pp., UCLA-ENG-7206, University of California, Los Angeles.
- Espinosa, A. F., Harding, S. T. & Lopez-Arroyo, A., 1973. Strong motion accelerations and displacements at near and intermediate distances; San Fernando earthquake, *Earthquake Notes*, **XLIV**, 49.
- Foster, M., 1961. An application of the Wiener-Kolmogorov smoothing theory to matrix inversion, *J. Soc. indust. Math.*, **9**, 387-392.
- Geller, R. J. and Frazier, G. A., 1976. Near field modelling of dislocations in a heterogeneous crust: a dynamic finite element approach, *J. geophys. Res.*, in press.
- Gilbert, F., 1970. Inverse problems for the Earth's normal modes, *The nature of the solid earth*, McGraw-Hill, New York.
- Grantz, A., 1971. The San Fernando, California, earthquake of February 9, 1971, *US geol. Surv. Prof. Paper*, **733**, 1-4.
- Hanks, T. C., 1974. The faulting mechanism of the San Fernando earthquake, *J. geophys. Res.*, **79**, 1215-1229.
- Jordan, T. H. & Franklin, J. N., 1971. Optimal solutions to a linear inverse problem in geophysics, *Proc. Nat. Acad. Sci. Am.*, **68**, 291-293.
- Jungels, P. H. & Frazier, G. A., 1973. Finite element analysis of the residual displacements for an earthquake rupture: Source parameters for the San Fernando earthquake, *J. geophys. Res.*, **78**, 5062-5083.
- McCowan, D. W., 1975. Dynamic finite element analysis with applications to seismological problems, *PhD thesis*, 188 pp., The Pennsylvania State University, University Park, Pasadena.
- Newmark, N. M., 1959. A method of computation of structural dynamics, *J. eng. mech. Div., Prov. Am. Soc. civ. eng.*, **85**, 67-94.
- Reid, H. F., 1969. *The California Earthquake of April 18, 1906*, Carnegie Institution of Washington, Washington, DC.
- Trifunac, M. D., 1974. A three-dimensional distortion model for the San Fernando, California, earthquake of February 9, 1971, *Bull. seism. Soc. Am.*, **64**, 149-172.
- Wesson, R. L., Lee, W. H. K. & Gibbs, J. F., 1971. Aftershocks of the earthquake, *US geol. Surv. Prof. Paper*, **733**, 24-29.

- Whitcomb, J. H., Allen, C. R., Garmany, J. D. & Hileman, J. A., 1973. The 1971 San Fernando earthquake series: focal mechanisms and tectonics, *Rev. Geophys. space Phys.*, 11, 693–730.
- Wong, H. L. & Jennings, P. C., 1975. Effects of canyon topography on strong ground motion, *Bull. seism. Soc. Am.*, 65, 1239–1257.
- Wyss, M. and Hanks, T. C., 1972. The source parameters of the San Fernando earthquake inferred from teleseismic body waves, *Bull. seism. Soc. Am.*, 62, 591–602.
- Zienkiewicz, O. C., 1971. *The finite element method in engineering science*. McGraw-Hill, London.

## Appendix

### Least-squares method with tradeoff correction

The usual least-squares procedure for estimating the solution of the  $M$  by  $N$  ( $M > N$ ) system of linear equations

$$Bf = x + \epsilon \quad (\text{A1})$$

where  $B$  is the  $M$  by  $N$  coefficient matrix,  $f$  is the vector of estimates,  $x$  is the vector of observations, and  $\epsilon$  is a vector of errors in each observation, consists of minimizing the mean squared error in the system

$$\frac{1}{M} (\epsilon^T \epsilon) = \frac{1}{M} (x^T - f^T B^T) (Bf - x). \quad (\text{A2})$$

The minimization leads to the familiar equation for the estimate of  $f$

$$f = (B^T B)^{-1} B^T x \quad (\text{A3})$$

provided that  $B^T B$  is non-singular.

A simple modification of this procedure consists of weighting the contribution of each equation to the mean squared error by its own error of observation. Thus, if

$$E = \langle \epsilon \epsilon^T \rangle \quad (\text{A4})$$

is the variance-covariance matrix, the mean squared error becomes

$$\frac{1}{M} (x^T - f^T B^T) E^{-1} (Bf - x). \quad (\text{A5})$$

The stochastic inverse of the matrix  $B$  defined by Foster (1961) can be thought of as that due to adding a 'tradeoff' term ( $\alpha$ ) into equation (A5) as follows

$$\frac{1}{M} (x^T - f^T B^T) E^{-1} (Bf - x) + \frac{1}{M} \alpha f^T f. \quad (\text{A6})$$

Thus  $\alpha$  controls how much of the additional term the mean squared error 'sees'. Minimization of this expression gives

$$f = (B^T E^{-1} B + \alpha I)^{-1} B^T E^{-1} x. \quad (\text{A7})$$

If the errors in the observations are uncorrelated, then the matrix  $E$  is diagonal and the non-zero elements are simply the weights in the estimate.

APPENDIX G

## A FAST, ACCURATE METHOD FOR COMPUTING GROUP-VELOCITY PARTIAL DERIVATIVES FOR RAYLEIGH AND LOVE MODES

BY W. L. RODI, P. GLOVER, T. M. C. LI, AND S. S. ALEXANDER

### ABSTRACT

A method for quickly and accurately calculating Rayleigh- and Love-mode group-velocity partial derivatives with respect to model parameters ( $m$ ) is developed. The method requires computer codes that calculate  $C$ ,  $U$ , and  $\left. \frac{\partial C}{\partial m} \right|_{\omega}$  and employs numerical differentiation of  $\left. \frac{\partial C}{\partial m} \right|_{\omega}$  to yield  $\left. \frac{\partial U}{\partial m} \right|_{\omega}$ . The method is fast because  $\left. \frac{\partial C}{\partial m} \right|_{\omega}$  and  $\left. \frac{\partial U}{\partial m} \right|_{\omega}$  for all the model parameters can be obtained at a given frequency from only two solutions of the period equation. The accuracy of the method is established with two examples. For Love waves, the group-velocity partials computed by this method agree exactly with those obtained analytically by Novotny (1970). For Rayleigh waves, comparison with a "brute force" calculation of group-velocity partials showed agreement to the order of 0.0002. Systematic inversion of group-velocity data separately or in combination with phase-velocity data is computationally feasible using this method.

### INTRODUCTION

The development of linear inverse theory (for example, Foster, 1961; Franklin, 1970; Backus and Gilbert, 1970; Wiggins, 1972; Jordan, 1973) has made it possible to deduce earth structures from a variety of seismological data. The successful application of this theory requires a computationally efficient method for repeatedly generating partial derivatives of the data predicted by an earth model with respect to the parameters of that model. This paper offers an efficient method for computing partial derivatives of Rayleigh- and Love-wave group velocity for a horizontally stratified earth model. The method is accurate and readily implemented using any existing computer program that calculates phase velocity, group velocity, and phase-velocity partials with respect to model parameters.

Compared to phase-velocity partials, group-velocity partials have proved cumbersome and time-consuming to compute. Also, the most efficient of the presently available techniques to compute group-velocity partials applies to Love waves but not Rayleigh waves. This has prevented the calculation of Rayleigh-wave group-velocity partials on a routine basis. A brief review of the available methods, presented below in order of increasing efficiency, will point out these difficulties.

First, the "brute force" approximation to group-velocity partial derivatives can be obtained by calculating the changes in group velocity at each frequency caused by the separate perturbation of each model parameter. This method can be used for both Love and Rayleigh modes but is very time-consuming.

Second, Novotny (1970) derived exact expressions for Love-wave group-velocity partials for a horizontally layered earth model. His expressions involve first and second derivatives of the root equation with respect to phase velocity, frequency, and the model

parameters. Novotny evaluates these derivatives in terms of first and second derivatives of the Thomson-Haskell layer matrices (Haskell, 1953). The computer time required to generate all the necessary layer matrix derivatives and to perform the many matrix multiplications needed is considerable.

Third, Harkrider (1968) and Anderson and Harkrider (1968) derived exact expressions for Love-wave group-velocity partials in a different way. By using the variational principle, they were able to express the partials in terms of first derivatives of energy integrals. Because only first derivatives of the layer matrices are required, their method requires fewer calculations than Novotny's. This, to our knowledge, has not been applied to Rayleigh waves.

Finally, a method due to Kosloff (1975) for approximating Love-wave group-velocity partials reduces the number of calculations even further. Using second-order perturbation, Kosloff (1975) expresses the partials in terms of a sum of energy integrals for all of the modes at a given wave number or frequency. He employs a scheme to eliminate leaky modes and force the sum to converge in five or fewer terms; thus the method requires approximately four or five root calculations per frequency (Kosloff, 1975).

The method for obtaining group-velocity partials described in this paper works for any Rayleigh- or Love-wave mode. It requires only the calculation of a double set of roots and phase-velocity partials to obtain group-velocity partials for all model parameters at a given frequency. The basis for the method is the theoretical relationship between group- and phase-velocity partial derivatives which is derived in the next section.

#### THEORY

Define  $U$  to be the group velocity and  $C$  to be the phase velocity at a frequency  $\omega$ .

Let  $\left. \frac{\partial U}{\partial m} \right|_{\omega}$  and  $\left. \frac{\partial C}{\partial m} \right|_{\omega}$ , respectively, be the derivatives with respect to a model parameter  $m$ , holding  $\omega$  fixed, of group and phase velocity.

By ignoring all the model parameters of a layered half-space except  $m$ ,  $C$  can be written as a function of  $\omega$  and  $m$

$$C = f(\omega, m) \quad (1)$$

where  $C$  is a root of the period equation

$$F(C, \omega, m) = 0. \quad (2)$$

If the function  $f_2$  is defined to be the partial derivative of  $f$  with respect to its second argument, then

$$\left. \frac{\partial C}{\partial m} \right|_{\omega} = f_2(\omega, m). \quad (3)$$

Similarly, the derivative of phase velocity with respect to  $\omega$  is given by

$$\left. \frac{\partial C}{\partial \omega} \right|_m = f_1(\omega, m). \quad (4)$$

Now let  $U$  and  $\left. \frac{\partial U}{\partial m} \right|_{\omega}$  be values of the functions  $g$  and  $g_2$

$$U = g(\omega, m) \quad (5)$$

$$\left. \frac{\partial U}{\partial m} \right|_{\omega} = g_2(\omega, m). \quad (6)$$

The relationship between  $\left. \frac{\partial U}{\partial m} \right|_{\omega}$  and  $\left. \frac{\partial C}{\partial m} \right|_{\omega}$  is derived from the relationship between  $U$  and  $C$  which is

$$U = \frac{C}{\omega \left. \frac{\partial C}{\partial \omega} \right|_m} \equiv \phi(C, \left. \frac{\partial C}{\partial \omega} \right|_m, \omega). \quad (7)$$

From (7),  $g(\omega, m)$  is recognized to be

$$g(\omega, m) = \phi(f(\omega, m), f_1(\omega, m), \omega). \quad (8)$$

Application of the chain rule results in

$$g_2 = \phi_1 f_2 + \phi_2 f_{12} \quad (9)$$

where the function  $f_{12}$  is the derivative of  $f_1$  with respect to its second argument. Since  $f_1$  and  $f_2$  are differentiable,

$$\left. \frac{\partial}{\partial m} \left( \left. \frac{\partial C}{\partial \omega} \right|_m \right) \right|_{\omega} \equiv f_{12}(\omega, m) = f_{21}(\omega, m) \equiv \left. \frac{\partial}{\partial \omega} \left( \left. \frac{\partial C}{\partial m} \right|_{\omega} \right) \right|_m. \quad (10)$$

Explicit differentiation of  $\phi$  yields

$$\phi_1 = \frac{U}{C} \left( 2 - \frac{U}{C} \right) \quad (11)$$

$$\phi_2 = \frac{U^2}{C^2} \omega. \quad (12)$$

Therefore, using (10), (11), and (12), equation (9) can be rewritten as

$$\left. \frac{\partial U}{\partial m} \right|_{\omega} = \frac{U}{C} \left( 2 - \frac{U}{C} \right) \left. \frac{\partial C}{\partial m} \right|_{\omega} + \omega \frac{U^2}{C^2} \left. \frac{\partial}{\partial \omega} \left( \left. \frac{\partial C}{\partial m} \right|_{\omega} \right) \right|_m. \quad (13)$$

The expression

$$\frac{m}{U} \left. \frac{\partial U}{\partial m} \right|_{\omega} = \frac{m}{C} \left. \frac{\partial C}{\partial m} \right|_{\omega} + \frac{U}{C} \omega \left. \frac{\partial}{\partial \omega} \left( \left. \frac{\partial C}{\partial m} \right|_{\omega} \right) \right|_m \quad (14)$$

relating logarithmic partial derivatives can be derived in a similar way.

Novotny (1970) derived an expression equivalent to (13). He evaluated  $f_{12}$  analytically in terms of derivatives of  $F$  in (2), but for Love waves only.

The next section describes a technique for accurately approximating (13).

#### NUMERICAL APPROXIMATIONS

This section describes an algorithm which, for a given frequency, requires the solution for only two roots of equation (2) to get the group-velocity partials with respect to all of the model parameters. The method described is to approximate  $\left. \frac{\partial}{\partial \omega} \left( \left. \frac{\partial C}{\partial m} \right|_{\omega} \right) \right|_m$  by numerically differentiating  $\left. \frac{\partial C}{\partial m} \right|_{\omega}$ . Standard Thomson-Haskell matrix calculations are used to get  $C$ ,  $U$ , and  $\left. \frac{\partial C}{\partial m} \right|_{\omega}$ . Since equations (13) and (14) depend only on the relationship between  $U$  and  $C$  in (7), clearly this method can be applied to any Rayleigh- or Love-wave mode.

Suppose the quantities  $C$ ,  $U$ ,  $\left.\frac{\partial C}{\partial m}\right|_{\omega}$ , and  $\left.\frac{\partial U}{\partial m}\right|_{\omega}$  are desired at the frequency  $\omega_0$ . Define  $\omega_{+1} = \omega_0 e^{\delta}$  and  $\omega_{-1} = \omega_0 e^{-\delta}$ . If the quantities  $C_1$ ,  $U_1$ , and  $\left.\frac{\partial C_1}{\partial m}\right|_{\omega}$  for each model parameter are computed at  $\omega_1$ , and if  $C_{-1}$ ,  $U_{-1}$ , and  $\left.\frac{\partial C_{-1}}{\partial m}\right|_{\omega}$  are computed at  $\omega_{-1}$ , then the following approximations can be assigned to the central frequency  $\omega_0$

$$C_0 = 1/2(C_1 + C_{-1}) \quad (15a)$$

$$U_0 = 1/2(U_1 + U_{-1}) \quad (15b)$$

$$\left.\frac{\partial C_0}{\partial m}\right|_{\omega} = 1/2\left(\left.\frac{\partial C_1}{\partial m}\right|_{\omega} + \left.\frac{\partial C_{-1}}{\partial m}\right|_{\omega}\right) \quad (15c)$$

$$\left.\frac{\partial U_0}{\partial m}\right|_{\omega} = \frac{U_0}{C_0} \left(2 - \frac{U_0}{C_0}\right) \left.\frac{\partial C_0}{\partial m}\right|_{\omega} + \frac{U_0^2}{C_0^2} \left(\left.\frac{\partial C_1}{\partial m}\right|_{\omega} - \frac{\left.\partial C_{-1}}{\partial m}\right|_{\omega}\right) \quad (15d)$$

A central difference is used in (15d) because this is the most accurate two-point approximation to  $\omega \left.\frac{\partial}{\partial \omega} \left(\left.\frac{\partial C}{\partial m}\right|_{\omega}\right)\right|_m$ . Using the averages (15a) to (15c) avoids the calculation of a root at  $\omega_0$ . Also, the first of the two roots calculated provides an excellent initial guess for the second root, which speeds up the calculation; given  $C_{-1}$  and  $U_{-1}$ , a very accurate guess to  $C_1$  is  $C_{-1}[1 + 2\delta(1 - (C_{-1}/U_{-1}))]$ .

The counterparts to equations (15c) and (15d) for the logarithmic partials in (14) are

$$\frac{m}{C_0} \left.\frac{\partial C_0}{\partial m}\right|_{\omega} = 1/2\left(\frac{m}{C_1} \left.\frac{\partial C_1}{\partial m}\right|_{\omega} + \frac{m}{C_{-1}} \left.\frac{\partial C_{-1}}{\partial m}\right|_{\omega}\right) \quad (16a)$$

$$\frac{m}{U_0} \left.\frac{\partial U_0}{\partial m}\right|_{\omega} = \frac{m}{C_0} \left.\frac{\partial C_0}{\partial m}\right|_{\omega} + \frac{U_0}{C_0} \left(\frac{m}{C_1} \left.\frac{\partial C_1}{\partial m}\right|_{\omega} - \frac{m}{C_{-1}} \left.\frac{\partial C_{-1}}{\partial m}\right|_{\omega}\right) \quad (16b)$$

*Choosing  $\delta$ .* The error in the approximation (15d) can be decomposed into two parts:  $e = e_1 + e_2$ .  $e_1$  arises from the nonlinearity of  $C$ ,  $U$ , and  $\left.\frac{\partial C}{\partial m}\right|_{\omega}$  as a function of  $\log \omega$  and can be shown to be on the order of  $\delta^2$ ;  $e_2$  is the result of round-off errors in  $C_1$ ,  $U_1$ ,  $\left.\frac{\partial C_1}{\partial m}\right|_{\omega}$ ,  $C_{-1}$ ,  $U_{-1}$  and  $\left.\frac{\partial C_{-1}}{\partial m}\right|_{\omega}$  and behaves as  $\delta^{-1}$ . If the errors in  $\left.\frac{\partial C_1}{\partial m}\right|_{\omega}$  and  $\left.\frac{\partial C_{-1}}{\partial m}\right|_{\omega}$  are  $\varepsilon_1$  and  $\varepsilon_{-1}$ , respectively, then for small  $\delta$

$$e_2 \sim \frac{U_0^2}{C_0^2} \left(\frac{\varepsilon_1 - \varepsilon_{-1}}{2\delta}\right). \quad (17)$$

A knowledge of  $\varepsilon_1$  and  $\varepsilon_{-1}$  enables a lower limit on  $\delta$  to be established to ensure that  $e_2$  be within a specified tolerance. If an upper limit on  $|\varepsilon_1|$  and  $|\varepsilon_{-1}|$ , say  $\varepsilon_{\max}$ , can be determined based on the precision of the phase-velocity partial calculations performed, then an upper limit on  $|e_2|$  is

$$e_2 \max = \frac{U_0^2 \varepsilon_{\max}}{C_0^2 \delta}. \quad (18)$$

Taking  $e_2 \max$  to be the largest tolerable  $|e_2|$ , a criterion for choosing  $\delta$  is

$$\delta > \frac{\epsilon_{\max}}{e_2 \max} \quad (19)$$

since  $U_0 \approx C_0$ . For example, if  $\left. \frac{\partial C_1}{\partial m} \right|_{\omega}$  and  $\left. \frac{\partial C_{-1}}{\partial m} \right|_{\omega}$  are accurate to  $N$  decimal figures, and if  $M$  decimal figures are desired for  $\left. \frac{\partial U_0}{\partial m} \right|_{\omega}$ , then  $\epsilon_{\max} = 1/2 \cdot 10^{-N}$ ,  $e_2 \max = 1/2 \cdot 10^{-M}$ , and (19) becomes

$$\delta > 10^{M-N}. \quad (20)$$

If  $M$  is sufficiently less than  $N$ , then  $\delta$  will be small enough to guarantee both a small  $e_1$  and a small  $e_2$ . The criterion in (20) can be applied to all modes since  $\delta$  is a perturbation of  $\log \omega$ .

TABLE 1  
CANSD CANADIAN SHIELD MODEL

$i$	$h_i$ (km)	$d_i$ (km)	$\beta_i$ (km/sec)	$\rho_i$ (gm/cm <sup>3</sup> )
1	6.0	3.0	3.47	2.70
2	10.5	11.25	3.64	2.80
3	18.7	25.85	3.85	2.85
4	80.0	75.2	4.72	3.30
5	100.0	165.2	4.54	3.44
6	100.0	265.2	4.51	3.53
7	80.0	355.2	4.76	3.60
8	$\infty$	—	5.12	3.76

\*  $h_i$  is layer thickness.

†  $d_i$  is depth to center of  $i$ th layer.

#### EXAMPLES

The algorithm in (15), hereafter referred to as the  $\Delta P$  (delta partial) method, was tested for fundamental-mode Love waves on a continental shield model and for fundamental-mode Rayleigh waves on an ocean model. In both cases  $U$ ,  $C$ , and  $\left. \frac{\partial C}{\partial m} \right|_{\omega}$  at the perturbed frequencies ( $\omega_1$  and  $\omega_{-1}$ ) were calculated with computer programs written by D. Harkrider for implementing methods described in Anderson (1964), Takeuchi *et al.* (1962), and Takeuchi *et al.* (1964).

*Example 1: Love waves.* Using the  $\Delta P$  method with  $\delta = 0.001$ , Love-wave group-velocity partial derivatives with respect to shear velocity ( $\beta$ ) and density ( $\rho$ ) were computed at periods of 20 and 40 sec for a version of the CANSD Canadian shield model (Brune and Dorman, 1963), shown in Table 1. The same derivatives were computed analytically by Novotny (1970). The  $\Delta P$  results are tabulated in Table 2 and agree in each case with the five decimal figures given by Novotny.

*Example 2: Rayleigh waves.* Again using equations (15) with  $\delta = 0.001$ , Rayleigh-wave group-velocity partials for a version of the Anderson ocean model (Harkrider, 1970), given in Table 3, were computed for seven periods. (For the purposes of this example, the model was taken as a flat, rather than spherical, earth.) The group-velocity and phase-velocity partial derivatives with respect to  $\beta$  for each layer at 66, 100, and 200 sec are shown in Figure 1.

TABLE 2  
PHASE- AND GROUP-VELOCITY PARTIAL DERIVATIVES FOR CANSO MODEL

$i$	$\frac{\partial C}{\partial \beta_i}$	$\frac{\partial C}{\partial \rho_i}$	$\frac{\partial U}{\partial \beta_i}$	$\frac{\partial U}{\partial \rho_i}$
<i>Period = 20 sec; C = 4.00710 km/sec; U = 3.52732 km/sec</i>				
1	0.25048	-0.05192	0.39610	-0.03708
2	0.40458	-0.03721	0.56217	0.01013
3	0.40666	0.03642	0.29970	0.06946
4	0.13636	0.04255	-0.17980	-0.03776
5	0.00022	0.00005	-0.00205	-0.00046
6	0.0	0.0	0.0	0.0
7	0.0	0.0	0.0	0.0
<i>Period = 40 sec; C = 4.40209 km/sec; U = 4.01515 km/sec</i>				
1	0.09234	-0.03562	0.26627	-0.08695
2	0.16802	-0.04359	0.47105	-0.09121
3	0.26171	-0.02070	0.64765	0.01359
4	0.48998	0.07374	0.37427	0.14947
5	0.10746	0.00813	-0.28059	-0.00354
6	0.01742	0.00136	-0.10107	-0.00573
7	0.00147	0.00027	-0.01280	-0.00223

TABLE 3  
ANDERSON OCEAN MODEL

$i$	$h_i$	$d_i$	$a_i$	$\beta_i$	$\rho_i$
0	5.0000	2.50	1.5200	0.0	1.0300
1	1.0000	5.50	2.1000	1.0000	2.1000
2	5.0000	8.50	6.4100	3.7000	3.0660
3	9.0000	15.50	8.1100	4.6060	3.4000
4	5.0000	22.50	8.1200	4.6110	3.4000
5	15.0000	32.50	8.1200	4.6100	3.4000
6	10.0000	45.00	8.0100	4.5600	3.3700
7	10.0000	55.00	8.0100	4.5600	3.3700
8	10.0000	65.00	7.9500	4.5600	3.3700
9	10.0000	75.00	7.9500	4.5600	3.3700
10	10.0000	85.00	7.7100	4.4000	3.3700
11	10.0000	95.00	7.7100	4.4000	3.3700
12	10.0000	105.00	7.6800	4.3400	3.3300
13	10.0000	115.00	7.6800	4.3400	3.3300
14	10.0000	125.00	7.7770	4.3400	3.3300
15	10.0000	135.00	7.7770	4.3400	3.3300
16	10.0000	145.00	7.8500	4.3400	3.3300
17	10.0000	155.00	7.8500	4.3400	3.3300
18	10.0000	165.00	8.1000	4.4500	3.3300
19	10.0000	175.00	8.1000	4.4500	3.3300
20	10.0000	185.00	8.1200	4.4500	3.3300
21	10.0000	195.00	8.1200	4.4500	3.3300
22	10.0000	205.00	8.1200	4.4500	3.3300
23	10.0000	215.00	8.1200	4.4500	3.3300
24	10.0000	225.00	8.1200	4.4500	3.3300
25	10.0000	235.00	8.1200	4.4500	3.3300
26	10.0000	245.00	8.1200	4.4500	3.3300
27	10.0000	255.00	8.1200	4.4500	3.3300

*Continued.*

TABLE 3—Continued

<i>i</i>	<i>h<sub>i</sub></i>	<i>d<sub>i</sub></i>	<i>z<sub>i</sub></i>	<i>β<sub>i</sub></i>	<i>ρ<sub>i</sub></i>
28	10.0000	265.00	8.1200	4.4500	3.3500
29	10.0000	275.00	8.1200	4.4500	3.3500
30	10.0000	285.00	8.1200	4.4500	3.3600
31	10.0000	295.00	8.1200	4.4500	3.3600
32	10.0000	305.00	8.1200	4.4500	3.3700
33	10.0000	315.00	8.1200	4.4500	3.3700
34	10.0000	325.00	8.1200	4.4500	3.3800
35	10.0000	335.00	8.1200	4.4500	3.3800
36	10.0000	345.00	8.2400	4.5000	3.3900
37	10.0000	355.00	8.2400	4.5000	3.3900
38	10.0000	365.00	8.3000	4.5300	3.4400
39	10.0000	375.00	8.3600	4.5600	3.5000
40	10.0000	385.00	8.3600	4.5600	3.5000
41	10.0000	395.00	8.7500	4.7950	3.6840
42	15.0000	407.50	8.7500	4.7950	3.6840
43	20.0000	425.00	9.1500	5.0400	3.8800
44	10.0000	440.00	9.4300	5.2170	3.9000
45	20.0000	455.00	9.7600	5.4000	3.9200
46	25.0000	477.50	9.7650	5.4000	3.9330
47	25.0000	502.50	9.7750	5.4000	3.9480
48	25.0000	527.50	9.7800	5.4000	3.9600
49	25.0000	552.50	9.7840	5.4000	3.9880
50	25.0000	577.50	9.7880	5.4000	4.0220
51	25.0000	602.50	9.7920	5.4000	4.0560
52	25.0000	627.50	9.7960	5.4000	4.0900
53	25.0000	652.50	9.8000	5.4000	4.1200
54	25.0000	677.50	10.1630	5.6000	4.1650
55	25.0000	702.50	10.4880	5.8000	4.2120
56	25.0000	727.50	10.8180	6.1000	4.2570
57	25.0000	752.50	11.1200	6.2000	4.3000
58	25.0000	777.50	11.1350	6.2050	4.4750
59	25.0000	802.50	11.1500	6.2100	4.6330
60	25.0000	827.50	11.1650	6.2180	4.7970
61	25.0000	852.50	11.1800	6.2300	4.9400
62	25.0000	877.50	11.2240	6.2500	4.9425
63	25.0000	902.50	11.2670	6.2750	4.9450
64	25.0000	927.50	11.3100	6.2970	4.9475
65	25.0000	952.50	11.3500	6.3220	4.9500
66	25.0000	977.50	11.3920	6.3400	4.9517
67	25.0000	1002.50	11.4340	6.3600	4.9534
68	25.0000	1027.50	11.4760	6.3750	4.9550
69	25.0000	1052.50	11.5180	6.3900	4.9567
70	25.0000	1077.50	11.5600	6.4050	4.9584
71	∞	—	11.6000	6.4210	4.9600

The partials with respect to  $\beta$  in six of the model's layers were also computed by the "brute force" approximation for five periods. A central difference scheme

$$\left. \frac{\partial U}{\partial \beta} \right|_{\omega} \approx \frac{\Delta U}{2\Delta\beta} \quad (21)$$

was used, where  $\Delta U$  is the difference between the group velocities for models with  $\beta$  perturbed by  $+\Delta\beta$  and  $-\Delta\beta$  in a given layer. A  $\Delta\beta$  of 0.1 was used for each of the 6

layers. The accuracy of the  $U$  partials computed this way is difficult to judge, but repeating the layer 6 calculation with  $\Delta\beta = 0.05$  revealed that the errors were on the order of 0.00002.

It can be seen from Table 4 that the agreement between the brute force and  $\Delta P$  group-velocity partials is very close. For layer 6 the agreement is closer when  $\Delta\beta = 0.05$  than when  $\Delta\beta = 0.1$ . Therefore, we infer errors of 0.00002 or less in the  $\Delta P$  answers.

#### DISCUSSION

The  $\Delta P$  method is an efficient way to compute group-velocity partial derivatives with an accuracy sufficient for use in inversion calculations. This capability increases the feasibility of using available group-velocity data, either separately or jointly with phase-velocity data, in the determination of earth structure by linear inverse methods.

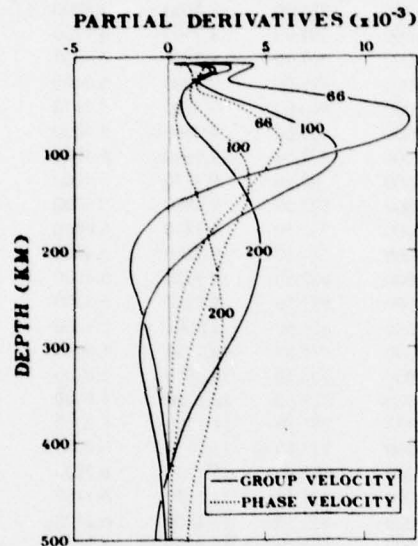


FIG. 1. Phase- and group-velocity partial derivatives with respect to  $\beta$  at periods of 66, 100, and 200 sec for Anderson ocean model. Partial derivatives are normalized by layer thickness; i.e.,  $(1/h_i)(\partial C/\partial\beta_i)$  and  $(1/h_i)(\partial U/\partial\beta_i)$ .

It is very desirable to be able to invert group-velocity data because of the extensive areal coverage of existing group-velocity observations as compared to phase-velocity observations, particularly at periods which sample the lithosphere. Also, a very large percentage of available higher-mode dispersion data consists of group-velocity measurements. Moreover, group-velocity determinations commonly can be more accurate than phase-velocity determinations. This is particularly true if a single source-station pair is used or if Fourier spectral methods involving long time windows are required for phase-velocity estimates while narrow-band filters suffice for group velocity.

In addition to their use in finding models consistent with group-velocity observations, partial derivatives can be used to generate averaging kernels. With averaging kernels, experiments can be designed to determine the most favorable frequencies to observe and the accuracy of group-velocity data needed to resolve radial or lateral variations in earth structure.

TABLE 4  
 COMPARISON OF  $\Delta P$  AND BRUTE FORCE (B.F.) RAYLEIGH-  
 WAVE GROUP-VELOCITY PARTIALS WITH RESPECT TO  $\beta$   
 $[(\partial U/\partial \beta)_w]$  IN SIX LAYERS OF ANDERSON OCEAN MODEL\*

<i>i</i>	B.F.	$\Delta P$
<i>Period = 140 sec; C = 4.1782 km/sec;</i>		
<i>U = 3.7468 km/sec</i>		
6	0.01378 ( $\Delta\beta = 0.05$ )	
6	0.01379	0.01378
11	0.05285	0.05281
16	0.06066	0.06063
21	0.04024	0.04023
31	-0.00058	-0.00058
41	-0.01140	-0.01139
<i>Period = 100 sec; C = 4.0751 km/sec;</i>		
<i>U = 3.9087 km/sec</i>		
6	0.03559 ( $\Delta\beta = 0.05$ )	
6	0.03560	0.03557
11	0.08448	0.08444
16	0.05468	0.05466
21	0.01386	0.01387
31	-0.01480	-0.01480
41	-0.00770	-0.00769
<i>Period = 70 sec; C = 4.0406 km/sec;</i>		
<i>U = 4.0003 km/sec</i>		
6	0.08617 ( $\Delta\beta = 0.05$ )	
6	0.08622	0.08615
11	0.09409	0.09407
16	0.01697	0.01698
21	-0.01484	-0.01483
31	-0.01113	-0.01113
41	-0.00207	-0.00207
<i>Period = 33 sec; C = 4.0350 km/sec;</i>		
<i>U = 4.0051 km/sec</i>		
6	0.23231 ( $\Delta\beta = 0.05$ )	
6	0.23234	0.23231
11	-0.02903	-0.02903
16	-0.02447	-0.02446
21	-0.00642	-0.00642
31	-0.00023	-0.00023
41	-0.00000	-0.00000
<i>Period = 16.5 sec; C = 3.8375 km/sec;</i>		
<i>U = 2.9741 km/sec</i>		
6	-0.10876 ( $\Delta\beta = 0.05$ )	
6	-0.10877	-0.10876
11	-0.00783	-0.00782
16	-0.00013	-0.00013
21	0.00000	0.00000
31	0.00000	0.00000
41	0.00000	0.00000

\* The brute force results were computed with  $\Delta\beta = 0.1$  except where 0.05 is indicated.

An inversion program is currently being developed that incorporates the  $\Delta P$  method of computing partial derivatives and allows inversion of group and phase velocity separately or in combination for both Rayleigh and Love modes.

#### ACKNOWLEDGMENTS

This research was supported by the Advanced Research Projects Agency of the Department of Defense and was monitored by the Air Force Office of Scientific Research under Contract AFSOR-73-2515.

#### REFERENCES

- Anderson, D. L. (1964). Universal dispersion tables I. Love waves across oceans and continents on a spherical earth, *Bull. Seism. Soc. Am.* **54**, 681-726.
- Anderson, D. L. and D. G. Harkrider (1968). Universal dispersion tables II. Variational parameters for amplitudes, phase velocity and group velocity for first four Love modes for an oceanic and a continental earth model, *Bull. Seism. Soc. Am.* **58**, 1407-1499.
- Backus, G. and F. Gilbert (1970). Uniqueness in the inversion of inaccurate gross earth data, *Phil. Trans. Roy. Soc. London, Ser. A* **266**, 123-192.
- Brune, J. and J. Dorman (1963). Seismic waves and earth structure in the Canadian shield, *Bull. Seism. Soc. Am.* **53**, 167-209.
- Foster, M. (1961). An application of the Wiener-Kolmogorov smoothing theory to matrix inversion, *J. Soc. Indust. Math.* **9**, 387-392.
- Franklin, J. N. (1970). Well-posed stochastic extensions of ill-posed linear problems, *J. Math. Anal. Appl.* **31**, 682-716.
- Harkrider, D. G. (1968). The perturbation of Love wave spectra, *Bull. Seism. Soc. Am.* **58**, 861-880.
- Harkrider, D. G. (1970). Surface waves in multilayered elastic media. Part II. Higher mode spectra and spectral ratios from point sources in plane layered earth models, *Bull. Seism. Soc. Am.* **60**, 1937-1987.
- Haskell, N. A. (1953). The dispersion of surface waves on multilayered media, *Bull. Seism. Soc. Am.* **43**, 17-34.
- Jordan, T. H. (1973). Estimation of the radial variation of seismic velocities and density in the earth, *Ph.D. Thesis*, Calif. Inst. Tech., Pasadena, California.
- Kosloff, D. (1975). A perturbation scheme for obtaining partial derivatives of Love wave group velocity dispersion, preprint.
- Novotny, O. (1970). Partial derivatives of dispersion curves of Love waves in a layered medium, *Studia Geophys. Geodaet., Ceskoslov. Akad. Ved.* **14**, 36-50.
- Takeuchi, H., M. Saito, and N. Kobayashi (1962). Study of shear velocity distribution in the upper mantle by mantle Rayleigh and Love waves, *J. Geophys. Res.* **67**, 2831-2839.
- Takeuchi, H., J. Dorman, and M. Saito (1964). Partial derivatives of surface wave phase velocity with respect to physical parameter changes within the earth, *J. Geophys. Res.* **69**, 3429-3441.
- Wiggins, R. A. (1972). The general linear inverse problem: implication of surface waves and free oscillations for earth structure, *Rev. Geophys.* **10**, 251-285.

GEOPHYSICS PROGRAM  
DEPARTMENT OF GEOSCIENCES  
THE PENNSYLVANIA STATE UNIVERSITY  
204 MINERAL SCIENCES BUILDING  
UNIVERSITY PARK, PENNSYLVANIA 16802

Manuscript received March 31, 1975

REPORT DOCUMENTATION PAGE		READ INSTRUCTIONS BEFORE COMPLETING FORM
1. REPORT NUMBER AFOSR-TR- 78 - 1260	2. GOVT ACCESSION NO.	3. RECIPIENT'S CATALOG NUMBER
4. TITLE (and Subtitle) RELATIONSHIP BETWEEN NEAR-FIELD AND TELESEISMIC OBSERVATIONS OF SEISMIC SOURCE PARAMETERS	5. TYPE OF REPORT & PERIOD COVERED Final 01 Apr 73 - 30 Sep 77	
	6. PERFORMING ORG. REPORT NUMBER	
7. AUTHOR(s) S. A. Alexander	8. CONTRACT OR GRANT NUMBER(s) AFOSR 73-2515	
9. PERFORMING ORGANIZATION NAME AND ADDRESS Department of Geosciences Pennsylvania State University University Park, PA 16802	10. PROGRAM ELEMENT, PROJECT, TASK AREA & WORK UNIT NUMBERS A.O.1827 62701E 4F10	
11. CONTROLLING OFFICE NAME AND ADDRESS ARPA/NMR 1400 Wilson Blvd. Arlington, VA 22209	12. REPORT DATE July 1978	
	13. NUMBER OF PAGES 187	
14. MONITORING AGENCY NAME & ADDRESS (if different from Controlling Office) AFOSR/NP Bolling AFB, Bldg.#410 Wash DC 20332	15. SECURITY CLASS. (of this report) Unclassified	
	15a. DECLASSIFICATION/DOWNGRADING SCHEDULE	
16. DISTRIBUTION STATEMENT (of this Report)  Approved for public release; distribution unlimited.		
17. DISTRIBUTION STATEMENT (of the abstract entered in Block 20, if different from Report)		
18. SUPPLEMENTARY NOTES		
19. KEY WORDS (Continue on reverse side if necessary and identify by block number)		
20. ABSTRACT (Continue on reverse side if necessary and identify by block number) The following summary outlines the accomplishments under this grant. It was determined: 1. There are significant variations in body-wave and surface wave excitation for explosions of comparable magnitude detonated in similar source media and located only a few kilometers apart at NTS (Yucca Flats and Pahute Mesa). These observed differences in excitation and energy partitioning imply either a rapidly varying tectonic stress field in the source region and/or strongly varying patterns of near-source fracturing. Source-generated P-wave code of two minutes duration or more are observed at NORSAR to vary significantly in		

strength and character among nearby Yucca and Pahute events, possibly due to short-period surface wave to P-wave scattering; 2. that relatively few SRO-type stations can be used to compare source mechanisms for suites of events of varying size in a given source region. For example, foreshocks and aftershocks of the Utah-Idaho border and Oroville, California sequences of 1975, as recorded at the Albuquerque SRO station, have been analyzed and compared; in both cases the principal foreshock exhibited the same mechanisms as the main shock, while the aftershocks are more varied in mechanism. For both sequences we were able to match the observed Love and Rayleigh waveforms and spectra as the mechanisms changed. Average path dispersion (hence structure) is a useful by-product of the analysis.



UNCLASSIFIED

UNCLASSIFIED

SECURITY CLASSIFICATION OF THIS PAGE (When Data Entered)